UC Berkeley
UC Berkeley Electronic Theses and Dissertations

Title
Electrostatic control of electronic and structural orderings in two-dimensional materials

Permalink
https://escholarship.org/uc/item/29k118mq

Author
Wang, Ying

Publication Date
2018

Peer reviewed|Thesis/dissertation

eScholarship.org Powered by the California Digital Library
University of California

Electrostatic control of electronic and structural orderings in two-dimensional materials

By

Ying Wang

A dissertation submitted in partial satisfaction of the

requirements for the degree of

Doctor of Philosophy

in

Applied Science & Technology
and the Designated Emphasis
in
Nanoscale Science & Engineering

in the

Graduate Division

of the

University of California, Berkeley

Committee in charge:

Professor Xiang Zhang, Chair
Professor Michael F. Crommie
Assistant Professor Jie Yao

Spring 2018

Electrostatic control of electronic and structural orderings in two-dimensional materials

© Copyright 2018
Ying Wang
All rights reserved

Abstract

Electrostatic control of electronic and structural orderings in two-dimensional materials

by

Ying Wang

Doctor of Philosophy in Applied Science & Technology
and the Designated Emphasis in
Nanoscale Science & Engineering

University of California, Berkeley

Professor Xiang Zhang, Chair

The band structure of a solid crystal is not only dependent on the potential of periodic atoms but also the electron-ion and electron-electron interactions. When dimensionality reduces to two, the latter part becomes prominent owning to greatly enhanced Coulomb interaction between quasiparticles. Meanwhile, the atomic thickness of two-dimensional materials allows full access to the interior of materials through electrostatic doping. Thus, electrostatic doping becomes one main approach to exploit the fundamental physics and practical application in the 2D limit. Among the family of two-dimensional systems, transition metal dichalcogenides (TMDs) are semiconductors with bandgaps, covering a broad spectrum. In addition, new degrees of freedom, such as topological edges and valley index, are found in TMDs and open the door to a new generation of energy-efficient optoelectronic devices carrying more information.

This dissertation first presents optimal thermoelectric effect in TMDs, simultaneously optimizing Seebeck coefficient and electrical conductivity. Even though both of them are determined by the electronic structure of the material, large Seebeck coefficient requires a large asymmetry near Fermi level, opposite to that for electrical conductivity. We employed electrostatic doping to lift up Fermi level and balance this tradeoff. And a recorded-high power factor up to 8.5 mW m^{-1} K^{-2} at room temperature was reported here due to its large effective mass and unique density of state under strong quantum confinement. Additionally, Seebeck coefficient at various temperatures reveals the phonon-limited scattering mechanism at two-dimensional materials. If limiting the carrier density to a low level, the electrical conductivity gives a carrier hopping length around 3nm, which indicates the density of active defects inside. The demonstrated high, electronically modulated power factor in 2D TMDCs holds promise for efficient thermoelectric energy conversion. And the discoveries of carriers' scattering and transport mechanisms are significant to understand quasiparticles' interaction at low dimensionality.

When the density of quasiparticles goes beyond critical density, quasiparticles not

only impact electronic structure but also have the possibility to reconstruct the configuration of lattice. For the first time, we demonstrated monolayer molybdenum ditelluride ($MoTe_2$) reforms form hexagonal phase to monoclinic one through electrostatic doping. A hysteretic behavior has been observed, which is a feature of structural changes as well as the existence of kinetic barrier. Microscopically, the crystal orientation of the electrostatic induced monoclinic phase is found to be consistent with the original crystal orientation of hexagonal phase. It leads to the reversibility of the structural phase transition in terms of both phases and orientation. This discovery opens new possibilities for developing phase-change memory based on atomically thin membranes. The carrier density (metallicity) is also shown to greatly affect the photoluminescence efficiency by controlling the pathway of exciton recombination and hence improves the performance of optoelectronics.

Table of contents

Abstract 1
Table of contents i
List of figures iii
List of tables vi
Acknowledgments vii
1 Introduction 1
1.1 Quasiparticles in solid crystals 1
1.2 Electrostatic controlling of quasiparticles 3
1.3 Two-dimensional materials 4
1.4 Structure of the dissertation 9
2 Enhanced thermoelectricity through quasi-particles 10
2.1 Introduction to thermoelectricity 10
2.2 Device design and measurement setup 12
2.3 Optimal power factor as a function of carrier density 16
2.4 Analysis of DOS and band structure 20
2.5 Scattering mechanism in MoS_2 23
2.6 Electrical properties of MoS_2 26
2.7 Mott variable range hopping in MoS_2 29
2.8 Exclude the impact of Joule heating on temperature distribution 33
2.9 Conclusion 37
3 Structural phase transition controlled by large population of quasi-particles 38
3.1 Structural phase transition in two-dimensional materials 38
3.2 Electric-double-layer field-effect transistor 39
3.3 Experimental design and device fabrication 40
3.4 Demonstration of phase transition through electrostatic doping 42
3.5 Hysteresis and Reversibility of phase transition 46
3.6 Hall measurement and mechanism discussion 48
3.7 Preservation of crystal orientation during phase transition 50
3.8 Uniformity during phase transition 53
3.9 Exclude other possibilities that induce phase transition 57
3.10 Summary and outlook 62

4 Quantum yield optimization through electrostatic approach 64
4.1 Introduction 64
4.2 Experimental design and PL enhancement 67
4.3 Summary and Outlook 70
5 Conclusion and outlook 71
5.1 Nano-engineering of two-dimensional materials 71
5.2 Microscopic mechanism and dynamics of structural phase transition 71
5.3 Quasiparticles in other low-dimensional orderings 72

List of figures

Figure 1-1: Band gap of $Al_XGa_{1-X}As$ as weight of Al changes. 3

Figure 1-2: configuration of metal-oxide-semiconductor (MOS) structure. 4

Figure 1-3: Schematics of Van de Waals materials. 5

Figure 1-4: The density of states in 0-, 1-, 2- and 3- dimensional materials. 6

Figure 1-5: Real-space representation of excitons in 3D and 2D. 7

Figure 1-6: Van der Waals heterostructures. 8

Figure 1-7: Field-effect transistor using stacked two-dimensional materials for all of the components. 8

Figure 1-8: Misoriented honeycomb lattices. 9

Figure 2-1: Schematic of Seebeck effect. 10

Figure 2-2: carrier concentration dependence of *ZT, S, σ* and *κ*. 12

Figure 2-3: Schematics of thermoelectric device. 13

Figure 2-4: Scanning electron micrograph of a thermoelectric device. 14

Figure 2-5: Thickness dependence of Raman spectra of MoS_2 and confocal image of a monolayer MoS_2 thermoelectric device. 15

Figure 2-6: AFM measurement of monolayer and bilayer MoS_2. 16

Figure 2-7 Electrical conductivities and Seebeck coefficients as a function of gate voltage for mono-, bi- and tri-layer MoS2. 18

Figure 2-8: Powerfactor, as a function of gate voltage, ... 19

Figure 2-9: Saturation of powerfactor in MoS_2. 19

Figure 2-10: Comparison of thermoelectric performance of monolayer and bilayer MoS2 with traditional thermoelectric materials. 20

Figure 2-11: QP band structure of pristine monolayer and bilayer of MoS_2 calculated at GW level. 21

Figure 2-12: Calculated DOS of pristine monolayer MoS_2 as a function of the energy difference from the CBM in the K valley. 22

Figure 2-13: Calculated DOS of pristine bilayer MoS_2 as a function of the energy difference from the CBM in the K valley. 23

Figure 2-14: Phonon scattering mechanism in monolayer revealed through Seebeck coefficient. 25

Figure 2-15: Phonon scattering mechanism in bilayer revealed through Seebeck coefficient. 26

Figure 2-16: The measured field-effect mobilities of monolayer, bi- layer, and trilayer samples as a function of back gate voltage Vg. 27

Figure 2-17: High Resolution Scanning Electron Micrographs (HR-SEM images) of 'defective' samples. 28

Figure 2-18: HR-SEM images of representative clean samples. 29

Figure 2-19: Temperature-dependent electrical conductivity at different carrider density. 30

Figure 2-20: Temperature-dependent mobility of monolayer MoS_2. 30

Figure 2-21: Phase diagram for thermoelectric transport as a function of temperature and electron concentration. 31

Figure 2-22: Experimental Seebeck Coefficient for 1L-MoS_2 as a function of temperature and applied back-gate voltage. 31

Figure 2-23: Temperature-dependent conductance of monolayer MoS_2 in insulating phase with different gate voltages. 32

Figure 2-24: Variable-Range Hopping (VRH) correlation energy scale T_0 and The localization length ξ, plotted as a function of carrier concentration. 33

Figure 2-25: Resistivity dependence of source-drain current. 34

Figure 2-26: Temperature measurement of MoS_2 device using Raman spectroscopy. 35

Figure 3-1: Crystal structures of the 2H and 1T′ phases of monolayer TMDs. 38

Figure 3-2: Mechanism of electrostatic doping driven phase transition 39

Figure 3-3: Schematis of the EDL-FETs. 41

Figure 3-4: Potential changes in dielectric materials. 41

Figure 3-5: Configuration of monolayer $MoTe_2$ FET with ionic liquid gate. 42

Figure 3-6: Cross section of FET with ionic liquid gate. 42

Figure 3-7: Raman features of pristine 2H-and 1T′ -phase monolayer $MoTe_2$. 44

Figure 3-8: Representative Raman spectra before, during and after phase transition from 2H to 1T' phase. 44

Figure 3-9: Ag mode observed in gate-driven 1T' phase. 45

Figure 3-10: Calculated shift in the Raman peak of the A_g mode of the 1T′ -phase $MoTe_2$ monolayer owing to strain. 46

Figure 3-11: Fitting of the Lorentz function for Raman spectra at different biases. 47

Figure 3-12: Gate-dependent Raman intensity ratios of 1T' over the whole flake. 48

Figure 3-13: Analysis of the mechanism of phase transition from 2H to 1T′ by the Hall effect. 49

Figure 3-14: Angular polarized Raman (A_g mode) pattern on an exfoliated 1T′ -phase $MoTe_2$ monolayer. 51

Figure 3-15: Raman intensity from monolayer $MoTe_2$ as a function of crystal angle. 52

Figure 3-16: SHG intensity from the same monolayer sample as a function of crystal angle. 52

Figure 3-17: top views of 2H (left) and 1T' phases (right). 53

Figure 3-18: Typical gate dependent SHG intensity under forward bias from target monolayer. 54

Figure 3-19: Optical image of a monolayer $MoTe_2$ flake to explore uniformity. 55

Figure 3-20: SHG mapping at several typical voltage biases. 56

Figure 3-21: Spatial distribution of voltage threshold obtained by fitting. 56

Figure 3-22: Raman mapping of phase transition in monolayer $MoTe_2$. 57

Figure 3-23: Thermally induced factors during phase transition. 59

Figure 3-24: Temperature dependence of Raman peaks of monolayer 2H MoTe2. 59

Figure 3-25: Gate dependent SHG on monolayer 2H $MoTe_2$. 60

Figure 3-26: SHG intensity of bilayer sample under gate bias. 61

Figure 3-27: SHG intensity versus excitation energy before and after phase transition. . 62

Figure 4-1: PL image of a MoS2 monolayer before and after treatment. 66

Figure 4-2: MoS_2 with TSFI coating. 67

Figure 4-3: Chemical formula of DEME-TFSI. 68

Figure 4-4: Schematics of redistribution of TSFI- on top of MoS_2. 68

Figure 4-5: Enhancement of PL over 20 times. 69

Figure 4-6: No change of PL at electrons side. 70

List of tables

Table 2-1: summary of properties of band structure.. 27

Table 2-2: the thermoelectric properties of traditional thermoelectric materials in comparison with our MoS2 devices. 37

Acknowledgments

It is my great privilege to thank my mentor Professor Xiang Zhang for the opportunity to conduct research in the very diverse and energetic group, as well as your sharp and timely guidance over the years. Your curiosity and enthusiasm on science always encourage me to expand my horizons. These are invaluable fortune and will be the cornerstones for my future career.

I thank Dr. Kedar Hippalgaonkar and Dr. Yu Ye for helping me launching my first project and training me in fabrication and electronics. I would like to thank Dr. Hanyu Zhu and Jun Xiao for your countless support, in scientific or non-scientific aspects. I appreciate the guidance from Dr. Ziliang Ye, Dr. Xiaobo Yin and Dr. Yuan Wang. And I am also grateful for the talented and warm-hearted colleagues in Xlab and their precious contribution to my research: Dr. Zijing Wong, Dr. Xingjie Ni, Dr. Sui Yang, Dr. Liang Feng, Dr. Cheng Gong, Dr. King Yan Fong, Dr. Mervin Zhao, Yang Xia, Quanwei Li, Siqi Wang and Yousif Alsaid. I treasure our girls' friendship between Xuexin Ren and Dr. Kun Zhang. I thank all the other Xlab members for the enjoyable time we have spent together. In addition, I thank Professor Evan Reed for support and helpful discussion and also Dr. Yao Li for the fruitful collaboration.

Finally, I would like to specially thank my parents and my husband who offered me unconditional love and support. I also give special thanks to my friends, who have my back and are always willing to bear my burden whenever up or down.

1 Introduction

1.1 Quasiparticles in solid crystals

Solid crystals are composed of periodic atoms that glued together through shared electrons in the outer shell. An exact theory for this system is based on solving a many-body Schrödinger equation of the form

$$\mathcal{H}\Psi(\{R_I; r_i\}) = \mathrm{E}\Psi(\{R_I; r_i\}) \tag{1.1}$$

where $\mathcal{H}$ is the hamiltonian of the system, containing the kinetic energy operators

$$-\sum_I \frac{\hbar^2}{2M_I}\nabla_{R_I}^2 - \sum_i \frac{\hbar^2}{2m_e}\nabla_{r_i}^2 \tag{1.2}$$

and the potential energy due to ion-ion, electron-electron and electron-ion interactions. In equations above , $\hbar$ is Planck constant divided by 2π; M_I and m_e are the mass of ion I and electrons, respectively; And E is the energy of the system; $\Psi(\{R_I; r_i\})$ is the wavefunction describing the states of the system; R_I and r_i are positions of ions and electrons.

For potential energy, ion-ion interaction can be described as

$$\frac{1}{2}\sum_{IJ(J\neq I)} \frac{Z_I Z_J e^2}{|R_I - R_J|} \tag{1.3}$$

based on the repulsive force between two ions at position R_I and R_J. And Z_I is the valence charge of this ion (nucleus plus core electrons). Similar forms of potential energy for electron-electron and electron-ion interaction shown in the following:

$$\frac{1}{2}\sum_{ij(j\neq i)} \frac{e^2}{|r_i - r_j|} \tag{1.4}$$

$$-\sum_{iI} \frac{Z_I e^2}{|R_I - r_i|} \tag{1.5}$$

The complete form of $\mathcal{H}$ contains both kinetic energy operator and potential energy. Since in a typical solid crystal, there is a huge difference of mass between ions and electrons (three to five orders of magnitude) and ions are so heavy and at rest that the wave function of system is only explicitly dependent on the electronic degrees of freedom alone. And it is safe to simplify the $\mathcal{H}$ by omitting the quantum mechanical terms for the

kinetic energy of the ions and potential energy for ion-ion interaction. This is known as the Born–Oppenheimer approximation. Therefore, the Hamiltonian of the system becomes

$$\mathcal{H} = -\sum_{i} \frac{\hbar^2}{2m_e} \nabla_{r_i}^2 - \sum_{iI} \frac{Z_I e^2}{|R_I - r_i|} + \frac{1}{2} \sum_{ij(j \neq i)} \frac{e^2}{|r_i - r_j|} \quad (1.6)$$

and the states of the system can be described through variables of electrons $\Psi(\{r_i\})$. Even with this simplification, however, solving for $(\{ri\})$ is an extremely difficult task, because of the nature of the electrons that each electron is affected not only be steady ions but also every other electron in the system. And even more, Pauli exclusion does not allow electrons occupy the same state. People simplified further to make it more practical to get eigenstates of the system in the following.

Essentially assuming that the electrons were non-interacting particles, many-body wavefunction can be expressed as

$$\Psi^H(\{r_i\}) = \phi_1(r_1)\phi_2(r_2) \cdots \phi_N(r_N) \quad (1.7)$$

in which, N is the total number of electrons. $\phi_i(r_i)$ refers to the states of single electron of the system. This approximation is called Hartree approximation. Therefore, the problem simplified into solving the single-particle Schrödinger equation

$$\left[-\frac{\hbar^2}{2m_e} \nabla_{r_i}^2 - \sum_{iI} \frac{Z_I e^2}{|R_I - r_i|} + \sum_{ij(j \neq i)} \langle \phi_j \left| \frac{e^2}{|r_i - r_j|} \right| \phi_j \rangle \right] \phi_i(r_i) = \epsilon_i \phi_i(r_i) \quad (1.8)$$

$$V_{eff} = -\sum_{iI} \frac{Z_I e^2}{|R_I - r_i|} + \sum_{ij(j \neq i)} \langle \phi_j \left| \frac{e^2}{|r_i - r_j|} \right| \phi_j \rangle \quad (1.9)$$

The resulting single-particle equations are supposed to describe the behavior of electrons as independent particles in an external potential V_{eff} defined by the ions, as well as an external field produced by the presence of all other electrons. And exchange energy, caused by Pauli exclusion is further added as a perturbation under mean field approximation to the system and modified the V_{eff}. Therefore, we could expect very different behavior of electrons in crystal, compared to those in vacuum, such as velocity and phase. Electrons in crystal are assigned with an effective mass and called as quasiparticle. The eigenstates, in which energy is dependent on momentum, form the band structure of the crystal that allows quasiparticles to occupy. Intuitively thinking, any method that can modify V_{eff}, changes the band structure of solid crystal and hence affect properties of them accordingly. And accessing to V_{eff} becomes one significant way to understanding fundamental physics in solid crystals.

1.2 Electrostatic controlling of quasiparticles

To modify V_{eff} , one could change both of the magnitude and periodicity of potential provided by periodic ions. In order to manipulate them to different extents, chemical doping, growth of alloys and hetero-structures [1–4] are accessible to satisfy the whole spectra. For example, $Al_XGa_{1-X}As$ is an arbitrary alloy, composed of GaAs and AlAs and the X in the formula is a number between 0 and 1. The bandgap of the alloy [5] varies from 1.42 eV (GaAs: X=0) and 2.16 eV (AlAs: X=1) and enables broad use in laser diodes with various wavelength as well as mirrors in VCSELs (see in Figure 1-1). However, gluing materials with distinct lattice constants inevitably associate with lattice mismatch and result in large strain non-uniformly, which is detrimental for electrical and optical applications.

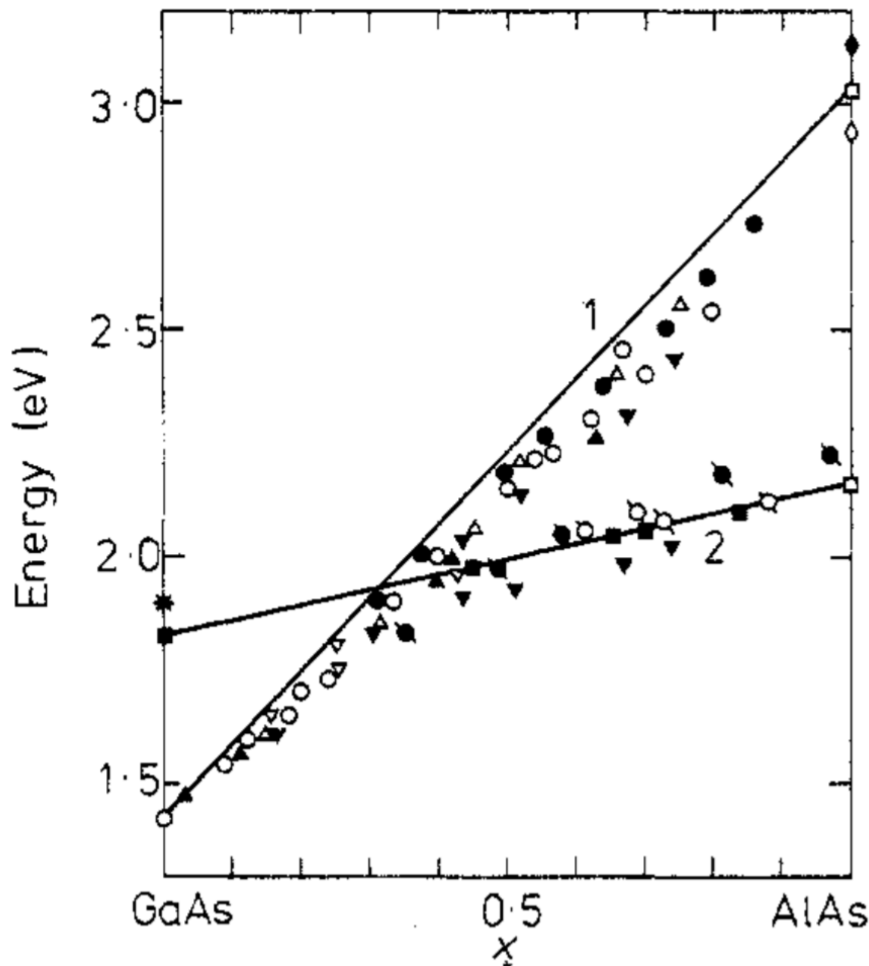

Figure 1-1: Band gap of $Al_XGa_{1-X}As$ as weight of Al changes. Copyright IOP Publishing, LTD

A more dynamic and controllable approach to control V_{eff} is the manipulation of the density of quasiparticles, which influences the second part of potential, such as exchange-

perturbation or modification of the energy level of quasiparticles, by filling band levels and moving Fermi level. The former usually occurs at high-density level of quasiparticles while the latter is achievable in moderate range through electrostatic doping, shown in Figure 1-2. Essentially, it can be achieved in metal-oxide-semiconductor (MOS) structure, where two metal and dielectric layers are stacked in sequence on top of semiconductor. As the middle material is dielectric, this structure is equivalent to a planar capacitor, with one of electrode replaced by a semiconductor. When a voltage applied across a MOS structure, two layers of quasiparticles with opposite charges, accumulate on two ends of dielectrics. And the density of quasiparticles changes on the very surface of semiconductor and this method is called as electrostatic doping. Unlike chemical doping, which usually inducing lattice distortion [6], electrostatic doping is a much cleaner approach to control carrier density so that it eliminates the possible side effects of introducing other elements. Since electrostatic doping used as a switch for the conductive channel on the surface of semiconductors, it has been greatly employed in the field-effect transistors and digital integrated circuits contain millions of those [7].

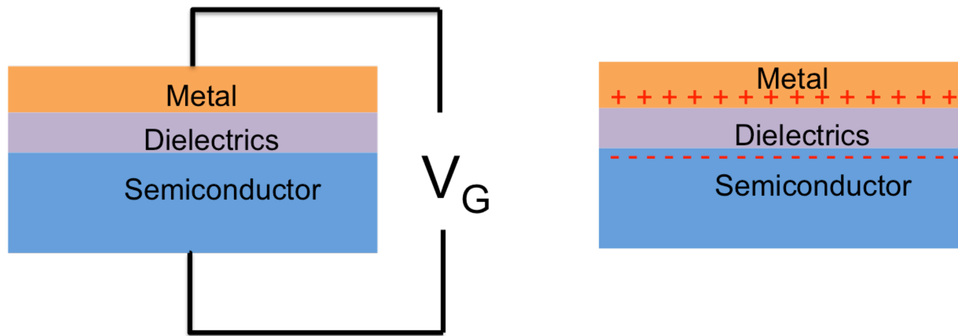

Figure 1-2: configuration of metal-oxide-semiconductor (MOS) structure. Applying the voltage across the metal and semiconductor, capacitor-like two layers of charges are accumulated on the surface of metal and semiconductor.

As we know, the redistribution of quasiparticles by electrostatic doping is confined on very top of material due to the screening effect that the high-concentrated charged carriers exhibits electric field, which is reverse to external electric field to screen it out. Hence, no electric field exists in deeper region to drive the movement of carriers. Such screening effect limits the depth of modification and makes it difficult to explore physics of the whole bulky body of materials under dynamic alteration of quasiparticle's density.

1.3 Two-dimensional materials

In comparison, materials with atomic thickness do not have this limitation since its thickness can be even smaller than that of doping depth. The interior of the materials under the manipulation of quasiparticles is thus fully accessible in terms of observation and manipulation [8–10]. Previously, several quasi-2D systems such as two-dimensional electron gas (2DEG) at the interface of semiconductor-semiconductor, semiconductor-insulator or insulator-insulator heterostructures [11,12] have been studied for decades. But prevalent dangling bonds and defects at the interface drastically complex the roles of ions and quasiparticles due to interface reconstruction and defect chemistry. In recently years,

Van der Waals materials [13,14] shown in Figure 1-3, composed of atomic layers through weak Van der Waals interaction in between, attract great attentions due to its 2D nature in each layer. By mechanical exfoliation, truly two-dimensional materials are obtained and being chemical stable without no dangling bond [15]. More than 0.1 carrier per unit cell can be injected through electrostatic doping [9]. Without inducing non-uniformity or local strain, it provides a good plotform for a lot novel research, such as quantum and topological transport as well as many-body problems at 2D limit.

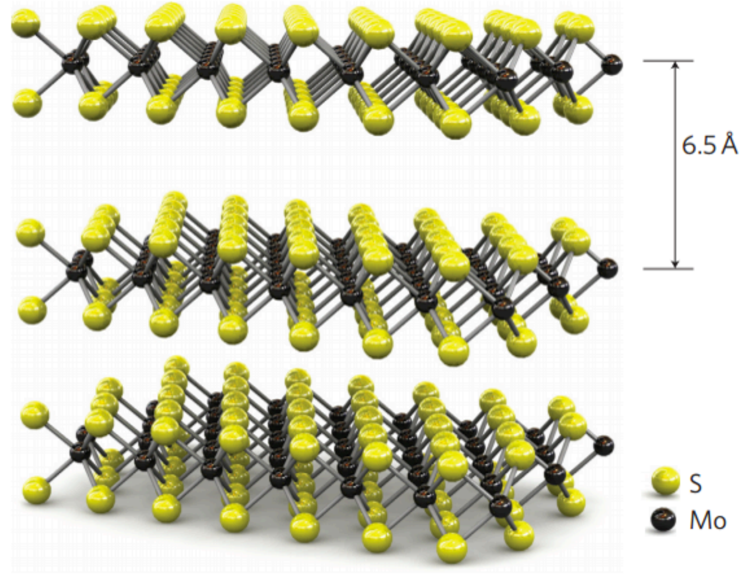

Figure 1-3: Schematics of Van de Waals materials. There is weak Van de Waals force between layers and hence mechanical force can peel single layer off. Reprinted from Ref. [16], Nature Publishing Group.

Besides its chemical advantages, the strong quantum confinement in two-dimensional material leads to the unique step shape [16] for the density of possible states of quasiparticle at a given energy (density of states, DOS), defined as below:

$$D_n(E) = \frac{d\Omega}{dE} \propto m^{*\frac{n}{2}} E^{\frac{n}{2}-1} \tag{1.10}$$

where $d\Omega$ is the number of possible states within the interval of dE and $m*$ is the effective mass. DOS changes qualitatively for various dimensionality n [18] (see in Figure 1-4). Since the strength of quasiparticles' interactions are proportional to the density of states of the participants, we expect the impact of quasiparticles in two-dimensional materials on ground state of the system or excited states are stronger than their 3D counterpart, especially for energy levels crossing the step edges.

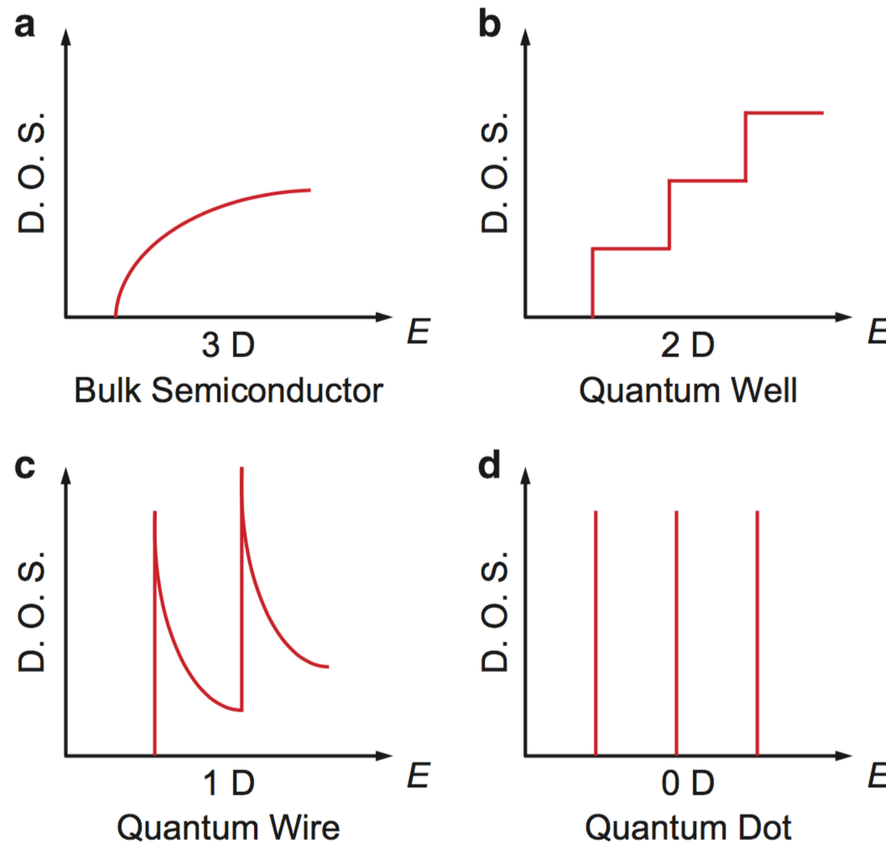

Figure 1-4: The density of states in 0-, 1-, 2- and 3- dimensional materials. Reprinted with permission from John Wiley and Sons.

Meanwhile, the suppression of screening effect and stronger Coulomb interaction between quasiparticles are characteristic in two-dimensional materials [19–21]. In many traditional systems, the relative dielectric constant ε_r is large and reduces the Coulomb interaction of quasiparticles [22]. For example, electron-hole pairs (excitons) in 3D system cannot be stabilized at room temperature because thermal fluctuation can easily break the bond [23]. But for 2D material, typically supported by an oxide substrate, the average $\varepsilon_{r,}$ where electric fields of quasiparticles extend over is close to 1 since at least one side of 2D materials is almost vacuum [24], shown in Figure 1-5. Benefitting from this, binding energy of electron-hole pairs gets one order of magnitude improvement compared to its 3D counterpart [25]. This effect releases cryo-temperature requirement for studying excitonic effect to room temperature (RT) and encourages exploration on RT-exciton condensation [26,27] and RT-operated excitonic-related optoelectronic application [28]. Moreover, the screening effect is controllable through quasiparticle density and as a result, the long-range Coulomb interaction and exchange effect in 2D material were manipulated to reconstruct single-particle band structure in a range of 500 meV [29,30].

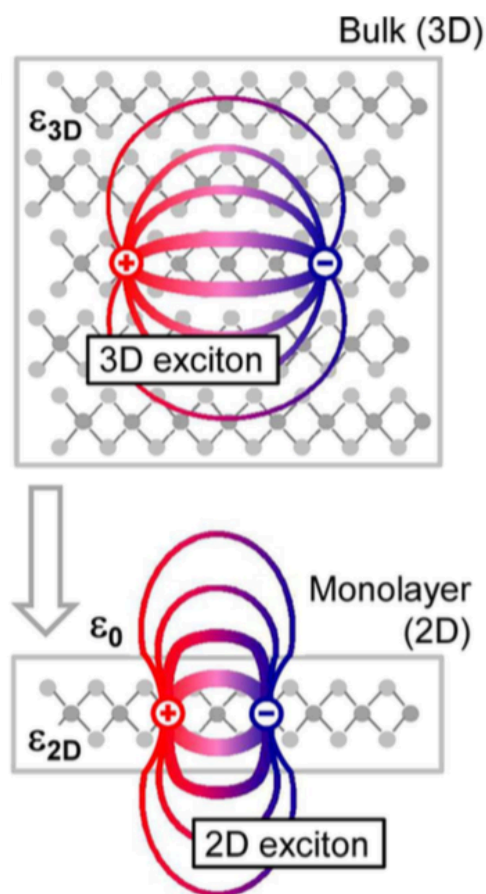

Figure 1-5: Real-space representation of excitons in 3D and 2D. The changes in the dielectric environment are indicated schematically by different dielectric constants ε_{3D}, ε_{2D}, and the vacuum permittivity ε_0. Reprinted from ref. [31] with permission American Physical Society.

Moreover, the family of Van der Waals materials shows its diversity covering the whole electrical and optical range, from insulators with large band gap to metals. With the fact that monolayers can be arbitrarily stacked with the weak interlayer binding [17,32–34], it opens the door to engineer artificial heterostructures with versatile physical properties and functionalities (see in Figure 1-6). For instance, people have demonstrated that all components in field effect transistors and light emitting diode can be 2D materials and these devices are atomic thin with less energy consumption [35,36] (shown in Figure 1-7). When looking into microscopic interaction between layers, one layer of atoms sit on the top of a periodic potential from the bottom layer of atoms and this heterostructure forms superlattice with a longer periodicity and leads to a new band structure [37,38] (see in Figure 1-8). Within this artificial band structure, the transition from Mott insulator to superconductivity has been repeated surprisingly to shed light on the mechanism of superconductivity [39]. Therefore, considering the large tunability of quasiparticls, Van der Waals material or its heterostructure is unique platform to exploit both fundamental and practical properties while changing it from insulator to metal.

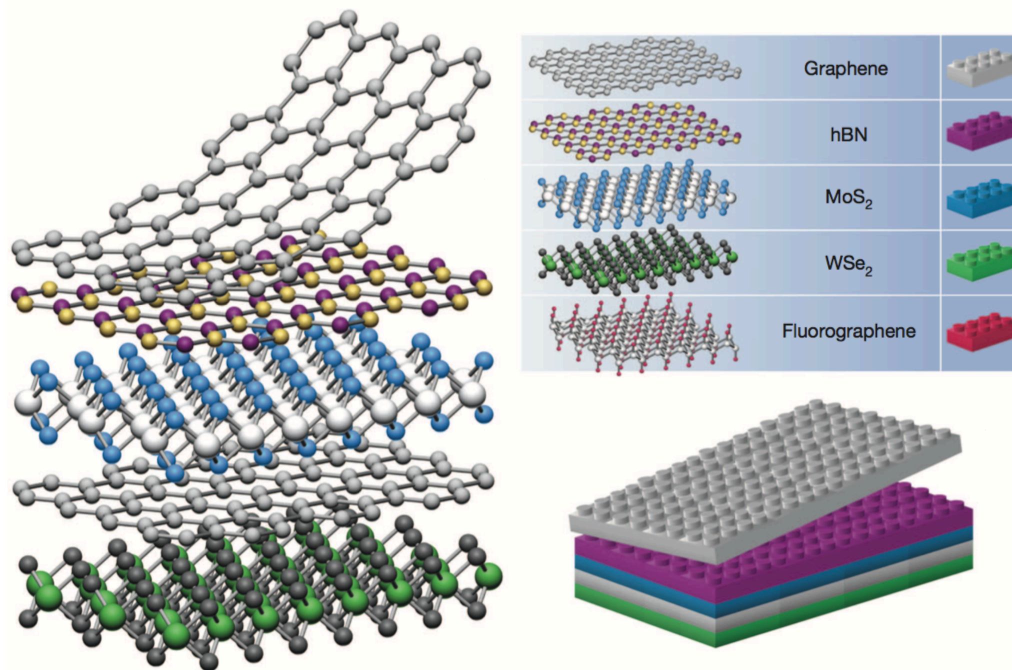

Figure 1-6: Van der Waals heterostructures. If one considers each 2D layer to be analogous to Lego block (right panel), the construction of a huge variety of layered structures becomes possible. Reprinted from Ref.[32] with permission from Springer Nature.

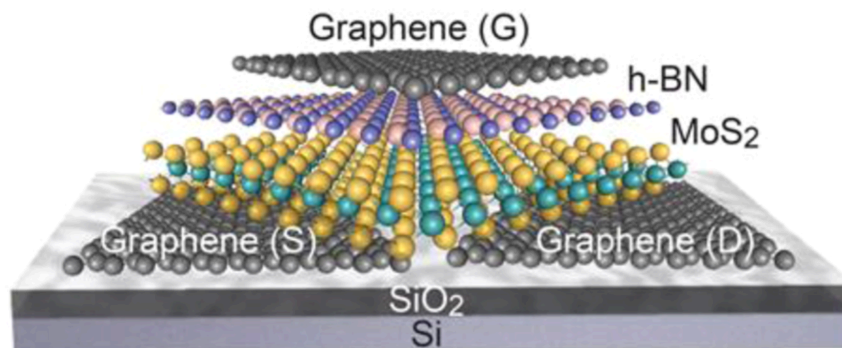

Figure 1-7: Field-effect transistor using stacked two-dimensional materials for all of the components. Reprinted from Ref. [36] with permission from American Chemical Society.

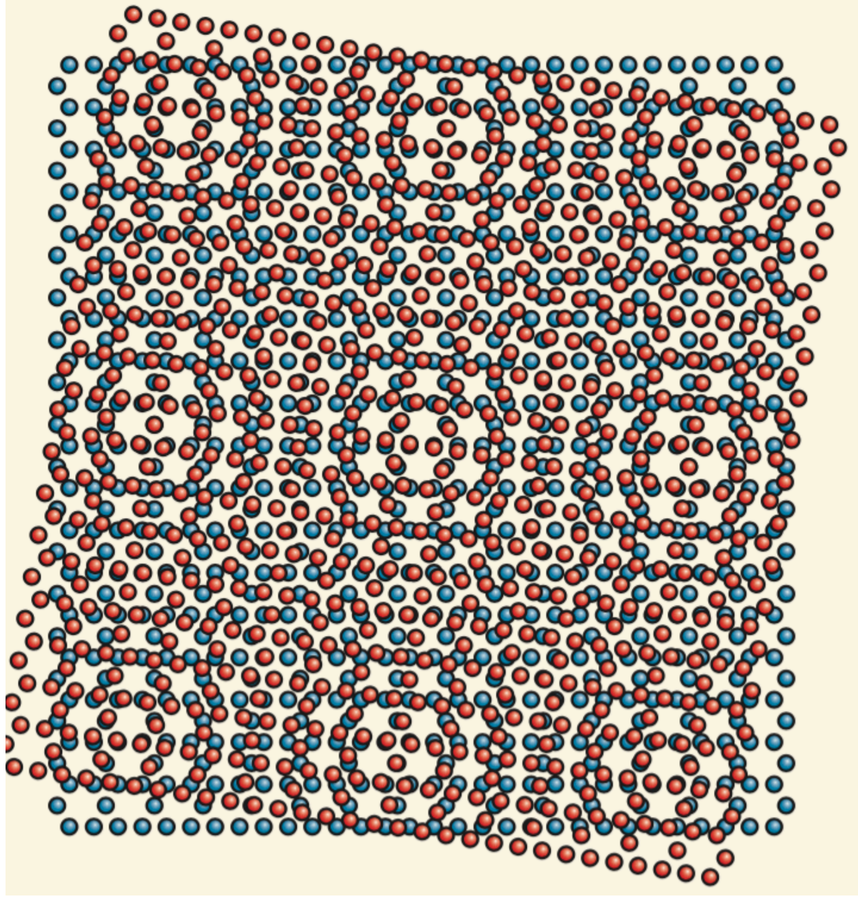

Figure 1-8: Misoriented honeycomb lattices. Lattices rotated by 9°. There is a periodic pattern of points in space at which atoms from the two layers are nearly on top of each other. Reprinted from Ref. [38] with permission from Spring Nature.

1.4 Structure of the dissertation

Based on the discussion above, two-dimensional materials are ideal research platforms for exploring quasiparticles' interaction and their significant influence on fundamental physics, owning to ultrahigh density of quasiparticles and less screening. It potentially enables induced electronic, optical and structural effects. This thesis presents three works in line with these directions in the following sequence:

- Chapter 2: electrical and thermoelectric properties in two-dimensional material, engineered through manipulation of population of quasiparticles [40]
- Chapter 3: structural phase transition induced by ultrahigh density of quasiparticles [41]
- Chapter 4: enhancement of quantum yield of photoluminescence through defect compensation with quasiparticles

2 Enhanced thermoelectricity through quasi-particles

2.1 Introduction to thermoelectricity

The thermoelectric effect is the direct conversion of temperature differences to electric voltage. A thermoelectric material creates voltage through non-uniformity of temperature (see in Figure 2-1). Assuming that a temperature gradient ΔT is established along the material, it generates a potential difference ΔV between the ends. The Seebeck coefficient, S, is defined as the ratio of ΔV to ΔT.

$$S = \Delta V/\Delta T \tag{2.1}$$

The mechanism behind this effect is that the temperature gradient causes charge carriers to diffuse from the hot side to the cold side and this redistributed carriers exhibits an electrical field inside and hence builds up a voltage. And this effect has been widely used to generate electricity [42], measure temperature [43] or change the temperature of objects [44].

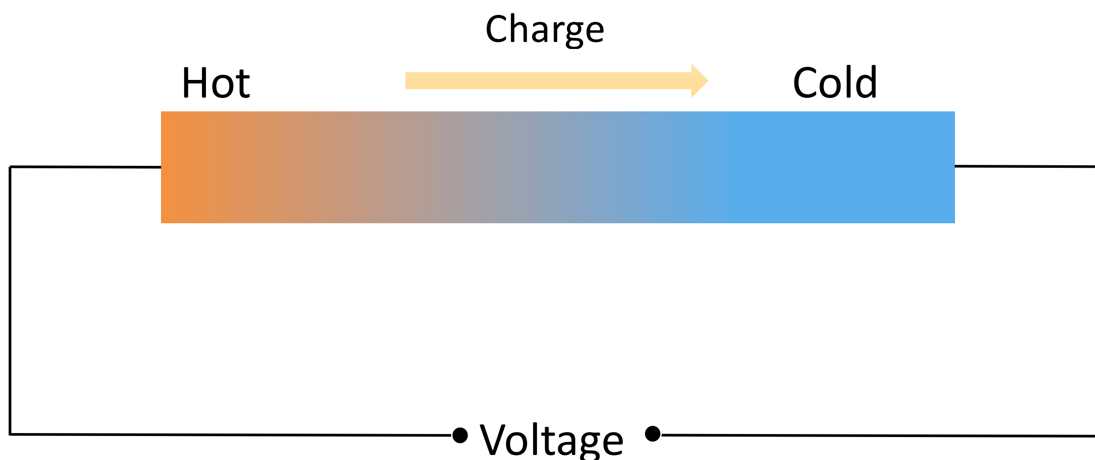

Figure 2-1: Schematic of Seebeck effect.When a temperature gradient applied along the material, there is a voltage built between two ends.

Considering the efficiency of thermoelectric device, not only Seebeck coefficient but also electrical conductivity and thermal conduction should be taken into account. Electrical conductivity determines the amount of energy that losses into Joule heating. Meanwhile, good thermal conductivity decreases the efficiency, since it leads to undesired thermal exchange between hot and cold sides of a thermoelectric device. Taking these factors into account, the power generation efficiency (η) proportionally depends on figure of merit (ZT), which is dimensionless and as a symbol of the thermoelectric performance of a material [45]. And,

$$ZT = (S^2\sigma/\kappa)T \tag{2.2}$$

In other words, to get high efficiency of converting heat to electricity, materials with good figure of merits (high *ZT*) are required. More specifically, large Seebeck coefficient (*S*) is necessary to produce large voltage and good electrical conductivity (σ) is also required to minimize Joule heating, while thermal conductivity (κ) should be minimized to maintain a large temperature gradient. *T* is thermodynamic temperature. However, these three requirements cannot be met simultaneously since they are strongly coupled with each other, i.e. improving one parameter may degrade the other. For example, in order to get better electrical conductivity, people usually increase carrier concentration inside of material (see in Figure 2-2). High density of carriers, as another important source that contributes to thermal conductivity, gives higher thermal conductivity and hence reduces *ZT,* opposite to our goal. Due to this trade-off, *ZT* cannot go to the infinite and there is an optimal value for each material [46].

In order to increase *ZT,* much effort has been made to decrease thermal conductivity by inducing nanostructures, resonant doping or multivalley scattering [47–49]. On the other hand, for a given thermal conductivity and temperature, *ZT* is also determined by the electronic structure of material through $S^2\sigma$, known as powerfactor. Engineering electronic structure becomes an alternative way to maximize *ZT*. However, tuning the electronic structures of traditional bulk materials involves complex chemical doping [50,51], making the optimization of figure of merit difficult to control. Low dimensional materials, with large quantum confinement and much less screening effect than bulk, allow electrostatic doping to change electronic structure dynamically [9]. It opens a more practical route to optimize figure of merit.

Transition-metal dichalcogenides (TMDs), as a typical class of 2D materials, includes the semiconducting MX_2 (M = Mo, W; X = S, Se, Te) [52,53]. In each van der Waals layer, a hexagonal M plane is sandwiched between two hexagonal X planes through ionic–covalent interactions in a trigonal prismatic arrangement as shown in Figure 1-3. The latest research shows that the thermal conductivity is ultralow in this material due to the enhanced scattering of phonons under strong quantum confinement [50] and electronic structure of TMDs indicates a large Seebeck coefficient because of step-like DOS in 2D [55].Therefore, TMDs are potential to be good candidate as thermoelectric materials with good efficiency.

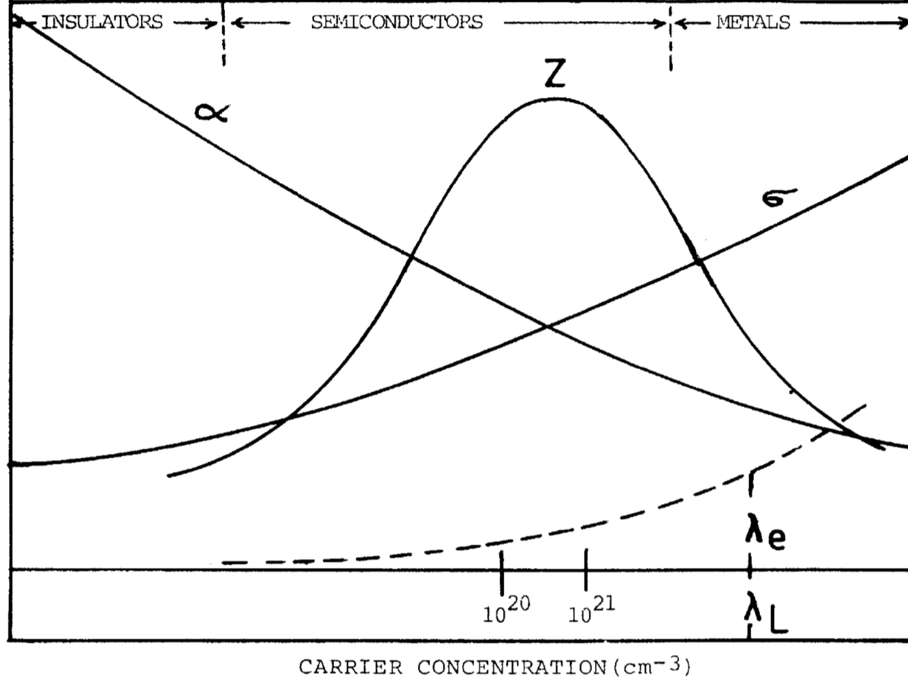

Figure 2-2: carrier concentration dependence of *ZT, S, σ* and *κ.* Thermal conductivity noted as λ [56]. Reprinted permission from Elsevier.

2.2 Device design and measurement setup

In order to optimize the powerfactor in 2D MoS_2 through electrostatic doping, we designed a device that could perform simultaneous measurements of the Seebeck coefficient (*S*) and two-probe electrical conductivity (σ) under various gating. In brief, the temperature gradient ΔT is created by a metal resistive element that is electrically isolated from the MoS_2 flake (see in Figure 2-3). And two metal electrodes are patterned on two ends of the MoS_2 flake to measure the temperature difference. This pair of electrodes is also employed to measure the open circuit voltage, V_{OC} to obtain the Seebeck coefficient $S \equiv -V_{OC}/\Delta T$. Two-probe electrical conductivity was measured by passing a current (I_{DS}) through the them as well and measuring the drain-source voltage (V_{DS}). Another pair of electrodes was patterned for four-probe electrical conductivity. Electrostatic doping was controlled through the thermally grown SiO2 as dielectrics gate. Details about the process of sample preparation and fabrication are discussed in the following session.

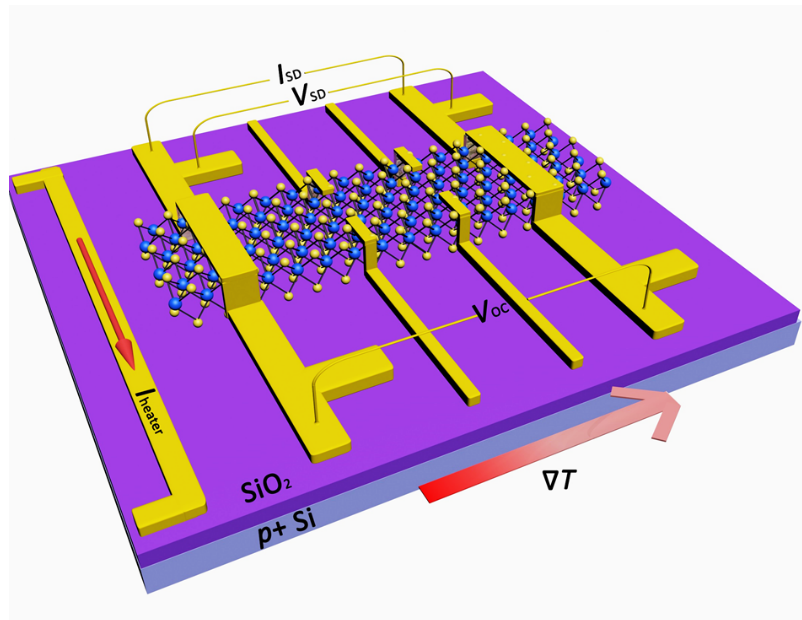

Figure 2-3: Schematics of thermoelectric device. Based on this configuration, simultaneous measurement of Seebeck coefficient and electrical conductivity are conducted. The illustration shows monolayer MoS_2, while the same device configuration was used to measure the bi- and tri-layer MoS_2, placed on thermally grown SiO_2 on a p+ Silicon substrate. Two-probe electrical conductivity was measured by passing a current through the device (I_{DS}) and measuring the drain-source voltage (V_{DS}) at each temperature. In order to measure the Seebeck $S = -V_{oc}/\Delta T$, current was passed through the heater to generate a temperature gradient ∇T, while the open circuit voltage (V_{OC}) was measured through the electrodes as well.

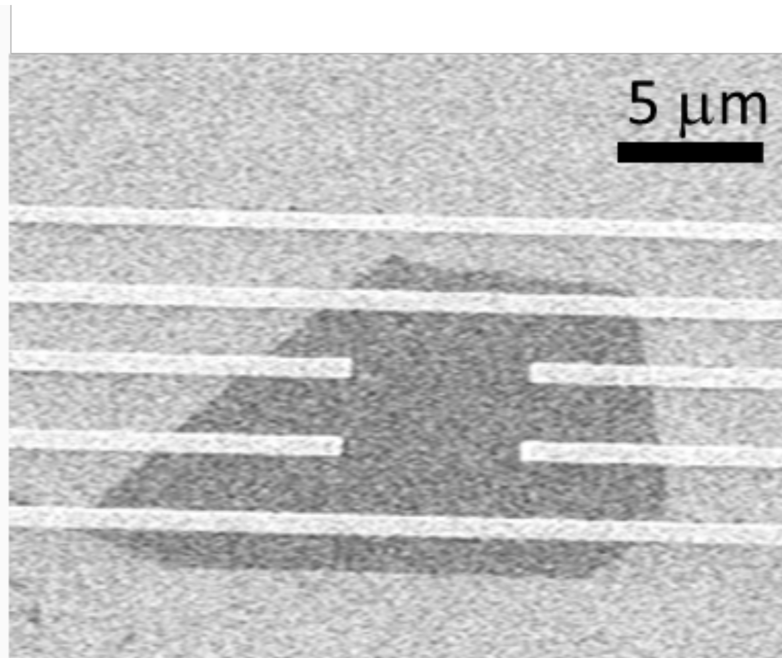

Figure 2-4: Scanning electron micrograph of a thermoelectric device. Note that the hall-bar electrodes were used to obtain the ratio of the two-probe to the four-probe electrical conductivities to estimate the contribution due to contact resistance at each temperature.

To achieve the device for power factor measurement, thin layers are prepared firstly. Exfoliated samples are obtained using the scotch-tape method by cleaving a bulk molybdenite. We exfoliate the samples onto 275 nm thermally grown SiO_2 on a highly doped p-Si substrate. MoS_2 flakes are visible on the sample under an optical microscope and the single, bi- or tri-layer samples are selected based on characterization due to optical contrast photoluminescence imaging and Raman Spectroscopy (see in Figure 2-5). The separation between Raman-active modes A_{1g} and E^1_{2g} decreases as the layer thickness decreases from three layers to one layer, as has been reported in literature [57–59]. The separation of the A_{1g} and E^1_{2g} peaks are 18 cm^{-1} for the monolayer, 22 cm^{-1} for the bilayer and 24 cm^{-1} for the trilayer (Figure 2-5(a)). Moreover, the monolayer MoS_2 exhibits strong photoluminescence, due to the direct bandgap nature (Figure 2-5(b)). [60]

In order to get the real thicknesses for monolayer and bilayer to guarantee the accuracy of our experiements, we also conduct AFM measurements. AFM images (Figure 2-6) were acquired from Dimension 3100 scanning probe microscope under non-contact mode using probes with tip radius less than 10 nm. The thickness was measured from the step between the MoS_2 crystal and the underlying SiO_2 substrate. The scanning parameters have been carefully selected to yield the true thickness due to the difference of tip-sample interaction over the substrate and the crystal [61]. Representative monolayer and bilayer samples show a thickness of 0.66 nm for the monolayer (with a rms roughness less than 0.2 nm) and 1.31 nm for the bilayer (also with a rms roughness less than 0.2 nm) respectively, similar to reported values in literature [14,62,63]. After identifying thickness of each flake, we use standard electron-beam lithography to pattern the geometry of all metal electrode and follow with one more step of electron-beam deposition. After this,

PMMA, photoresist used in electron-beam lithography is removed by acetone. Annealling in a high vacuum of 5×10^{-6} torr at 475 K for 1 hour, is used to remove the tape residue, particles and absorbed water molecules from the surface and reduces the surface roughness. All devices were prepared after following identical fabrication steps and a typical SEM image for real devices is shown in Figure 2-4.

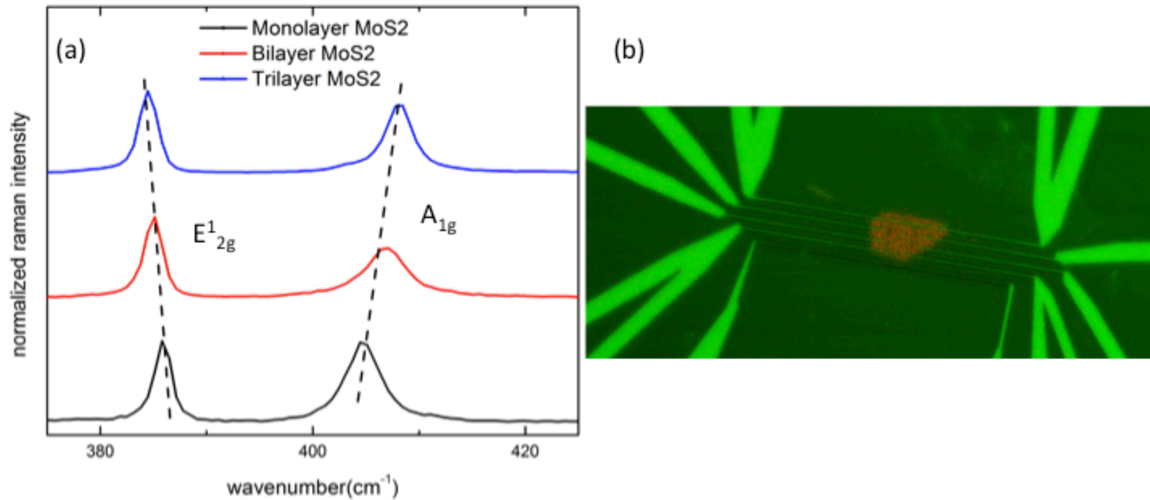

Figure 2-5: Thickness dependence of Raman spectra of MoS_2 and confocal image of a monolayer MoS_2 thermoelectric device. In (a), the Raman spectrum of MoS_2 has two prominent peaks: an in-plane ($E1_{2g}$) mode and an out-of-plane (A_{1g}) mode. As MoS_2 becomes monolayer, these two modes evolve with thickness. The in-plane mode upshifts to 386 cm^{-1} and the out-of-plane downshifts to 404 cm^{-1}. The difference of these two modes (~18 cm^{-1}) can be used as a reliable identification for monolayer MoS_2. As in (b), The monolayer MoS_2 shows strong photoluminescence, due to the direct bandgap property. The red channel is the photoluminescence channel, indicating the shape of monolayer MoS_2. The green channel is the scattering channel of the incident laser, indicating the geometry of the device.

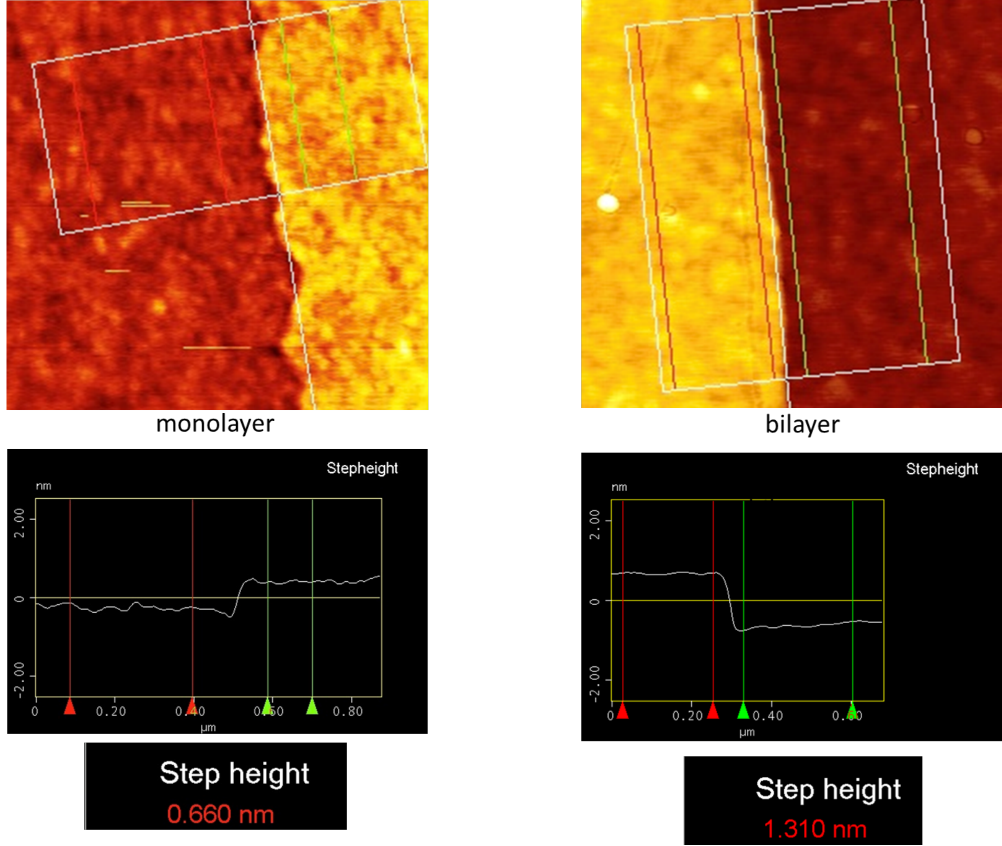

Figure 2-6: AFM measurement of monolayer and bilayer MoS_2.The thickness of monolayer is about 0.66 nm and the thickness of bilayer is about 1.31 nm.

On the devices of mono-, bi-, tri-layers MoS_2, the heat generated from the heater line firstly creates a temperature gradient across the TMDC sample, given by $Q \propto I_{DC}^2 R_{htr} \propto \Delta T$. The DC current, I_{DC}, passing through the resistive line is up to 20mA. The electrodes patterned on two sides of the sample function both as probes for electrical measurements and for local temperature measurement. For each electrode, the resistance is given by $R_{hot/cold} \propto \Delta T_{hot/cold}$. Then, the temperature difference across the device is calibrated as $\Delta T = \Delta T_{hot} - \Delta T_{cold}$, where $\Delta R_{h/c} = \alpha_{h/c} \Delta T_{h/c}$ obtained at every global temperature. And the electrical conductivity (σ) of the channel material could be derived form the voltage difference between the two electrodes while sending a constant current into the channel materials. The open circuit voltage across the device, V_{oc} as a function of heating current is then determined, from which the Seebeck coefficient of the device can be deduced as $S = -V_{oc}/\Delta T$.

2.3 Optimal power factor as a function of carrier density

In order to optimize powerfactor through electrostatic doping, the Seebeck coefficient and electrical conductivity of 2D MoS_2 are measured as a function of carrier concentration tuned by a back gate. And at each gate voltage, both of these parameters are measured simultaneously using the measurement method discussed above. The electron

concentration is given by $n = C_{ox}/e \cdot (V_g - V_t)$, where C_{ox} is the capacitance between the channel and the back gate, e is the electron charge, V_g and V_t are the gate and threshold voltage, respectively. A typical I_{sd}-V_g curve for each device was measured to estimated the capacitance and electron density at various gate voltages.

The measured electrical conductivities and Seebeck coefficients of monolayer, bilayer and trilayer MoS_2 follow behavior akin to an extrinsically doped semiconductor (Figure 2-7). We found that with increasing electron concentration, the magnitude of the Seebeck coefficient drops. This effect is well expected because the Seebeck voltage is proportional to the asymmetry of occupied density of states around the Fermi level in the energy diagram [64,65] and is defined as

$$S = \frac{-\pi^2}{3e} k_B^2 T \frac{1}{\sigma} \left(\frac{d\sigma}{dE} \right) \Bigg|_{E_F} \tag{2.3}$$

where $k_B = 86.2$ μeVK^{-1} is the Boltzmann constant. As carrier density increases, the Fermi level is pushed closer to the conduction band minimum (CBM) and hence the magnitude of the Seebeck coefficient drops. However, electrical conductivities in both mono- and bilayer follow the opposite trend and increases as carrier concentration increases. The electrical conductivity is determined by:

$$\sigma = en\mu \tag{2.4}$$

in which, e and μ are charge and mobility of electrons, respectively.

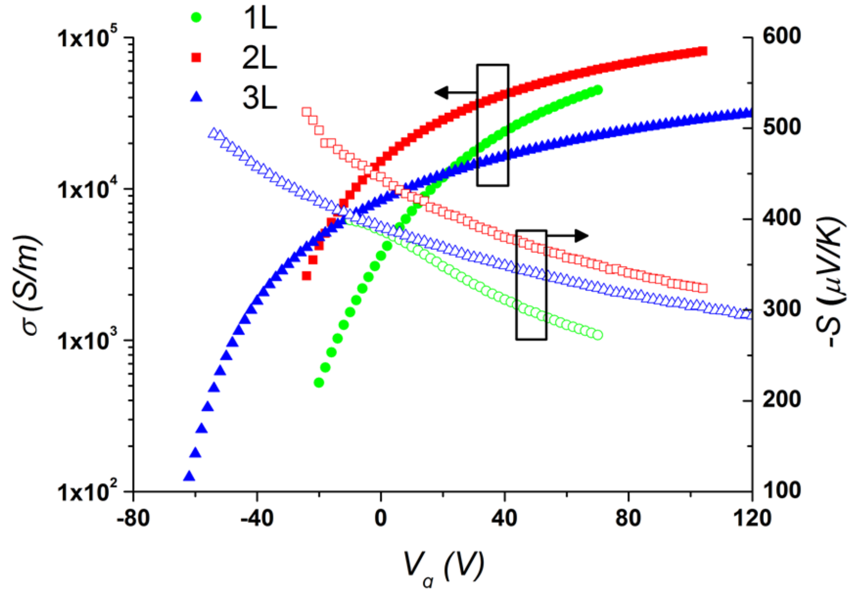

Figure 2-7 Electrical conductivities and Seebeck coefficients as a function of gate voltage for mono-, bi- and tri-layer MoS_2. As the carrier concentration $n \propto (V_g - V_t)$ increases, σ increases and the magnitude of S decreases. S is negative, which confirms that the sample is n-type.

By combining both electron-density-dependent Seebeck coefficient and electrical conductivity, electron-density-dependent powerfactors of mono-, bi-, tri-layers MoS_2 are summarized in Figure 2-8. The bilayer device exhibits the largest powerfactor $S^2\sigma = 8.5$ $mWm^{-1}K^{-2}$ at V_g = 104 V equivalent to a high electron concentration $n_{2D} \sim 1.06\times10^{13}$ cm^{-2}. The magnitude of the powerfactor is expected to reach a peak and then drop for even higher carrier concentrations as the increasing electrical conductivity is offset by the decreasing Seebeck coefficient [64]. However, For MoS_2 samples shown here, the powerfactor does not peak, as this optimum carrier concentration is expected to occur at an even higher gate voltage ($n_{2D} \sim 1.31\times10^{13}$ cm^{-2} equivalent to a bulk concentration of $n_{3D} \sim 1\times10^{20}$ cm^{-3} – obtained by considering a bilayer thickness of 1.3 nm), which is limited by the electrical breakdown of the gate oxide in our experiment. And for devices with better quality of gate oxide, additional two monolayer samples (Figure 2-9) show saturation of the powerfactor at even higher gate voltages (carrier concentrations), close to 1-1.5$\times10^{20}$ cm^{-3}, whose behavior similar to a degenerately doped semiconductor. It reveals the possibility to increase the power factor higher with better devices.

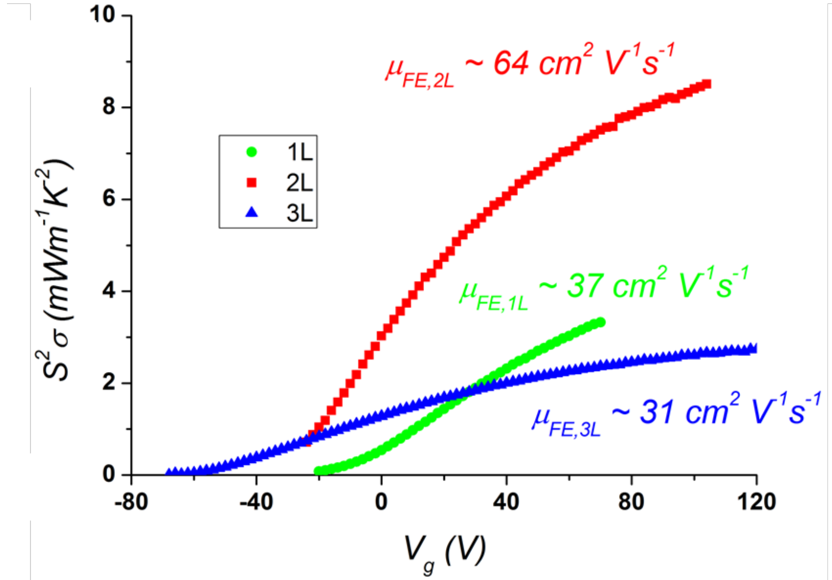

Figure 2-8: Powerfactor, $S^2\sigma$ as a function of gate voltage, V_g. The largest powerfactor is observed for the bilayer device, which also has the largest effective mobility of 64 $cm^2V^{-1}s^{-1}$.

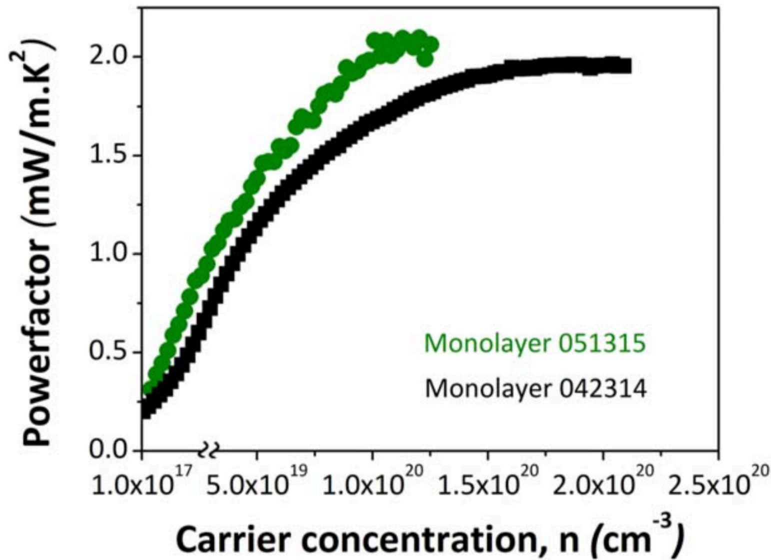

Figure 2-9: Saturation of powerfactor in MoS_2.

By comparing thermoelectric properties of atomic thin MoS_2 with traditional thermoelectric materials, we found MoS_2 shows recorded high powerfactor. The gate-modulated Seebeck coefficient of monolayer MoS_2 (shown as α in μV/K in Figure 2-10a) is plotted as a function of electrical conductivity (shown as lnσ in $\Omega^{-1}cm^{-1}$) in comparison to traditional thermoelectric materials. Evidently, α = m(b-lnσ), [66] with the slope m ≈

k_B/e. A larger value of the intercept, b, indicates a larger powerfactor ($\alpha^2\sigma$). The thermoelectric performance of monolayer MoS_2 is comparable with that of high-performance thermoelectric materials such as Bi_2Te_3 and PbTe. Similarly, the monolayer MoS2 matches Bi2Te3 in the $\alpha^2\sigma$-σ plot (Figure 2-10b), while the bilayer MoS2 has a higher powerfactor at the same conductivity, indicating superior thermoelectric performance. To understand the reason that bilayer MoS2 has recorded-high powerfactor and the limitation of powerfactor in two-dimensional materials, microscopic factors, such as effective mass and mobility are analyzed in details in the following sessions.

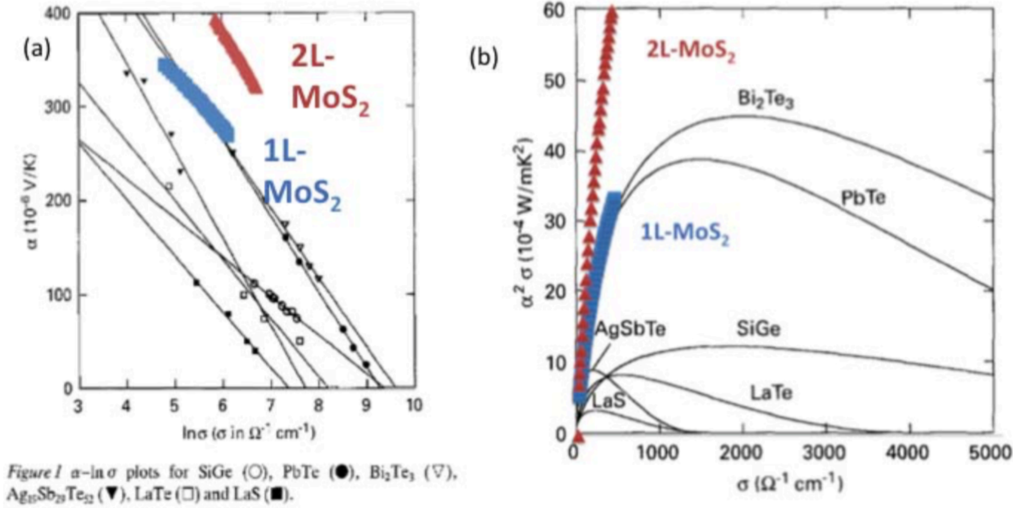

Figure 2-10: Comparison of thermoelectric performance of monolayer and bilayer MoS2 with traditional thermoelectric materials. (a) α-lnσ plot and $\alpha^2\sigma$-σ plot are adapted from Rowe *et. al* [66].The thermoelectric performance of monolayer is comparable with that of high-performance thermoelectric material Bi_2Te_3, while the bilayer indicates superior thermoelectric performance.

2.4 Analysis of DOS and band structure

The maximum power factor is 8.5 $mWm^{-1}K^{-2}$ at V_g = 104 V equivalent to a high electron concentration $n_{2D} \sim 1.06\times10^{13}$ cm^{-2}. For phonon-limited theoretical mobility in suspended monolayer MoS2, a power factor as large as 28 mW $m^{-1}K^{-2}$ is predicted at much less electron density level: $n_{2D} = 1\times10^{12}$ cm^{-2} [67]. It is important to explore factors, affecting the thermoelectric performance and then would direct the effort of engineering to further improve it.

And I firstly analyzed Seebeck coefficient microscopically. The Seebeck coefficient from the linearized Boltzmann transport equation (BTE) under the relaxation time approximation, given by the following

$$S = \frac{1}{qT} \frac{\int_{E_c}^{\infty} \frac{d\, f_{FD}}{dE} D_{2D}(E) * (E - E_F) * \tau(E) dE}{\int_{E_c}^{\infty} \frac{d\, f_{FD}}{dE} D_{2D}(E) * \tau(E) dE} \qquad (2.5)$$

Here, f_{FD} is the Fermi Dirac distribution, $D_{2D}(E)$ is the 2D DOS, E_F is the Fermi level with respect to the CBM at Ec, q is the electron charge, and $\tau(E)=\tau_0 E^r$ is the energy-dependent relaxation time, where r is the scattering exponent and depends on the dominant scattering mechanism. Essentially $\frac{d\, f_{FD}}{dE} D_{2D}(E) * (E - E_F)$ represents the imbalanced chemical potential generated by temperature gradient and $\tau(E)$ refers to the process of scattering to rebalance chemical potential within the material. From the equation above, DOS and scattering process play very important roles in Seebeck coefficient and those I will mainly discuss below.

In order to obtain the DOS used in the above equation, first principles calculations of the quasiparticle (QP) band structure of suspended monolayer and bilayer MoS_2 were conducted within the GW approximation (see in Figure 2-11). The CBM was found to be at the K and K' points in the Brillouin zone for monolayer MoS_2 and along the six-fold degenerate Λ high-symmetry line (Λ valley) for bilayer MoS_2, in good agreement with previous calculations [60,68,69]. The computed DOS of pristine monolayer and bilayer MoS_2 at the GW level shows that due to the larger band effective mass and higher degeneracy in the Λ valley, the DOS of bilayer MoS_2 at the CBM is ~4 times larger than the DOS of monolayer MoS_2. Therefore, higher DOS is one of the reasons to explain high power factor found in bilayers instead of monolayer.

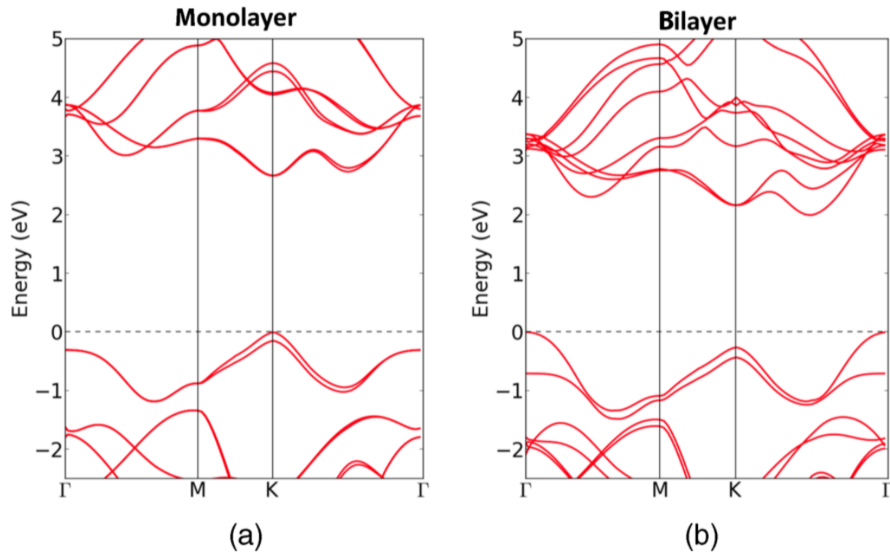

Figure 2-11: QP band structure of pristine monolayer and bilayer of MoS_2 calculated at GW level.

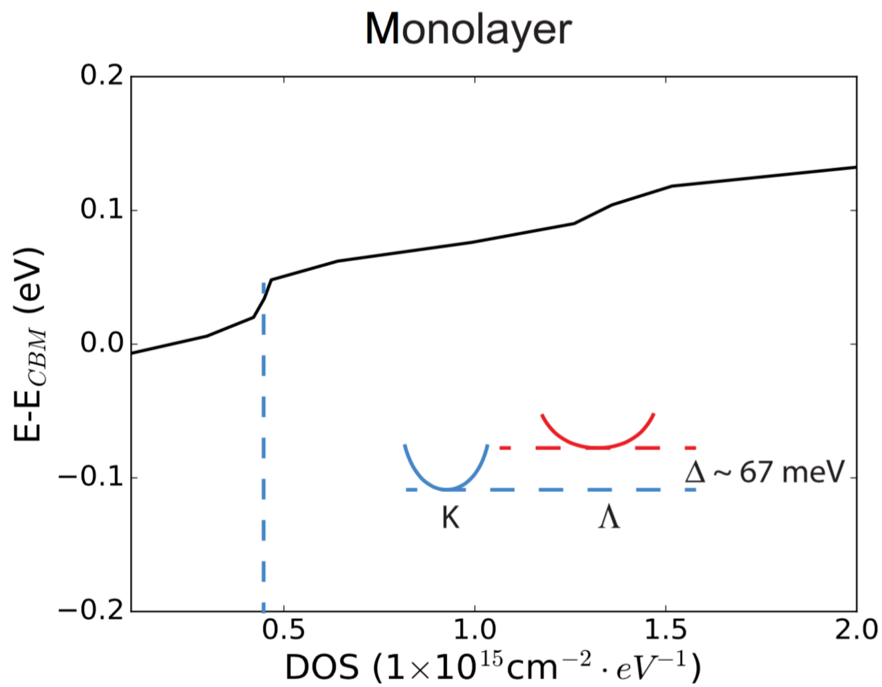

Figure 2-12: Calculated DOS of pristine monolayer MoS_2 as a function of the energy difference from the CBM in the K valley. The step function feature expected from 2D confinement can be seen clearly and in the inset, the relative positions of the K valley in monolayer MoS_2 show that thermoelectric transport only occurs through the K point in the monolayer since the energy difference is >~ $2k_BT$.

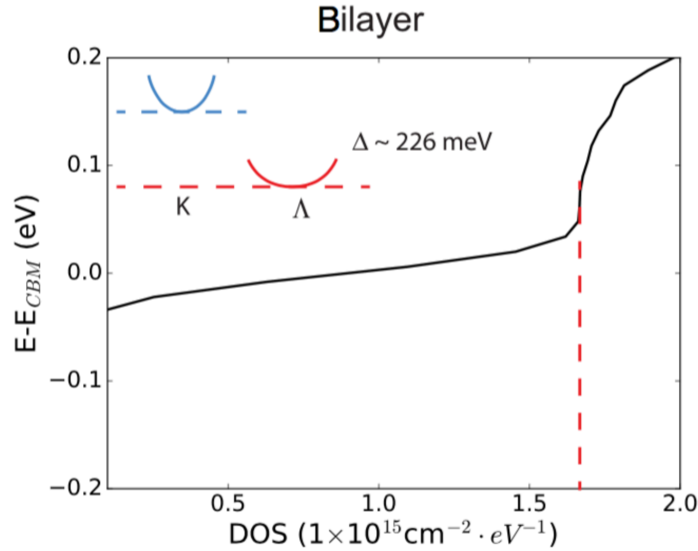

Figure 2-13: Calculated DOS of pristine bilayer MoS_2 as a function of the energy difference from the CBM in the K valley. The step function feature expected from 2D confinement can be seen clearly and in the inset, the relative positions of the K and Λ valleys in bilayer MoS2 show that thermoelectric transport only occurs through the Λ point in the bilayer since the energy difference is >~ $2k_BT$.

There is a possibility that besides CBM, there are more bands contributing to Seebeck effect due to thermal excitation of electrons in those additional bands. To exclude this, QP band structures of monolayer and bilayer MoS_2 are examined. Monolayer MoS_2 has a direct band gap at the K point. In addition to the CBM at K, there is another valley in the conduction band along the Λ high-symmetry line from Γ to K. We find that the bottom of this Λ valley is 67 meV higher in energy than the K point and thus unlikely to contribute to the Seebeck coefficient at room temperature, which provides thermal excitation at 23 meV. We also find that SO coupling splits the conduction band at K by 2 meV, so we expect both spin bands to contribute to the transport. For bilayer MoS_2, we ascertain that the CBM occurs along the Λ high-symmetry line and 226 meV smaller than second minimum point in conduction band. Hence, Λ valley mainly attributes to the Seebeck effect. The single valley contribution in both mono- and bilayers ascertains the validity of previous DOS analysis.

2.5 Scattering mechanism in MoS_2

Scattering process, revealed as $\tau(E)$ in equation 2.5 and it is energy-dependent relaxation time, defined as [70]

$$\tau(E)=\tau_0 E^r \qquad (2.6)$$

in which, $r = 0$ for acoustic phonon-limited scattering in 2D in the single parabolic band model. For charged impurity scattering, the scattering roughly has the energy dependence

r = 3/2 for a simple model for elastic scattering in which the bands are assumed to be parabolic and the impurity is screened with a Thomas-Fermi type screening in 2D [70].

Equation 2.7 relates Seebeck coefficient with Fermi level. Experimentally we cannot get the Fermi level directly. We did a derivation below to obtain equation of Seebeck coefficient as a function of doping level. Given that doping due to the back gate pushes the 2D MoS_2 channels into the degenerate limit,

$$n = \int_{E_c}^{\infty} D_{2D}(E) f_{FD}(E) dE \qquad (2.7)$$

where $D_{2D}(E) = \frac{g_v g_s m^*}{2\pi\hbar^2}$ are the 2D DOSs ascertained earlier. Here, g_V and g_S are the valley and spin degeneracies, respectively, and m^* is the band effective mass obtained from the band structure. $f_{FD}(E) = \frac{1}{e^{(E-E_f)/k_B T}+1}$ is the Fermi-Dirac distribution. Let $\varepsilon = (E - E_c)/k_B T$ and $\eta = (E_F - E_c)/k_B T$. Then the equation 2.7 above gives $n_{2D} = N_{c,2D} \int_0^\infty f_{FD}(\varepsilon) d\varepsilon$, where $N_{c,2D} = D_{2D} * k_B T$ is the effective DOS in two dimensions. Here, $\int_0^\infty f_{FD}(\varepsilon) d\varepsilon = F_0(\eta)$ is the zeroth order Fermi intergral, which can be evaluated analytically as $F_0(\eta) = \ln(1 + e^\eta)$. Therefore, we get the expression $(E_F - E_c) = k_B T(e^{\frac{n}{N_c}} - 1)$, which connect doping density n with Fermi level.

Calculating the Seebeck coefficient as a function of the carrier concentration, n, elucidates the dominant scattering mechanism of electrons in the 2D MoS2 channels given by equation 2.5. Using the energy-independent DOS D_{2D} and accounting for the energy-dependent scattering rate, Equation 2.5 can be written as follows:

$$S = -\frac{k_B}{q}\left[\eta - \frac{(r+2)\int_0^\infty f_{FD}\varepsilon^{r+1} d\varepsilon}{(r+1)\int_0^\infty f_{FD}\varepsilon^{r} d\varepsilon}\right] \qquad (2.8)$$

We calculate the Seebeck cofficient for both monolayer and bilayer MoS2 as a function of the carrier concentration and compare the calculated Seebeck coefficient to experimental values for four devices [see in Figure 2-14 and Figure 2-15, respectively]. Numerical integration was performed using the function fermi.m in Matlab [71] [46]. Here, we see that the Seebeck coefficient, as calculated from equation 2.8, fits the experimental data quite well when r = 0, which strongly suggests that the scattering is dominated by electron-phonon scattering.

Given phonons contributing to scattering barely comes from the lattice of flakes, the scattering rate in both the K and Λ valleys is constant, with a total scattering rate of roughly 1×10^{13} s^{-1} over all phonon modes from first principles [72,73]. With this

scattering rate, the phonon-limit mobility is ~410 $cm^2V^{-1}s^{-1}$ [74], which is one order higher than what we observed in our device. And this strongly indicts external source of phonon that mainly contributes to scattering in 2D materials. We suspect it comes from substrate's lattice oscillation.

Summarizing last two sessions, by carefully analyze the 2D DOS in both mono- and bilayer MoS_2, we conclude that given identical carrier concentrations, the magnitude of the Seebeck coefficient for the bilayer is larger than that for the monolayer as a consequence of the larger DOS at the conduction band edge, which stems from both a heavier effective mass and a higher valley degeneracy of the CBM at the high-symmetry valley. Carrier density dependent Seebeck coefficient manifests the scattering mechanism in electron transport is electron-phonon scattering.

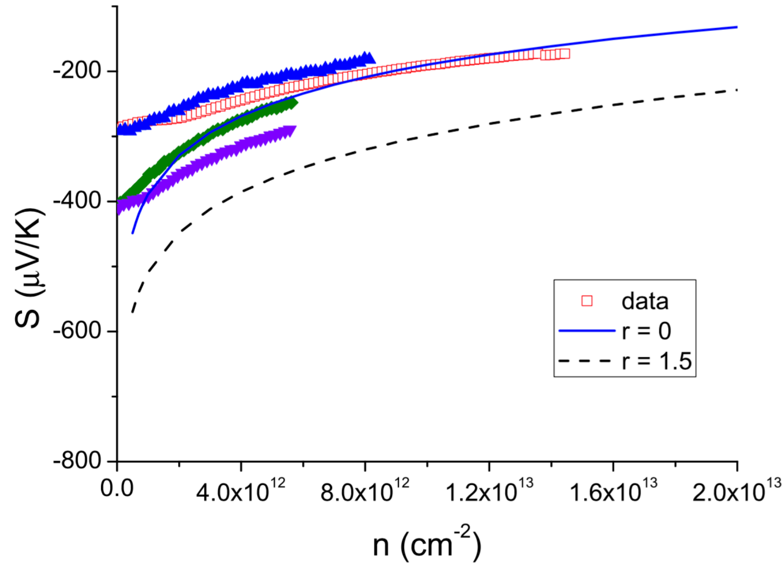

Figure 2-14: Phonon scattering mechanism in monolayer revealed through Seebeck coefficient. Monolayer experimental data (open symbols) compared with the estimated Seebeck coefficient from Eq. (2.5) for r = 0, consistent with phonon-limited scattering in 2D (solid lines) and r = 1.5 for reference (dashed lines). The data fit the r = 0 phonon-limited scattering case well.

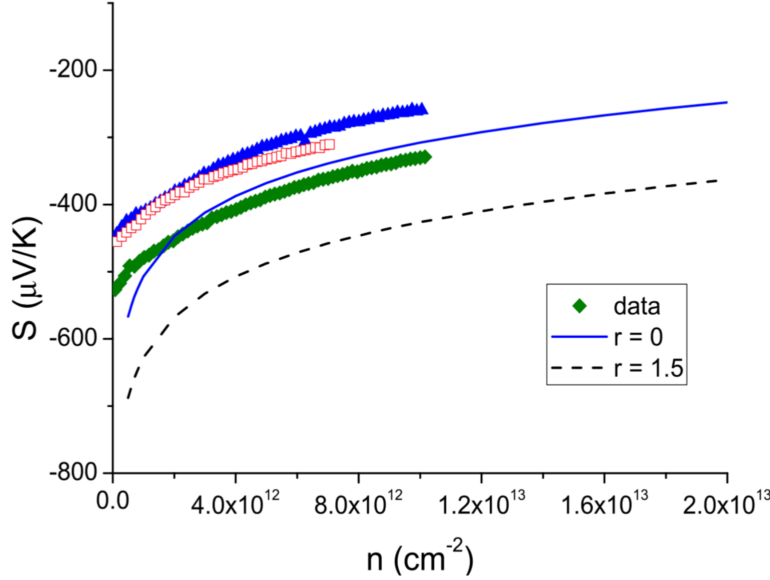

Figure 2-15: Phonon scattering mechanism in bilayer revealed through Seebeck coefficient. Bilayer experimental data (open symbols) compared with the estimated Seebeck coefficient from Eq. (2.5) for r = 0, consistent with phonon- limited scattering in 2D (solid lines) and r = 1.5 for reference (dashed lines). The data fit the r = 0 phonon-limited scattering case well.

2.6 Electrical properties of MoS_2

Second factor that affects power factor is electrical conductivity, which is determined by $\sigma = en\mu$, in which, e and μ are charge and mobility of electrons, respectively. And n is electron density, which is externally controlled through back gate. μ is intrinsic property of materials. The mobility of each MoS_2 is determined following standard procedure using field-effect transistor with a fixed drain-source voltage, V_{ds}=10 mV. Here, the drain-source current, Ids ∝ Vg and the mobility is given by: $\mu = \frac{dI_{ds}}{dV_g}\frac{L}{W}\frac{1}{V_g}\frac{1}{C_{ox}}$, where L and W are the MoS2 channel length and width respectively, $C_{ox} = \frac{\varepsilon_0 \varepsilon_r}{t_{ox}}$ is the oxide capacitance, where $\varepsilon_r = 3.9$ is the relative permittivity of SiO_2, $\varepsilon_0 = 8.85 \times 10^{-12}$ F/m is the permittivity of free space and t_{ox} = 275 nm is the thickness of the thermally grown oxide. This results in an estimated field mobility of 37 $cm^2V^{-1}s^{-1}$ for the monolayer, 64 $cm^2V^{-1}s^{-1}$ for the bilayer and 31 $cm^2V^{-1}s^{-1}$ for the trilayer, as shown in Figure 2-16. Since the exfoliated MoS_2 are n-type semiconductors, the devices turn on at negative gate voltages; the turn-on voltage is −20 V for the monolayer, −38 V for the bilayer and −64 V for the trilayer. Here we only report the two-probe nobilities for all devices.

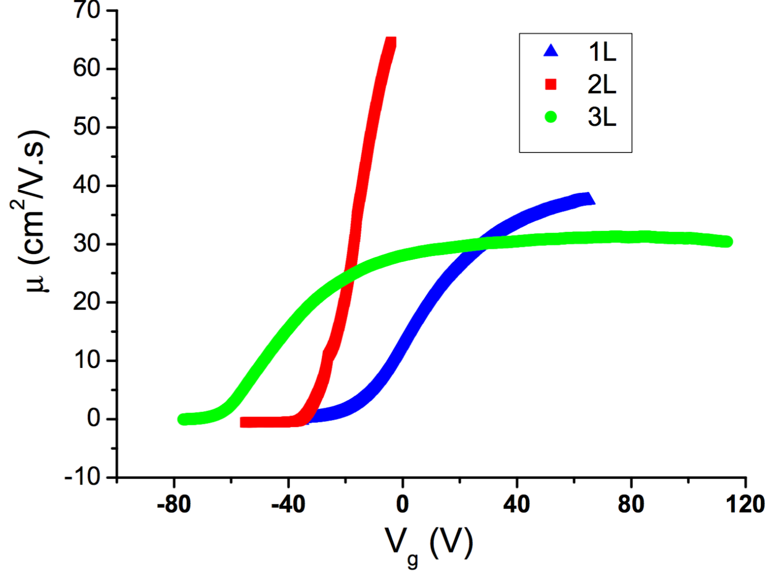

Figure 2-16: The measured field-effect mobilities of monolayer, bi- layer, and trilayer samples as a function of back gate voltage Vg. The measured mobility is 37 $cm^2V^{-1}s^{-1}$ for the monolayer, 64 $cm^2V^{-1}s^{-1}$ for the bilayer, and 31 $cm^2V^{-1}s^{-1}$ for the trilayer.

The bilayer sample shows largest mobility, as well as high electrical conductivity. Mobility of electron is inversely proportional to effective mass of conduction band edge. We determine that in monolayer, the effective mass of the lower band (which we refer to as spin up) is 0.45 m_0 and the effective mass of the upper band (which we refer to as spin down) is 0.59 m_0, where m_0 is the free electron mass. For bilayer MoS_2, we ascertain that the CBM occurs along the high-symmetry line. This valley is anisotropic, and its average effective mass is 0.68 m_0. Calculated effective masses, SO (Spin orbital coupling) splitting of the conduction band, and ordering of the conduction band valleys are summarized in Table 2-1. The effective mass indicates monolayer is supposed to have a higher mobility compared to bilayer due to its smaller effective mass, opposite to our experimental observation.

	n (cm^{-2})	$E_K - E_\Lambda$(eV)	$E_{K,c\downarrow} - E_{K,c\uparrow}$(eV)	$m_{\mathbf{K}\uparrow}(m_0)$	$m_{\mathbf{K}\downarrow}(m_0)$	$m_{\Lambda\uparrow}(m_0)$	$m_{\Lambda\downarrow}(m_0)$
Monolayer	0	−0.067	0.003	0.45	0.59	0.87	0.73
Monolayer	1×10^{13}	−0.668	0.003	0.45	0.53	1.18	1.02
Bilayer	0	−0.226	0.000	0.67	0.67	0.68	0.68

Table 2-1: summary of properties of band structure. Comparison of (1) the difference between the CBM at K and that along the high-symmetry line ($E_K - E_\Lambda$), (2) SO splitting of the conduction band at K, and (3) effective masses for spin-up (↑) and spin-down (↓) states in the K and Λ valleys in units of the free electron mass (m_0) for monolayer and bilayer MoS_2 with different doping levels (n).

We further exclude the impact of topography on mobility. We notice that the

formation of ripples in two-dimensional graphene [73–75] and MoS_2 [78–80] has been discussed broadly in literature. These 2D crystals form ripples in order to stabilize their structure. However, bilayer MoS2 is shown to be much flatter than monolayer MoS2 as well as bilayer graphene [78]. Thus the likelihood of ripples affecting on mobility and electron transport is minimal in bilayer devices. To avoid the effect, in our procedure of exfoliating samples, we rarely notice ripples, usually observable with high resolution SEM as evidenced by images in Figure 2-17 below. Occasionally, the samples fold over themselves (black arrows), but this is clearly visible either with an optical microscope or under a Scanning Electron Microscope (SEM) and we discard such samples and do not use them for fabricating our thermoelectric devices. Similarly we discard those samples with small ripples (red arrows) or cracks (green arrows) and/or multilayer overlap (blue arrow). Figure 2-18 shows representative SEM samples that have clean surfaces without ripples/cracks or folds, which are typical of the samples that we use for our thermoelectric devices.

With the effort to minimize external scattering from non-uniformity of flakes, we suspect that monolayer, which has half thickness of bilayer, suffers more from screening and scattering from the underlying dielectric substrate. It results that intrinsic mobility of monolayer is hindered. Therefore, electrical and phonon decoupling of monolayer MoS2 with substrate would increase the electrical performance greatly.

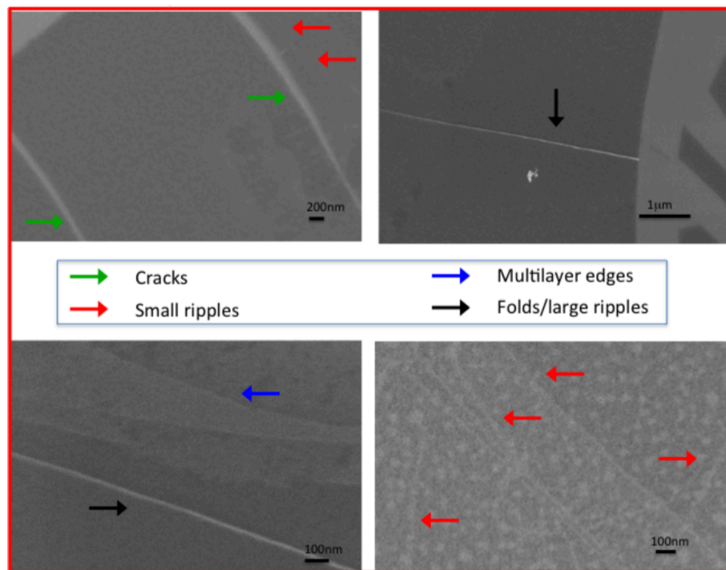

Figure 2-17: High Resolution Scanning Electron Micrographs (HR-SEM images) of 'defective' samples. We found many flakes are with visible folds, cracks, large/small ripples, and multilayer boundaries. We classify such samples as 'defective' during Electron Beam Lithography (EBL) patterning and do not use them for our measurements.

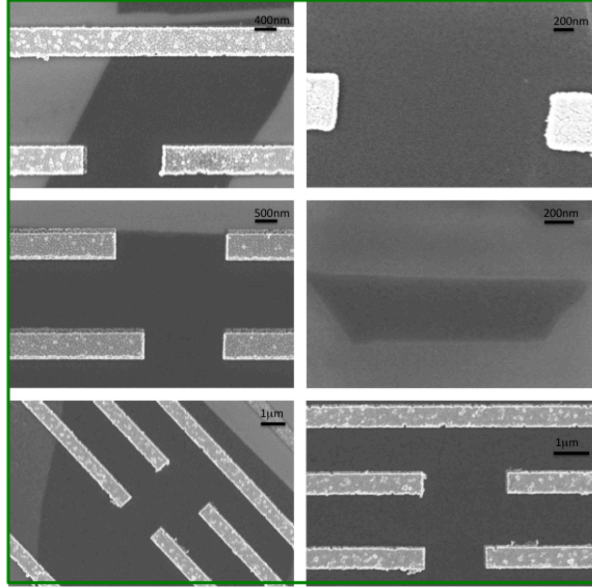

Figure 2-18: HR-SEM images of representative clean samples. These devices are with very low roughness, and showing no evidence of any 'defects' including ripples. The bright lines are electrodes formed after metal deposition.

2.7 Mott variable range hopping in MoS_2

Furthermore, a detailed study of transport behavior on monolayer MoS_2 was conducted and helps to understand the transport mechanism at 2D limits. At high temperatures and high electron concentrations, when the Fermi level is pushed close to the conduction band edge, monolayer MoS_2 undergoes an insulator-to-metal transition [81–83]. This metallike regime for conducting MoS_2 is determined by analyzing the conductivity as a function of temperature for different electron concentrations (gate voltages): we study the temperature-dependent electrical conductivity from 1.0×10^{11} to 5.1×10^{12} cm^{-2} for a monolayer MoS_2 sample, as plotted in Figure 2-19. The insulator-to-metal transition temperature T_{IMT} is defined as the temperature at which the measured conductivity changes from increasing with temperature to a metal-like decrease with temperature. This is corroborated from the mobility as a function of temperature, which changes its slope from 0.3 to ~1.9 at the insulator-to-metal transition temperature shown in Figure 2-20. We thus illustrate the electronic phase diagram of transport in MoS_2 in Figure 2-21, where T_{IMT} is plotted as a function of the carrier concentration. Since this phase diagram is linked to percolation, in the insulating phase, the conductivity follows a relation in temperature given by $\sigma \propto e^{-(T_0/T)^{1/3}}$ in a 2D system, which fits a Mott variable range hopping (m-VRH) model [83–85], separate from the first-order transition described elsewhere [81,86] . In m-VRH model, electrons at the Fermi level below the mobility edge (at E_c) are localized, but are able to hop from one localized site to another due to the gradient field or interaction with phonons [87]. This model for electron transport is further verified in Figure 2-22, showing the measured Seebeck coefficient, which follows a monotonic increase with temperature as $S \propto T^{1/3}$, using Zyvagin's formula for the m-VRH model [88–90], with $S \rightarrow 0$ as $T \rightarrow 0$ (inset). Such m-VRH transport is in stark

contrast with the thermally activated transport mechanism in semiconductors [91,92], and indicates electron-phonon interaction is strong in this system.

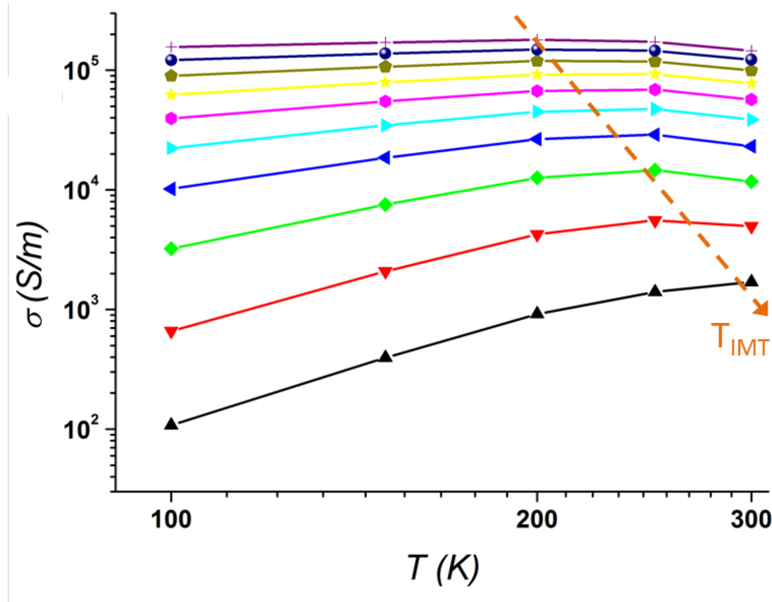

Figure 2-19: Temperature-dependent electrical conductivity at different carrider density. As the gate voltage $V_g \sim n$ increases, the insulator-to-metal transition temperature (T_{IMT}) shifts to lower temperatures.

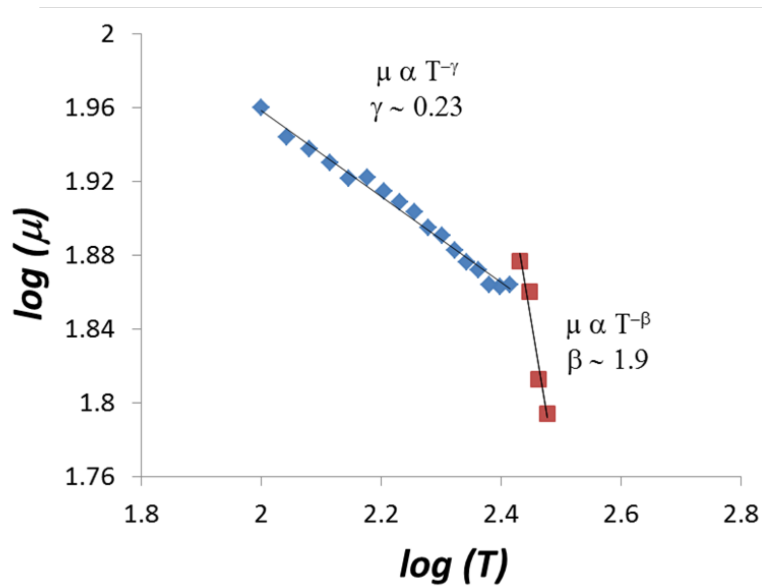

Figure 2-20: Temperature-dependent mobility of monolayer MoS_2. The mobility undergoes a rapid decrease with an exponent ~0.23 to ~1.9 crossing the metal-insulator-transition temperature (TIMT).

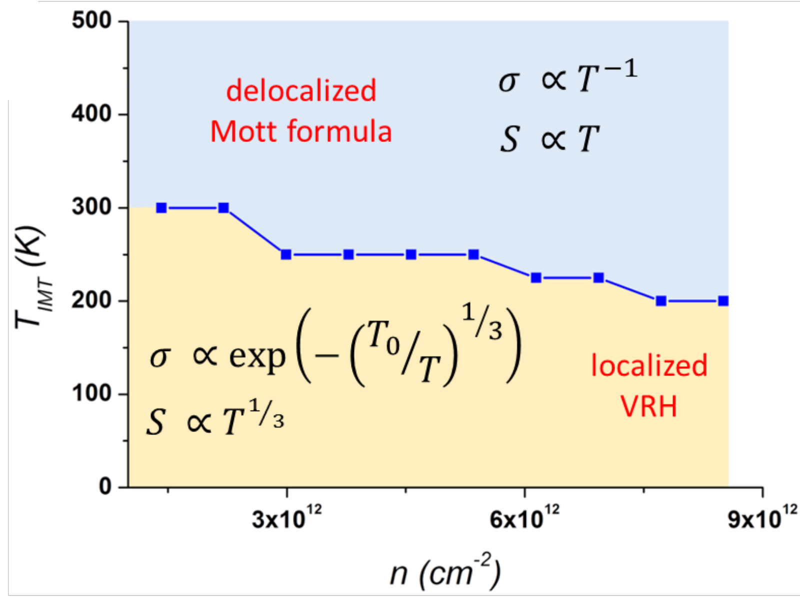

Figure 2-21: Phase diagram for thermoelectric transport as a function of temperature and electron concentration. For insulating phase, $T > T_{IMT}$, the Seebeck increases slowly, $S \propto T$ (Mott formula for extended states) while for conducting phase, $T > T_{IMT}$, $S \propto T^{1/3}$ (VRH for localized states).

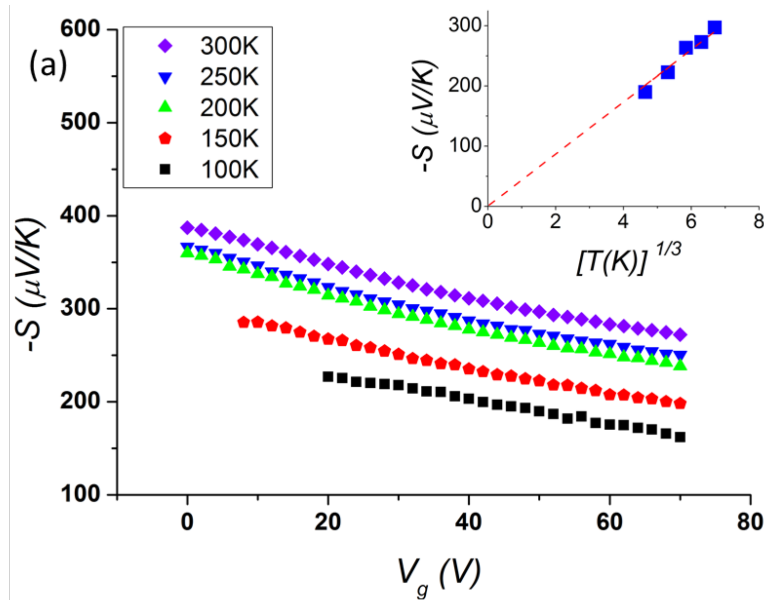

Figure 2-22: Experimental Seebeck Coefficient for 1L-MoS_2 as a function of temperature and applied back-gate voltage. The magnitude of Seebeck decreases (increases) with backgate (temperature). In the inset we show that the measured

Seebeck at a fixed carrier concentration $n = C_{ox}/e \cdot (V_g - V_T)$, which shows a function of $T^{1/3}$, indicating Variable-Range Hopping dominates transport.

And the distance of hopping between localized states can be extracted as well. In 2D, Mott VRH gives $T_0 = (13.8/k_B D(E_F)\xi^2)$ [93,94], where T_0 is VRH correlation energy scale, $D(E_F)$ is the density of states due to the localized states at the Fermi level, E_F and ξ is the localization length. In two dimension, the conductivity in the insulating phase follows $\sigma(T) = \sigma_0 \exp[-(T_0/T)^{1/3}]$ and gives T_0 for different doping level from figure Figure 2-23. If we assume the density of localized states is equal to that observed in [82], $D(E_F) = D_{it} \sim 8\text{x}10^{13}$ $eV^{-1}cm^{-2}$, we can extract the localization length, ξ as a function of T_0 as shown in Figure 2-24 from our experiment on a monolayer MoS2 sample saturating to a value of ξ~2.7nm when transport is fully metallic. This value of localization length agrees well with other studies in 2D TMDCs [82,93–95]. Considering a defect density of n_t ~$1\text{x}10^{13}$ cm^{-2} [95] the average defect distance is a~3 nm: thus when $\xi \geq a$, the states becomes delocalized (for n $\geqslant$ $2\text{x}10^{12}$ cm^{-2}) resulting in metal-like transport which corroborates our observation in Figure 2-21.

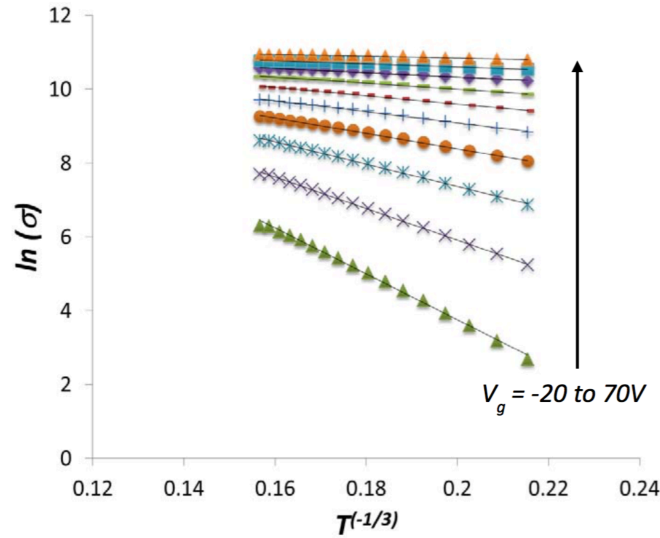

Figure 2-23: Temperature-dependent conductance of monolayer MoS_2 in insulating phase with different gate voltages. The conductance follows the relation of $\sigma(T) = \sigma_0 \exp[-(T_0/T)^{1/3}]$ in two dimensions, indicating the Mott Variable Range Hopping (M-VRH) mechanism.

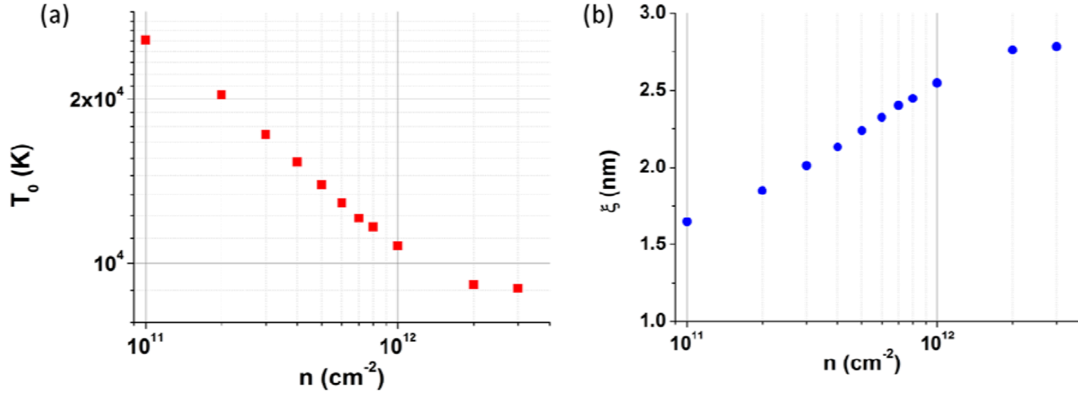

Figure 2-24: Variable-Range Hopping (VRH) correlation energy scale T_0 and The localization length ξ, plotted as a function of carrier concentration. The value of T_0 agrees well with literature [77,79].

2.8 Exclude the impact of Joule heating on temperature distribution

Both Seebeck coefficient and electrical conductivity are measured through electrical method. There is possibility that electrical current, as an electrical probe, could add external temperature source caused by joule heating. Since the Seebeck measurements are performed under open circuit conditions such current-induced effects will be zero while measuring the thermopower. When measuring electrical conductivity, there is a current passing through the whole flake from one end to another, causing Joule heating. However, the Joule heating is significant only under high source-drain currents and voltages (typically Ids~150 μA/μm and Vds~1 V) based on the experiments on graphene [96,97]. While in our measurements, Ids<0.1 μA/μm and Vds<10 mV, which means that the effects of heating and thermoelectric voltage generation should be orders of magnitude smaller than those reported for graphene.

In order to verify experimentally that the measured electrical properties do not depend on the source- drain current, Ids, we performed an experiment where we measured the 2-probe electrical resistivity as a function of a series of atypically high Ids values (~500 times higher than values we typically use for electrical conductivity experiments: see Figure 2-25). The length of this device is 9 μm, thus the current densities are: 5.56 μA/μm (Ids=50 μA), 11.11 μA/μm (Ids=100 μA), 22.22 μA/μm (Ids=200 μA), and 55.56 μA/μm (Ids=500 μA) respectively. The electrical resistivity does not depend upon the magnitude of the current and indicates that joule-heating, current-crowding or thermoelectric effects should be negligible even at such high current densities for the measured electrical conductivity.

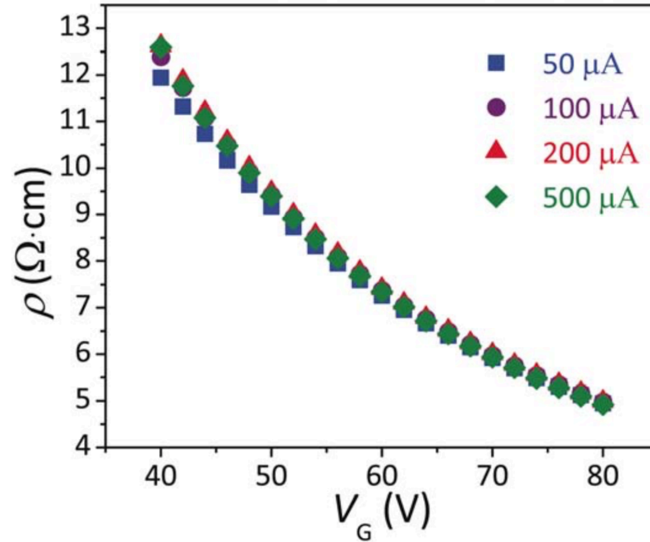

Figure 2-25: Resistivity dependence of source-drain current. For different values of the drain-source current, I_{ds}, the measured resistivity is identical, especially at high gate voltages.

We have performed an additional experiment to monitor the temperature rise in the MoS_2 (by measuring the Raman shift of the MoS_2 E_{2g} peak) while driving an increasing electrically supplied power through the device. The summary of this data is shown in Figure 2-26. The temperature calibration was performed on the same device in a home-built Raman cryostat where the stage temperature was monitored while the Raman-active E_{2g} peak location was measured. By calibrating the peak-shift as a function of temperature, we can ascertain the local temperature of the MoS_2 device given by ΔT_{MoS2} [98,99]. Since $\Delta T_{MoS2} \propto (I_{sd} * V_{sd})$, we see that the temperature rise in MoS2 only begins at ~2 mW (corresponding to an applied current of ~250 μA). The device length is 5 μm giving a current density of ~50 μA/μm which is ~500 times higher than the typical values used for measurement of two-probe electrical resistivity (typically <0.1μA/μm) that we used in all experiments. This is also consistent with the high current density experiments performed above. Therefore, we could exclude current joule heating and thermoelectric effects here and power factors obtained from experiments are reliable.

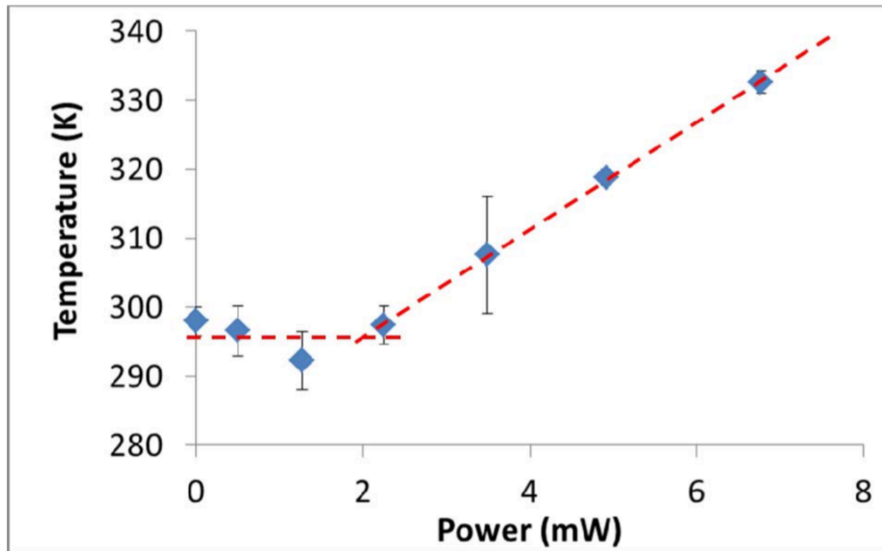

Figure 2-26: Temperature measurement of MoS_2 device using Raman spectroscopy.The temperature rise in MoS_2 only begins at ~2 mW (corresponding to an applied current of ~250 μA).

Material	μ (cm^2/V·s)	carrier concen-tration (cm^{-3})	ρ (mΩ-cm)	|S| (μV/K)	PF (mW/ m·K^2)	m^*/m_0
Bi_2Te_3 [Shigetomi, Mori @1956] [31]	p ~ 280 n~200	~1×10^{18} ~1.4×10^{19}	~1.3 ~1.6	~180 ~150	~2.5 ~1.4	~1.26 ~1.07
Bi_2Te_3 [Harman, Paris, Miller, Goering @1957] [32]	p ~ 540 n ~ 400	5×10^{18} 8×10^{18}	~ 2 ~ 2	~150-200 (both n- and p-type)	~2.0	0.46 0.32
Bi_2Te_3 [Satterwaithe, Ure @ 1957] [33]	p ~ 410 (ZR) p ~ 430 (D4) p~ 680 (D7) n ~ 330 (D5) n ~ 440 (D13)	2×10^{19} 3×10^{18} 4×10^{18} 9×10^{17} 3×10^{17}	0.76 4.84 2.3 21.04 47.34	< 200 (both n- and p-type)	5.2 0.8 1.7 - -	-
BiSbTe crystal [Caillat et. al.@1992] [34]	**n ~ 150 (S1)** n ~ 200 (S2)	**7×10^{19}** 3×10^{19}	**0.6** 1	**~180** ~200	5.4 4.0	~0.7
BiSbTe crystal [LaHalle-Gravier, Lenoir, Scherrer &	**n ~ 90** **n ~ 50**	**4×10^{19}** **1.6×10^{20}**	**1.6** **0.8**	**250** **175**	3.9 3.8	-

Scherrer @1998] [35]						
2L-MoS_2 [this work]	*n* ~ 64	8×10^{19}	1.36	340	8.5	~8.1
1L-MoS_2 [this work]	*n* ~ 37	1.2×10^{20}	2.65	283	3.0	~2.1

Table 2-2: the thermoelectric properties of traditional thermoelectric materials in comparison with our MoS2 devices.

2.9 Conclusion

The table above summarizes the thermoelectric properties of traditional thermoelectric materials in comparison with two-dimensional material MoS_2. The mobilities of commercial thermoelectric materials are higher at lower doping concentrations. Our equivalent 3D bulk carrier concentration (based on the thickness of ~1.3 nm for bilayer) is higher ~1×20 cm^{-3} and the mobilities are comparable to values for Bi_2Te_3 and BiSbTe, and as expected mobility drops with an increase in carrier concentration. At these high electron densities, we observe a larger Seebeck value due to the high valley degeneracy and large effective mass, which explains why our values of powerfactor for 2D MoS_2 are about the same or larger than traditional thermoelectric materials, making 2D TMDCs promising candidates for planar thermoelectric applications. The enhanced power factor in the metallic regime is attributed to the sizable conductivity in the highly doped crystals and a large Seebeck coefficient stemming from high valley degeneracies and effective masses, especially in the case of the bilayer, where a large effective mass at the CBM in the valley is coupled with a sixfold valley degeneracy. We measure thermoelectric transport in the highly doped regime allowing us to access the 2D DOS in TMDCs. Our device configuration allows us to tune the carrier concentration of 2D MoS2, which is difficult in bulk materials, hence providing important insights into thermoelectric transport in these layered materials. The high power factor in layered TMDCs provides an exciting avenue to enhance thermoelectric efficiencies and galvanize the growth of thermoelectric devices in the near future.

3 Structural phase transition controlled by large population of quasi-particles

3.1 Structural phase transition in two-dimensional materials

Structural phase transition refers to the process that crystal lattice reforms to another structure, involving atomic movements. Even though materials are composed of the same chemicals, their physical properties are distinct due the difference of crystal structure. For example, carbon atoms form graphite and diamond at particular conditions. Almost every aspect of them differs, such as mechanical, electrical, thermal properties et al.

The crystal form commonly studied among TMDs is the most stable 2H phase (left panel in Figure 3-1), in which hexagonally arranged transition metal atoms are sandwiched between two chalcogen atom layers [52]. When thinned down, monolayer 2H TMDs become direct bandgap semiconductors and break inversion symmetry, creating inequivalent K and K' valleys [100,101]. This valley degree of freedom, together with the strong excitonic effect in low dimension, makes this phase a unique platform for 2D valleytronics and optoelectronics [102–104]. Intriguingly, experimental studies report another crystal structure, namely 1T' phase, where chalcogen atoms form octahedral coordination around transition metal atoms with a lattice distortion along y axis [105] (right panel in Figure 3-1). Contrary to the semiconducting 2H phase, the semimetallic or metallic 1T' monolayer TMDs, retain inversion symmetry and are predicted to display non-trivial topological states [106,107]. Dynamic control of transitions between the 2H and 1T' phases can reveal the competition, coexistence and cooperation of different crystal structures and interplay among distinct physical properties [108]. It also leads to broad device applications such as memory, reconfigurable circuits and topological transistors at atomically thin limit [106,109,110].

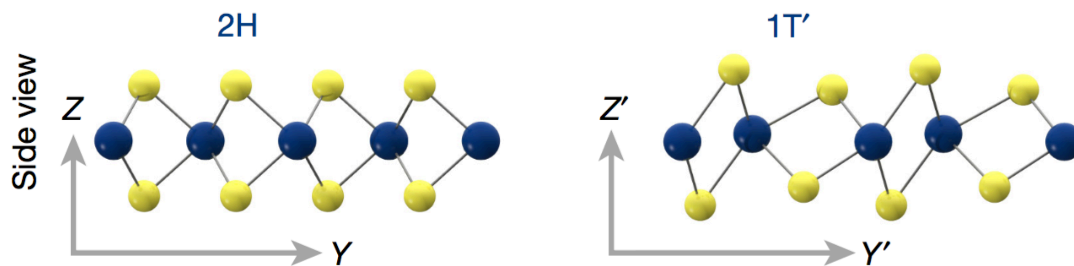

Figure 3-1: Crystal structures of the 2H and 1T′ phases of monolayer TMDs. Blue spheres, metal atoms (molybdenum or tungsten); yellow spheres, chalcogens (selenium, sulfur or tellurium). In our experiment, the coloured spheres represent molybdenum and tellurium atoms.

So far, the 2H to 1T' phase change in TMDs such as $MoTe_2$ is experimentally reported through thermal synthesis at 500° C [111], irreversible growth by element

substitution [112] and laser irradiation [113]. However, these phase transitions were only found in few layers or bulk and not yet realized in monolayers. Reaching 2D limit is important to explore phase ordering competition with largely enhanced electron-phonon and electron-electron interactions, which are the core for many-body phenomena like high-Tc superconductivity [114]. It also opens the access to unique properties in monolayer materials such as valley degree of freedom [100], Ising pairing [115] and topological transport [107].

In comparison to above methods, electrostatic gating control could be a new approach to achieve structural control. Essentially, the excessive electrons injected into a crystal of 2H phase under an electrostatic bias, occupy the lowest available energy states in the conduction band, which are hundreds of meV higher than that in 1T' phase, shown in Figure 3-2. Therefore, at high doping level, the extra electrons are expected to carry enough energy to lift the total energy of 2H phase higher than that of 1T', switching the ground state from 2H to 1T' phase and inducing structural phase transition [116]. And this new method is expected to be dynamic, reversible and free of impurity and very important for potential applications such as switching memory and reconfigurable devices. Based on the theoretical calculation, the requirement of doping level to drive such transition is up to 10^{14} cm^{-2}, which is only achievable in two-dimensional materials. Therefore, it is promising to demonstrate this method as well as achieve dynamic control between 2H and 1T' phases.

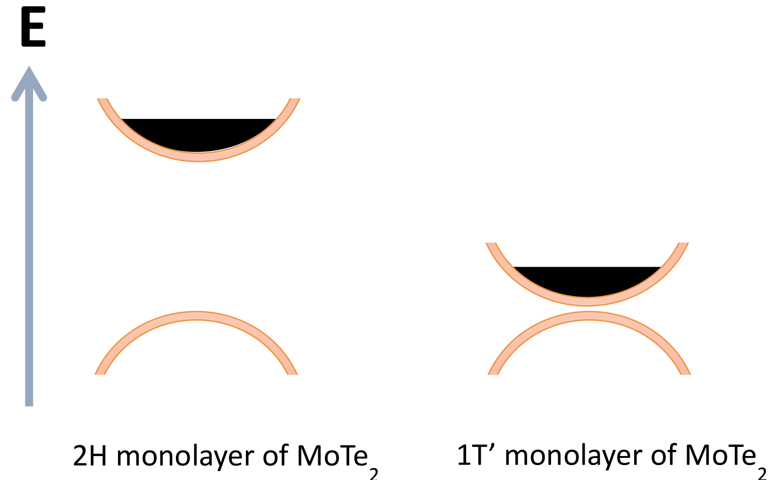

Figure 3-2: Mechanism of electrostatic doping driven phase transition

3.2 Electric-double-layer field-effect transistor

A salt can be melted down, by providing proper amount of heat to the system to overcome the lattice energy. Such a melted salts, called as ionic liquid, consist of ions and their combinations. Some salts, having a low melting point, are liquid form at room temperature, or at even lower range. Compared to aqueous, organic, gel or polymer electrolyte, ionic liquids have no solvents and can be exposed to moderate potential difference with chemical reaction. Therefore, they are nonvolatile and compatible with

most material systems. And ionic liquids have been employed to manifest outstanding performance in energy storages, Li-based batteries, electrochemical reactions et al [117–119].

Another vital application of it is 'super capacitance', which is significant to realize the structural change in two-dimensional materials. For a long time, native oxides of silicon have been used as core dielectric materials in field-effect transistors (FETs) to dope channel materials. And nowadays organic compounds, polymers, nano-composites, complex oxides, and/or low carrier density metals are considered to replace traditional silicon oxide and futher improve the performance of FETs. Especially, high capacitance of dielectric materials is required for achieving high doping level and larger on-off ratio. The accumulated charges Q in semiconductor can be expressed in a parallel-place capacitor and written as

$$Q = CV \tag{3.1}$$

where C and V are capacitance and applied voltage, respectively. The higher capacitance, lower voltage is required. And a parallel-place capacitor can be expressed in a simple way as

$$C = \frac{\varepsilon_0 \varepsilon_r A}{d} \tag{3.2}$$

where ε_0 and ε_r are the vacuum and relative permittivity. A is the area of the plates, and d is the distance between the two plates. Any dielectric material below 10 nm suffers from severe breaking down because of lattice imperfection. Therefore, the maximum capacitance for a solid gate is limited to be tens of nF/cm^2 and hence hinders the doping level going beyond $10^{13}/cm^2$. Surprisingly, if the dielectric material is replaced by ionic liquid, the measured capacitance is ~10 $\mu F/cm^{-2}$ and the relative permittivity is 1~10. The effective distance in the parallel capacitor model is 1Å~8.85Å, multiple orders smaller than the real thickness of ionic liquid, which is usually~mm.

The ultra small effective distance can be understood by Helmholtz model that a single layer of ions in solution absorbed on solid surface, together with charges in solid forms an electric double layer (EDL) (see in Figure 3-3). The distance between positive and negative charge layer is around the physical size of ionic molecules. And there are two EDLs in the FET. One is the semiconductor-liquid surface and another is metal-liquid one. And it indicates that the potential drop happens within the electric double layers instead of the bulky body of ionic liquid (see in Figure 3-4). Therefore, the ability of injecting carrier into channel material is independent of the volume of ionic liquid. This differs from traditional solid dielectric materials, where potential drops linearly through the bulk, preventing it thinning down.

3.3 Experimental design and device fabrication

With that, we employed ionic liquid as gate dielectric material to reach the doping level requirement to drive phase transition. We first designed and fabricated one FET on monolayer 2H $MoTe_2$. Monolayers of 2H-$MoTe_2$ were obtained by mechanically

exfoliating bulky single crystals onto a Si wafer covered with a 285 nm thick thermally grown SiO_2 layer. After identifying positions of monolayers, electrodes were patterned by standard electron-beam lithography and electrode metal of In (5 nm)/Au (100 nm) was deposited through thermal evaporation. A drop of ionic liquid was cast on the top of device, covering both monolayer flakes and metal pad for gating (Figure 3-5). The ionic liquid used in this study is N ,N -diethyl-N -(2-methoxyethyl)- N -methylammoniumbis-(trifluoromethylsulfonyl)-imide (DEME-TFSI). $DEME^+$s and $TFSI^-$s are cations and anions, respectively. From theoretical calculation, the requirement for density of electrons is half of that for holes. Therefore we apply positive voltage to make $DEME^+$s accumulating on the surface of 2H $MoTe_2$ monolayer and doping it with electrons. Figure 3-6 exhibits the EDL formation on top of monolayer $MoTe_2$ under positive bias.

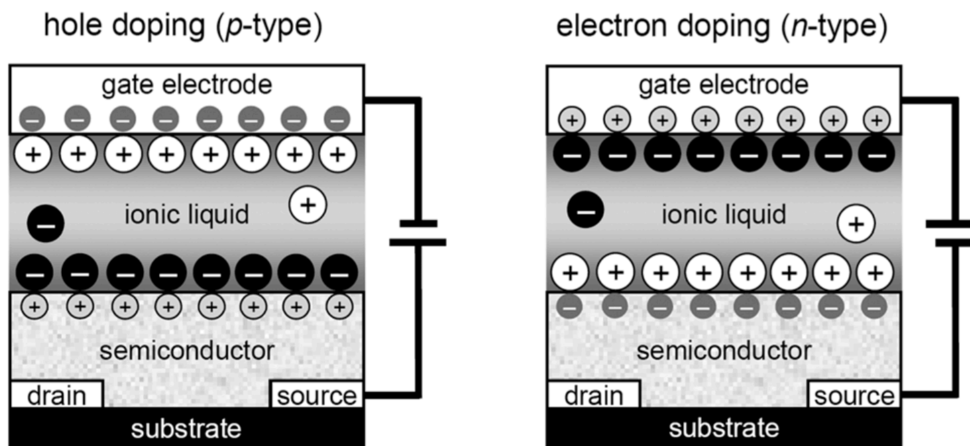

Figure 3-3: Schematis of the EDL-FETs. It shows hole (left) and electron (right) dopings. Reprinted permission from Royal Society of Chemistry.

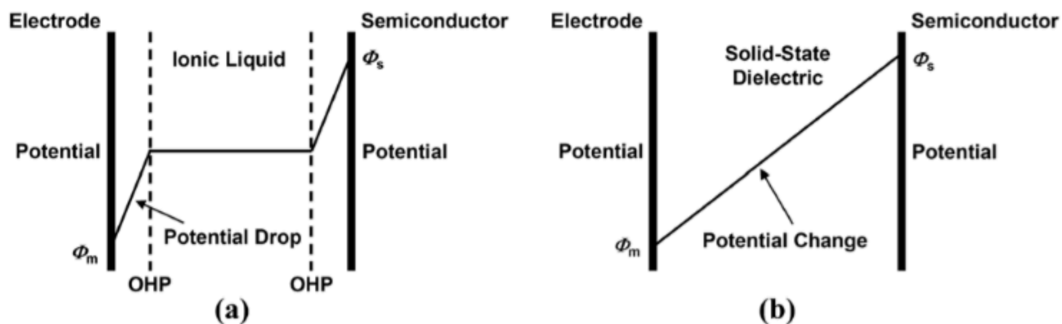

Figure 3-4: Potential changes in dielectric materials. They are sandwiched by an electrode and a semiconductor, for ionic liquids (a) and solid-state dielectrics (b). Reprinted permission from Royal Society of Chemistry.

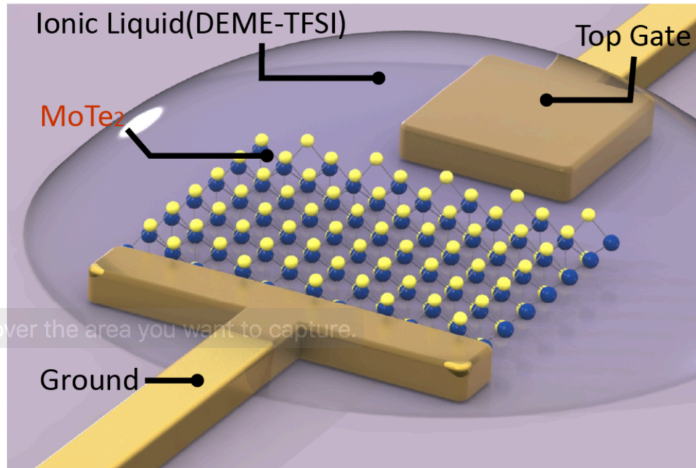

Figure 3-5: Configuration of monolayer $MoTe_2$ FET with ionic liquid gate. The monolayer $MoTe_2$ is anchored by a ground In/Au contact and an isolated In/Au pad nearby works as contact to control gate bias. Ionic liquid (DEME-TFSI) as dielectric gate can manipulate electron population in $MoTe_2$, resulting in structural transition between 2H and 1T' phases

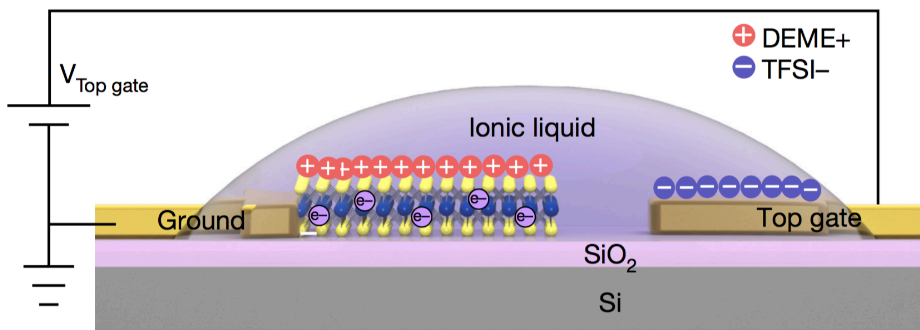

Figure 3-6: Cross section of FET with ionic liquid gate. This ionic liquid can manipulate the electron population in MoTe2, resulting in a structural transition between the 2H and 1T′ phases.

3.4 Demonstration of phase transition through electrostatic doping

Since the phonon vibration modes (Raman active modes) are distinct in different lattice configurations, we use Raman spectra to identify the structural status of monolayer $MoTe_2$. Firstly, Raman spectra of exfoliated monolayers from pristine 2H and 1T' bulky synthetic crystal were measured. Specifically, 632.8 nm laser excitation was chosen because it shows high Raman intensity for monolayer and could be used for layer identification. In Figure 3-7, Raman spectra for each phase are compared. Within the

measured spectra range, 2H monolayer exhibits two characteristic Raman modes: 171.5 cm^{-1} ($A_1^{'}$) and 236.0 cm^{-1} ($E^{'}$). In contrast, only one peak is shown in pristine monolayer 1T' flake: 166.8 cm^{-1} (A_g). Also, no Raman features from ionic liquid showed up among this studied range and make this system clear to study. To keep consistence, the measurements of Raman spectra and all other measurements mentioned in this chapter were kept at 220 K.

Based on Raman spectra, we identified the status of phase evolution of the monolayer $MoTe_2$ when injecting electrons through sweeping gate, shown in Figure 3-8. When top gate is zero biased, the initial exfoliated 2H monolayer $MoTe_2$ shows its two characteristic Raman peaks: 171.5 cm^{-1} (out of plane $A_1^{'}$ mode) and 236 cm^{-1} (in plane $E^{'}$ mode). Both peaks display simultaneous intensity drop and linewidth broadening after gate bias above 2.8 V, which is one signature of ongoing bond breaking and disappearance of 2H phase. Meanwhile, Raman spectra also exhibit a rising new peak at 167.5 cm^{-1}. By verifying these measured Raman spectra consistent with calculated and measured spectra of pristine monolayer 1T' $MoTe_2$, we confirmed this new peak corresponds to the characteristic A_g mode of 1T' phase. This evidence clearly points out the formation of 1T' phase under gate control.

Only one A_g mode of 1T' phase was used to reveal the emergence of new phase, even though another A_g (270 cm^{-1}) mode was observed in Raman spectroscopy of pristine 1T' monolayer $MoTe_2$ (Figure 3-9). But its intensity is 20 times smaller than the one around 170 cm^{-1}. Meanwhile, ionic liquid (DEME-TFSI) employed as top gate provides a strong Raman background around 270 cm^{-1} and hinders the visualization of A_g (270 cm^{-1}) mode. We carefully compared the spectra at 4V between monolayer $MoTe_2$ with ionic liquid on top (black line in Figure 3-9(b)) and bare ionic liquid nearby (red line). By deducting Raman background from ionic liquid, a small peak at 270 cm^{-1} was identified (blue curve) and reconfirms that the presence of 1T' phase. Since A_g (167 cm^{-1}) has a much stronger intensity and little influence from ionic liquid background, we mainly choose it as the main feature to study phase-change mechanism behind.

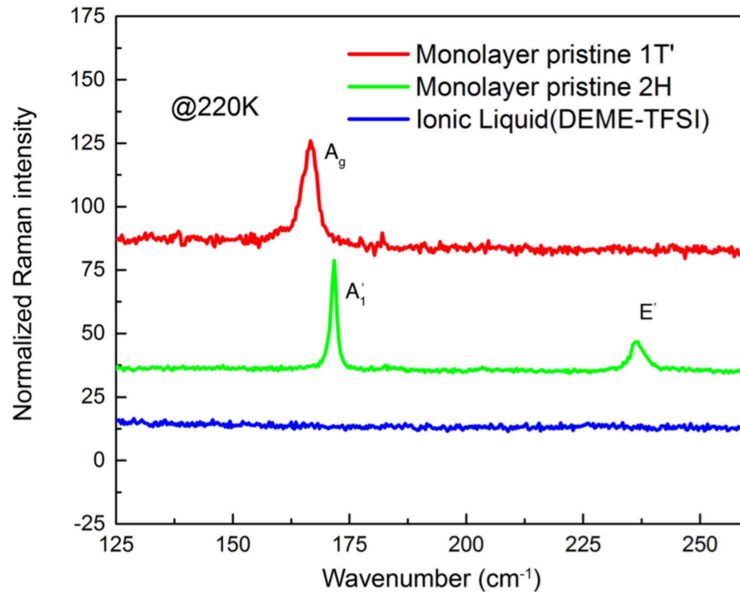

Figure 3-7: Raman features of pristine 2H-and 1T′-phase monolayer $MoTe_2$.Raman spectra for the 2H and 1T′ phases of monolayer $MoTe_2$ are plotted in green and red, respectively. The Raman modes at 171.5 cm^{-1} and 236 cm^{-1} are the A′ and E′ oscillation modes, belonging to the 2H phase. Excited by the same wavelength (632.8 nm), the 1T′ monolayer has just one dominant mode, at 166.8 cm^{-1}. The blue curve, from bare ionic liquid, shows no Raman modes and so acts as a clear and flat background in all Raman measurements.

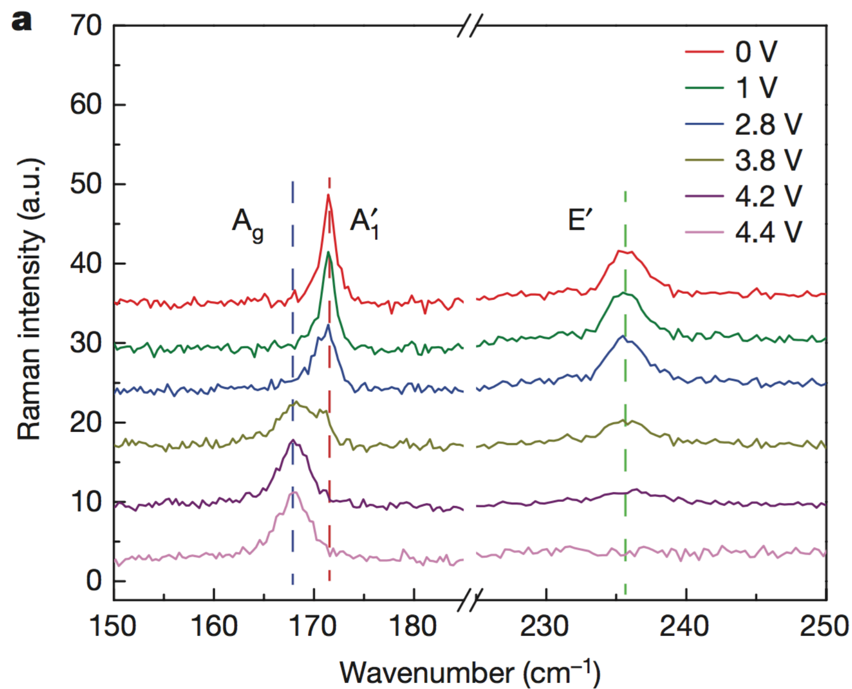

Figure 3-8: Representative Raman spectra before, during and after phase transition from 2H to 1T’ phase. When bias changes from 0V to 4.4V, the characteristic

Raman modes of 2H phase, A_1' and E' (red and green dashed line at 171.5 cm^{-1} and 236 cm^{-1}, respectively) gradually decreases accompanying with the growth of the A_g mode of 1T**'** phase (167.5 cm^{-1}, blue dashed line).

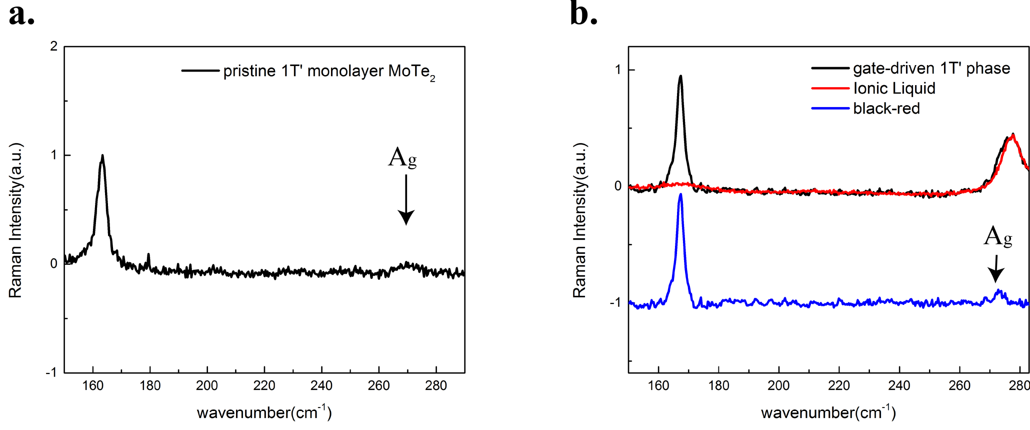

Figure 3-9: Ag mode observed in gate-driven 1T' phase. A large Raman background originating from ionic liquid emerges at 270 cm^{-1} (red in (b)), masking the A_g mode of 1T' phase. By deducting the Raman contribution of ionic liquid, a small peak at 270 cm^{-1} is visible (blue in b), which is consistent with the peak position observed in pristine 1T' monolayers (a).

And A_g mode in the gate-induced 1T' phase is 167.5 cm-1, which has 0.7cm^{-1} blue shift, compared to pristine monolayer 1T' phase. We suspect it comes from some mechanical constraints, originating from the process of structural change. At zero stress, the 2H phase and 1T′ phase of monolayer MoTe2 have different lattice constants. Therefore, the lattice constants would be expected to change when a transition from the 2H phase to the 1T′ phase occurs at zero stress. However, substrate friction could prevent the lattice constants from changing by fully or partially inhibiting sliding. Therefore, the lattice constants of the electrostatic-doping-induced 1T′ phase could be in between the pristine 1T′ phase lattice constants and the 2H phase lattice constants, depending on the magnitude of the substrate friction. To study this strain effect, the peak shift of the Ag mode of 1T′ phase monolayer MoTe2 was calculated by using different lattice constants (a, b), ranging from the pristine 1T′ phase lattice constants ($a_{T'}$, $b_{T'}$) to the 2H phase lattice constants (a_H, b_H), as follows:

$$\begin{cases} a = a^{T'} + x(a^H - a^{T'}) \\ b = b^{T'} + x(b^H - b^{T'}) \end{cases} \tag{3.3}$$

$$\begin{cases} x = 0: a = a^{T'} = 3.452\text{Å}, \quad b = b^{T'} = 6.368\text{Å} \\ x = 1: a = a^{H} = 3.551\text{Å}, \quad b = b^{T'} = 6.149\text{Å} \end{cases}$$

In Figure 3-10, the shift in the Raman peak of the Ag mode is shown at different lattice constants. We find that the peak position of the Ag mode of the induced 1T′ phase could

have a blue shift caused by substrate friction, which is consistent with the experimental finding.

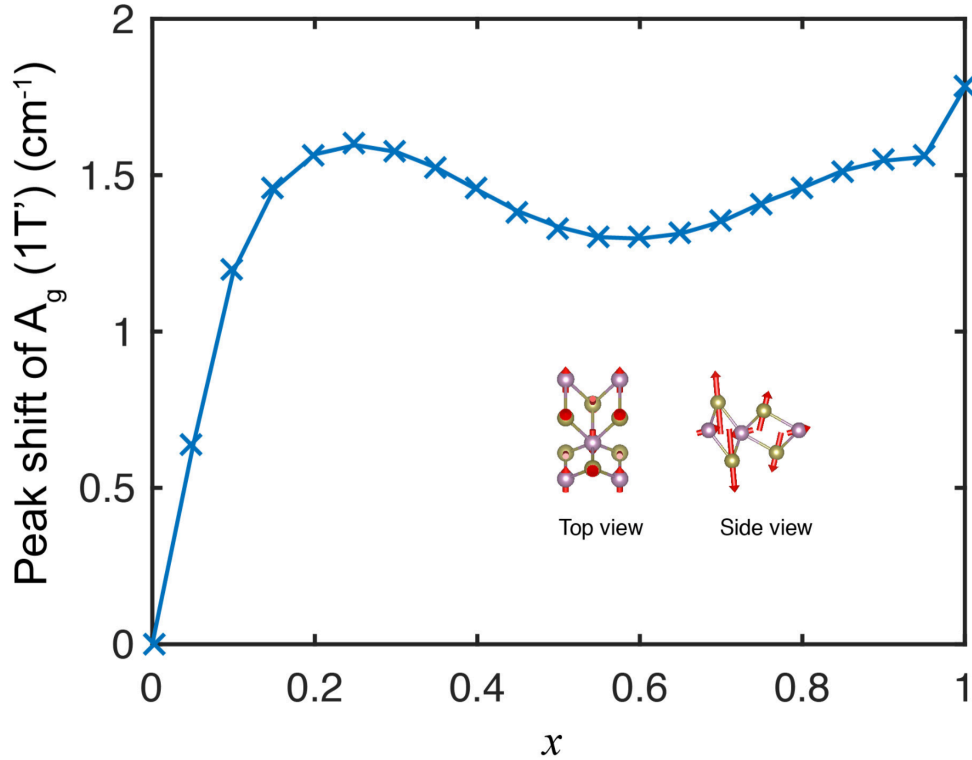

Figure 3-10: Calculated shift in the Raman peak of the A_g mode of the 1T′-phase $MoTe_2$ monolayer owing to strain. The lattice constants range from ($a_{T'}$ $b_{T'}$) at x = 0 to (a_H, b_H) at x = 1. Inset, top and side views of the atomic displacement pattern of the A_g mode. The magnitude of the displacements is proportional to the length of the red arrows. Purple and yellow spheres denote molybdenum and tellurium atoms, respectively.

3.5 Hysteresis and Reversibility of phase transition

To uncover the phase status of monolayer, we did analyze Raman spectra at various gates and use Lorentz model to fit out the weight of different phases. At median gate voltages, Raman peaks were observed, indicating a mixture of 2H and 1T' phases. To extract separate Raman components of 1T' and 2H phases, the Raman mixture in the range of 160 to 180 cm^{-1} is fitted with Lorentz model (Figure 3-11):

$$y = y_0 + \frac{2A}{\pi} * \frac{w}{4(x - x_c)^2 + w^2} \tag{3.4}$$

which peaks at x_c with a width w and an amplitude A; x and y denote the wavenumber and Raman intensity, respectively. The green and blue fitting lines in Figure 3-11 represent the 2H and 1T′ phases, respectively. Before and after the phase transition, only one phase exists and can be well fitted. But at 3.6 V bias, it shows a typical Raman mixture obtained during the phase transition. With different characteristic peak positions for the 2H and 1T′ phases, the fitting curves can reveal the weights of the 2H and 1T′ Raman modes. We define the fraction of Raman intensity of 1T' phase over the whole of 2H and 1T' phase as F=1T'(A_g)/[2H(A_1')+1T'(A_g)]. Gate dependence of F is plotted in black and red curves, referring to forward and backward gate-sweep respectively (see in Figure 3-12). Before 2.8 V in forward sweep, the ratio F remains to be around zero, meaning negligible portion of 1T' phase presence. In this region, 2H phase is still dominant with almost unchanged Raman shift. After further adding up gate bias, F starts increasing sharply and approaching to 1 with 1 V extra bias, revealing nearly complete phase transition to 1T' phase. Then by backward sweeping the gate voltage, the flake keeps staying at 1T' phase until tuning down bias to 2.4 V. 2H phase begins to restore since then and reaches to the full recovery at 1.2 V. The width of this hysteresis loop, in terms of gate voltage, is around 1.8 V. Therefore, reversible phase transition is realized, accompanying with a hysteretic loop.

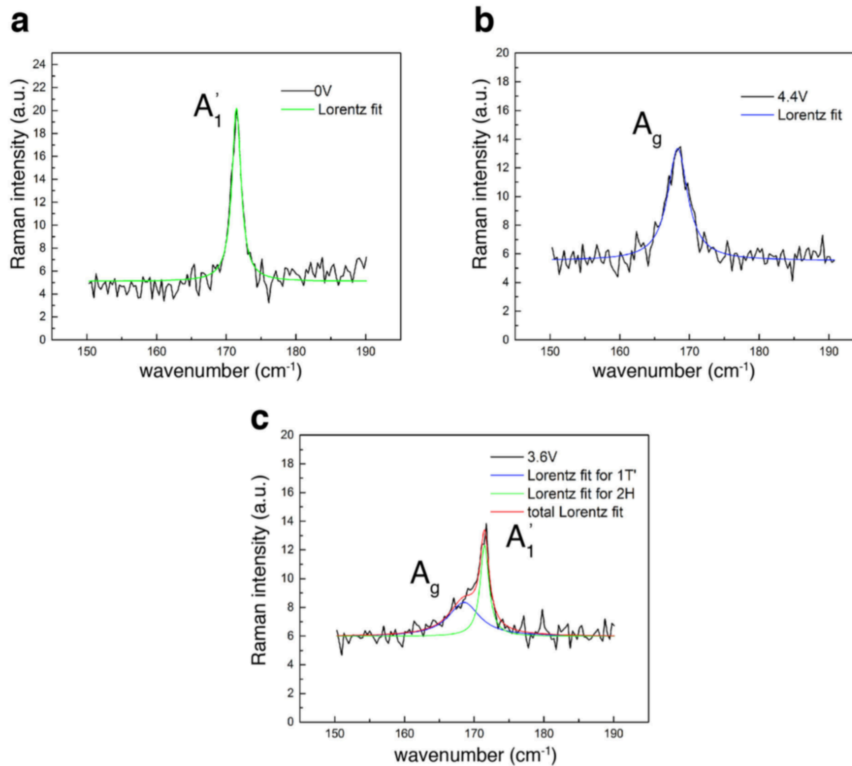

Figure 3-11: Fitting of the Lorentz function for Raman spectra at different biases. **a**, **b**, Raman spectra at 0 V and 4.4 V are well fitted by only one Lorentz function, representing a single Raman mode (A_1' in the 2H phase, and A_g in the 1T′ phase). **c**, A typical Raman spectrum taken during transition from one phase to another (for example, at a bias of 3.6 V) is well fitted by two Lorentz functions, centred at A_1' and A_g.

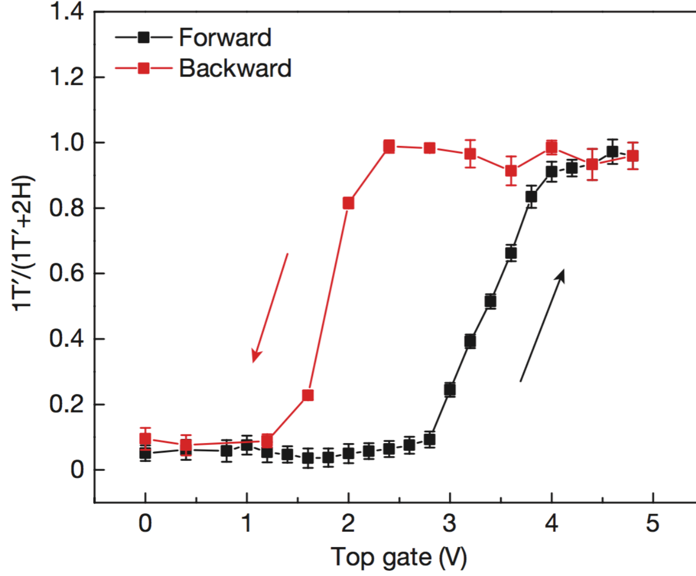

Figure 3-12: Gate-dependent Raman intensity ratios of 1T' over the whole flake. The ratio F = 1T′(Ag)/[2H(A_1′)+1T′(Ag)] (y-axis) , shows hysteresis under an electrical field scan, with a loop width as large as 1.8 V. The black and red curves show increasing and decreasing gate voltage, respectively. The Raman intensity for each mode was extracted from Lorentz fitting of the Raman mixture in the range 160 cm^{-1} to 180 cm^{-1} from Figure 3-8. The error bars represent the standard error propagated from the fitting parameters. The transformation of phonon modes and the corresponding hysteresis loop indicate a clear structural phase transition between 2H and 1T′ phases under gate control.

3.6 Hall measurement and mechanism discussion

To understand the mechanism to drive such phase transition, we performed Hall and Raman measurement on another device with Hall bar geometry. Similar to last session, a typical hysteresis loop in in gate-dependent ratio of 1T' phase Raman intensity to the whole Raman was repeated in Figure 3-13. According to Preisach model, the threshold gate bias for the phase transition (Figure 3-13 (a)) is determined to be 3.2 V, marked by red dashed line. At this particular gate bias, a Hall measurement under magnetic field B up to 9T was performed on the same device. Figure 3-13b shows the Hall resistance R_{xy} as a function of magnetic field B at 3.2 V. The Hall resistance curve is well linear fitted (black dash line) and infers the estimated sheet carrier density to be $2.2 * 10^{14} cm^{-2}$, which is derived by $n_{2D} = 1/|R_H e|$, $R_H = \frac{R_{xy}(B)-R_{xy}(0)}{B}$, where $R_{xy}(B)$ is the transverse resistance under B field and $R_{xy}(0)$ is the transverse resistance without B field. This doping level is higher than that predicted in the theoretical paper [116] ($0.4{\sim}1\times10^{14}$ cm^{-2}). We suspect such difference results from presence of kinetic barriers during transition, which are not considered in theoretical calculation due to its computational complicity. Such kinetic barrier results in hysteresis and set higher doping level requirement for transition.

To compare with the theoretical estimation, which ignores kinetic barrier, we need to redefine the critical voltage and corresponding carrier density where two phases are

degenerate. Following a typical method [120], such critical voltage is determined to be the middle point in hysteretic loop and is the average of voltages at which the transitions of 2H→1T' and 1T'→2H start. In the hysteresis loop (Figure 3-13c), the starting voltage in forward 2H-1T'transition is 2.6 V while starting voltage of the reveral transition is 2.2 V. Therefore, the redefined critical voltage is 2.4 V. In the following, we measured out the carrier density at such voltage and compare it with theoretical value.

Figure 3-13d shows the Hall resistance R_{xy} as a function of magnetic field B at 2.4 V and the carrier density infers to be $0.85\times10^{14}\ \mathrm{cm}^{-2}$ by linear doping. After taking uncertainty ±0.1 V of determination of critical voltage, equivalent to one scanning step used in gate-dependent Raman measurement, critical carrier density is a range that is centered at $0.85\times10^{14}\mathrm{cm}^{-2}$ with an uncertainty of $\pm0.16\times10^{14}\mathrm{cm}^{-2}$. This range sits within theoretically predicted carriers range ($0.4\sim1\times10^{14}\mathrm{cm}^{-2}$). This consistency confirms the electrostatic doping mechanism for driving phase transition. The low and high ends of the predicted range correspond to constant stress (the monolayer is freely suspended) and constant area (lattice constant clamped) conditions, respectively [116]. In real experimental scenario, monolayers are supported by the substrate with surface friction. It is suspected that the substrate friction limits the structural relaxation partially for the monolayer flake. Therefore, the measured critical carrier density is reasonable to sit in between low and high end of predicted values.

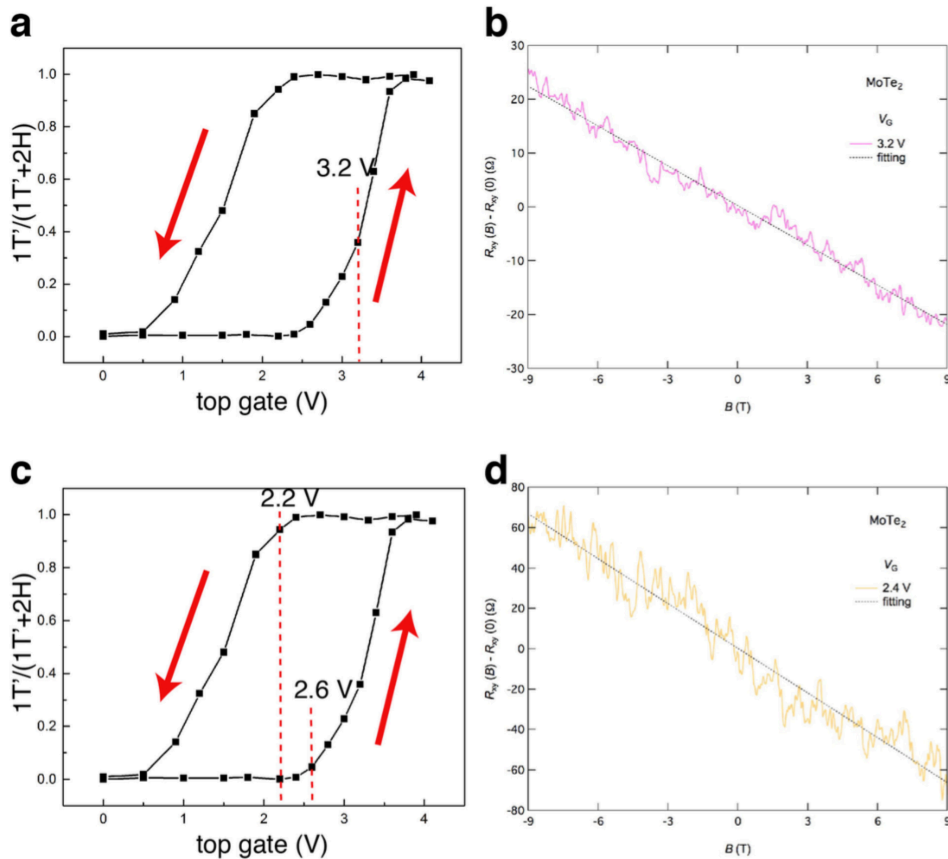

Figure 3-13: Analysis of the mechanism of phase transition from 2H to 1T′ by the Hall effect. **a,c**, Gate-dependent Raman intensity ratio. The ratio (1T′/1T′ + 2H)) is

extracted from Lorentz fitting of Raman spectroscopy at each gate. Red arrows show gate sweeping forward and backward. From a, we determine the threshold for transition from phase 2H to 1T′ to be 3.2 V (red dashed line) on the basis of fitting with the Preisach model. **b,d**, The Hall resistance [Rxy – Rxy(0)] for the same sample at 3.2 V (b) and 2.4 V (d), as a function of the magnetic field, B. Here R_{xy} is the transverse resistance under the magnetic field while $R_{xy}(0)$ is the transverse resistance without magnetic field. The slopes of their linear fittings (dashed lines) give the corresponding carrier densities to be 2.2×10^{14} cm^{-2} and 8.5×10^{13} cm^{-2}, respectively. The latter, which excludes the kinetic barrier, matches the carrier range that is predicted7 to drive this phase transition ($0.4–1 \times 10^{14}$ cm^{-2}).

3.7 Preservation of crystal orientation during phase transition

The microscopic immigration of atoms is significant to understand thermodynamics of phase transition. Polarized Raman and second harmonic generation are sensitive probes for symmetry in solid crystal. And we found a strong correlation of crystal orientation from lattice evolution during phase transition.

According to symmetry analysis and density functional theory (DFT) calculation, A_1' mode of 2H phase $MoTe_2$ has only diagonal components with identical scattering strength for $A_1'{}_{(xx)}$ and $A_1'{}_{(yy)}$ in Raman tensor, while A_g mode of 1T' phase $MoTe_2$ has significant scattering anisotropy with $A_{g(xx)} : A_{g(yy)} = 2.3: 1$ (Methods). The Raman tensor is in the following form:

$$\begin{bmatrix} \alpha_{xx} & 0 & 0 \\ 0 & \alpha_{yy} & 0 \\ 0 & 0 & 0 \end{bmatrix}$$

where α_{xx}/α_{yy}=2.3. And this ratio could be resolved from polarized Raman spectroscopy. Polarized Raman intensity is proportional to $|\widehat{e_i} \cdot R \cdot \widehat{e_s}|^2$ where $\widehat{e_i}$ and $\widehat{e_s}$ are the polarizations of the incident and scattered photons, while R is the Raman tensor for a given mode. In our Raman measurement configuration, the laser excitation is linear polarized and the polarization can be rotated by a half-wave plate. Meanwhile, there is no selection on scatter polarization. Therefore, the measured Raman intensity is the summation of both parallel and perpendicular scattering components with respect to the incident polarization. Given the calculated Raman tensor for A_g mode and $\widehat{e_i} = (\cos\theta, \sin\theta)$ where the angle θ is measured with respect to X' axis in 1T' phase, the angular Raman intensity is expected to be proportional to $\frac{1}{2} \cdot \left[\left(a_{xx}^2 + a_{yy}^2\right) + \left(a_{xx}^2 - a_{yy}^2\right)\cos 2\theta\right]$. In 2H phase, polarized Raman is angular independent, because $a_{xx} = a_{xx}$. In contrast, we expect to observe a two-fold pattern for 1T' phase, which was indeed observed in exfoliated monolayer 1T' $MoTe_2$ (see in Figure 3-14).

With the knowledge of polarized Raman pattern for pristine 2H and 1T' phase, we studied the bonding orientation correlation between the two phases to understand the microscopic lattice change during the transition via electrostatic control. We compared polarized patterns at 0 V and 4V, a circular and two-lobe pattern were observed, respectively (Figure 3-15). The axis connecting the Raman scattering maximums in two lobes is the direction of Mo chain along the X' coordinate shown in Figure 3-1.

While circular pattern at 0V tells little information about crystal orientation of 2H phase, polarization dependence of second harmonic generation (SHG) was employed instead. 2H monolayer crystal belongs to D_{3h} space group with a 3-fold rotation symmetry along the z-axis, and a mirror symmetry with respect to the x-z plane, given coordinate axes depicted in Figure 3-1. Therefore, the only nonzero tensor components responsible for the SHG signal are χ_{xxx}, χ_{xyy}, χ_{yxy} and χ_{yyx}, with the following relationship: $\chi_{xxx} = -\chi_{xyy} = -\chi_{yxy} = -\chi_{yyx}$. When the polarization of the excitation and the detection are kept the same and rotate together with respect to the crystal, the SHG intensity response is simply: $I = I_0 \cos^2 (3\theta+\theta_0)$, where θ is crystal angle, θ_0 is the angle difference between laser polarization and crystal angle. As shown in Figure 3-16, monolayer 2H $MoTe_2$ shows strong SHG signal under 1066 nm ultrafast laser pump. By rotating excitation and detection polarizations co-directionally, a six-fold SHG pattern is clearly revealed with a minimum SHG pointing to zigzag direction (X coordinate in Figure 3-17). Intriguingly, we found that the zigzag direction in original 2H phase (0 V) completely overlaps with distorted Mo-zigzag chain direction (along X' coordinate in Figure 3-17) in gate-induced 1T' phase. It indicates keeping zigzag axis in 2H phase the same as distorted Mo zigzag chain direction in 1T' phase is energetically favorable during intra-layer atomic plane gliding and has been suggested by previous study with scanning transmission electron microscope (STEM) [121]. Contrast to the studied area under STEM around 10 nm^2, our observation confirms this orientation locking is strictly followed in a much larger scale (~10 μm^2). Besides, the polarized SHG patterns at zero bias before and after a full loop of gate scanning are compared. Not only six-fold pattern for 2H phase restores, but the crystal orientation recovers as well (Figure 3-16). Such reversibility of crystal orientation guarantees predictable crystal evolution under gate operation and is significant for potential phase-transition devices with repetitive cycles.

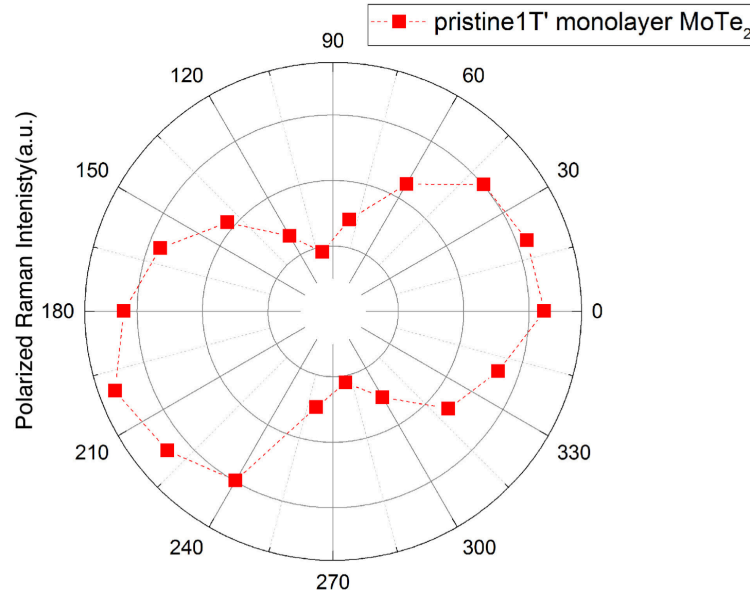

Figure 3-14: Angular polarized Raman (A_g mode) pattern on an exfoliated 1T′-phase $MoTe_2$ monolayer. The position of zero degrees is arbitrary. By rotating the

polarization of the excitation laser, we detected a twofold pattern, verifying the anisotropic *xx* and *yy* components in the A_g Raman tensor.

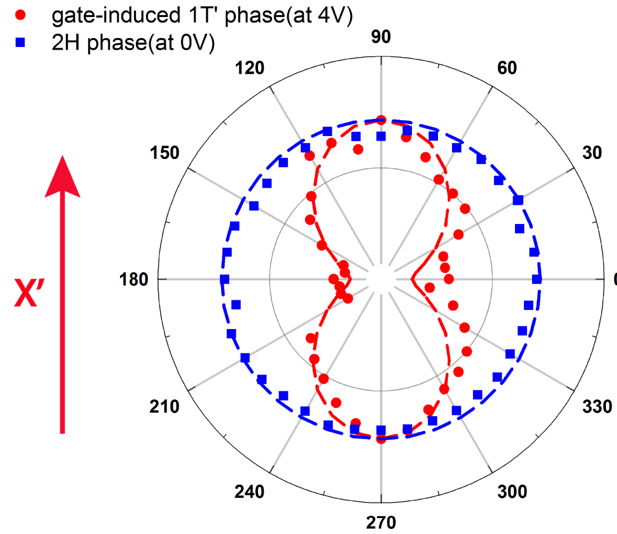

Figure 3-15: Raman intensity from monolayer $MoTe_2$ as a function of crystal angle. The polar pattern of A_1' mode in 2H phase at 0 V bias (blue squares) is well fitted by a circle (blue dashed line), which shows isotropic Raman scattering. In contrast, the distorted 1T' phase at 4 V bias exhibits a two-lobe Raman scattering pattern (red dots), agreeing well with our calculation of anisotropic A_g mode Raman tensor (red dashed line).

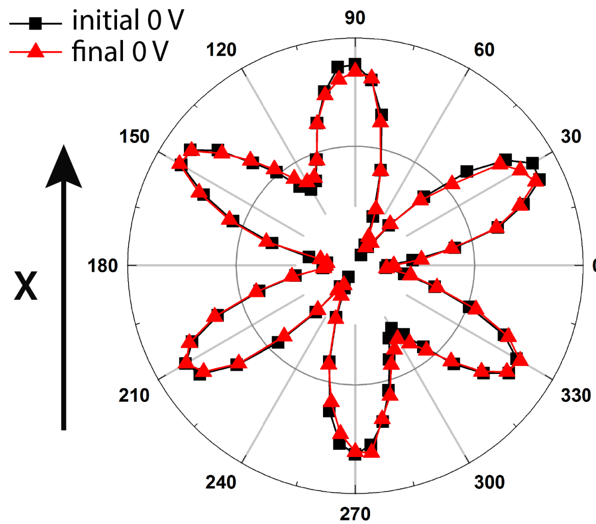

Figure 3-16: SHG intensity from the same monolayer sample as a function of crystal angle. The initial 2H phase at 0 V shows typical six-fold pattern (black

square connected by black line). The armchair direction in 2H phase (directed by X axis, which is defined in next figure) and distorted Mo atom direction in 1T' phase (directed by X' axis, in the following figure) are observed to completely overlap with each other. In addition, the same six-fold pattern fully restores in final 2H phase at 0 V after regrowth from 1T' phase (red square connected by red line). Such crystal axes' overlap and restoration indicate preservation of crystal orientation through the phase transitions.

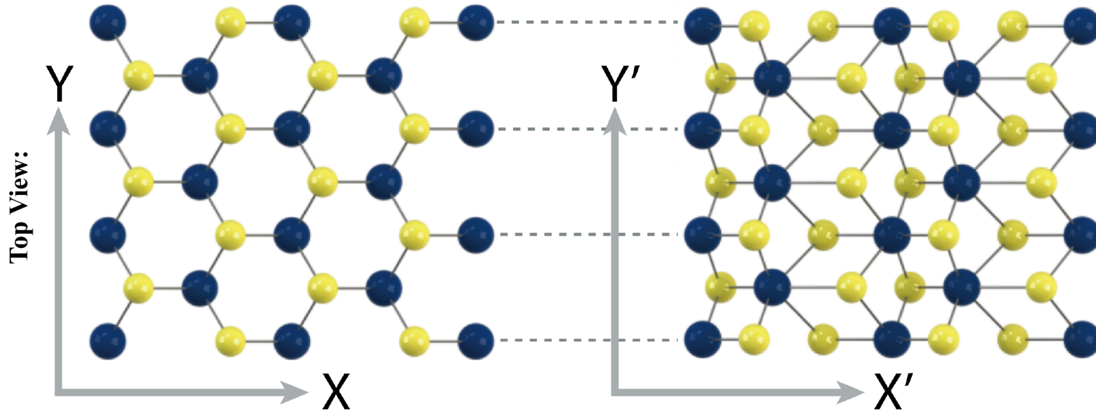

Figure 3-17: top views of 2H (left) and 1T' phases (right).And X, Y directions refers to armchair and zigzag direction accordingly.

3.8 Uniformity during phase transition

All measurements mentioned above is based on single spot, whose size is laser light spot. We conducted study on the distribution of phase transition spatially through SHG mapping during phase change and found out transition occurs uniformly among the whole flake, which is an important step towards applications. Instead of Raman mapping, we mainly employed SHG as an effective probe for image because the integrated time is 60 times less while maintaining the same signal-to-noise ratio. Unlike peak shifts in Raman spectra when phase changes, intensity of SHG dramatically varies, as a probe of phase. By applying forward bias up to 4 V, a typical gate scan with fine step was obtained and is shown in Figure 3-18. When the gate bias tunes up from 0 V, the SHG intensity gradually increases due to absorption profile modification by doping in 2H phase. Further increasing bias from 2.2 to 3.6 V, SHG intensity shows a sharp decrease of more than one order of magnitude. Such drop is attributed to transition from 2H phase to 1T' phase. We mentioned in the section above, 2H phase has none-zero tensor components due to broken inversion symmetry while 1T' phase is opposite. Therefore, intensity of SHG is a very sensitive probe for symmetry through the variation of intensity.

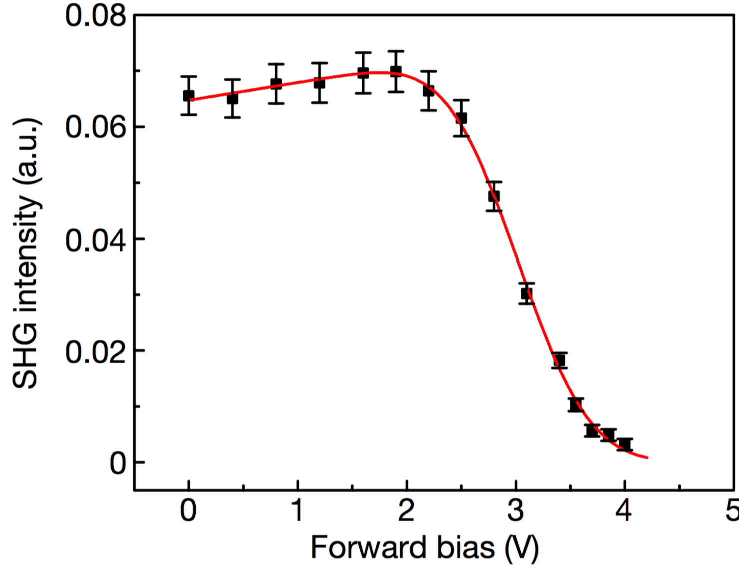

Figure 3-18: Typical gate dependent SHG intensity under forward bias from target monolayer. Voltage bias from 2 to 4V, SHG intensity (black square) shows a sharp decrease to noise level. Such drop mainly attributes to formation of 1T' phase which restores the inversion symmetry.

Several SHG intensity mappings at typical biases are shown in Figure 3-20 and indeed display uniform SHG intensity over the whole flake. Simultaneously dimming over the whole flake as gate increases, refers to a uniform transition from 2H (broken inversion symmetry) to 1T' phase (inversion symmetry). To quantitatively study the uniformity of such transition, the SHG change at each spatial point is analyzed through the fitting model discussed below, and threshold is plotted out in Figure 3-21.

There are several common features in the gate dependence of SHG data throughout the film. First, from 0-2 V the SHG intensity slightly increases, which we attributed to the shift of SHG resonance peak of 2H phase as a function of doping level. Since the excitation wavelength is not close to any optical resonance, we assume that the dependence is weak and approximately linear. Second, the SHG gradually decreases between 2-4 V due to phase transition to 1T' phase. The transition can be well described by Preisach model [122], i.e. each of the pixels contains many nucleation centers with different transition points. According to the literature [123], we assumed the transition points obey Gaussian distribution and thus the fraction of 1T' area is an error function of the gate. Third, the signal finally converges to a non-zero background level. Therefore, we built the following model to describe the gate dependence of SHG: $I = (A + Bx)(1 - erf((x - C) / D) + 0.003$, where A is the SHG intensity at 0 V, B is the gate dependence of 2H SHG, C is the center of transition voltage and D is the deviation. The background of 0.003 is measured in a clean area without sample that came from the electronics of the setup. Figure 3-18 shows the model fits very well to the experimental data. By applying this type of fitting to the whole flake, we mapped out the spatial distribution of voltage threshold (Figure 3-21). Except for a few points at the edge, the critical voltages over monolayer $MoTe_2$ center at 3 V with small standard deviation of 0.1

V, indicating a near uniform and global transition with substantial crystal symmetry change over tens of micrometer scale controlled by electrostatic gating.

Even though Raman mapping is not an efficient way to quantitatively study spatial distribution of threshold over the whole flake, we did do Raman mapping to qualitatively reveal uniformity of phase transition. Firstly, representative Raman spectra from one single spot (~ 0.5 μm * 0.5 μm) of this flake under various gate bias (Figure 3-22b) show Raman peak changing from $A_1^{'}$ (2H phase) to A_g (1T' phase). Three mappings at typical voltages: 0 V, 2.8 V, 4 V (before, during, after phase transition) are chosen to display uniformity over the whole flake. Each pixel's intensity is the integration of characteristic Raman peak within FWHM window. Given the coexistence of 2H and 1T' phases at 2.8V, the integration area is centered in the middle of $A_1^{'}$ (2H phase) and A_g (1T' phase). All integration regions are shadowed in -Figure 3-22c-e. We found little intensity variation in each Raman mapping (before, during, after phase transition in Figure 3-22f-h) over the whole flake. Such observations conclude that this $5\times15\mu m^2$ monolayer $MoTe_2$ undergoes a uniform transition over the whole flake, consistent with our previous SHG mapping result.

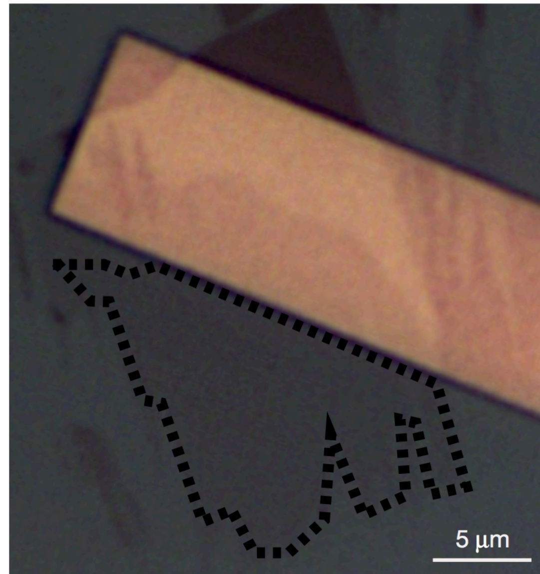

Figure 3-19: Optical image of a monolayer $MoTe_2$ flake to explore uniformity. Flake is circulated by black dash line.

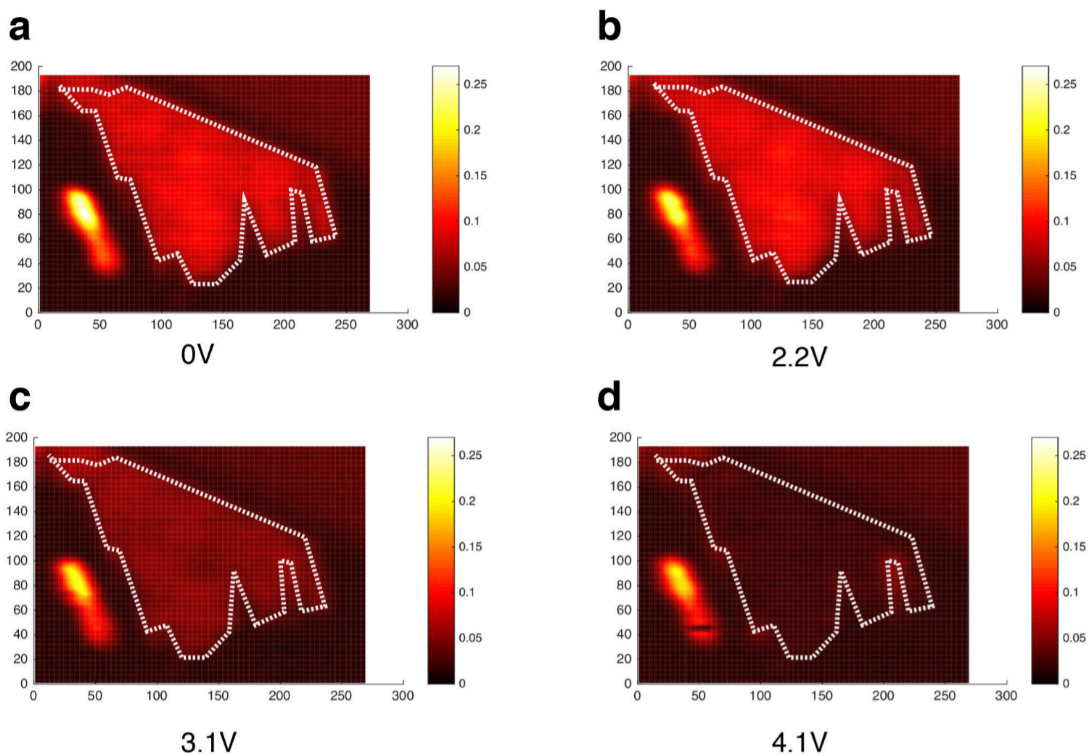

Figure 3-20: SHG mapping at several typical voltage biases. a–d, These biases correspond to before (0 V and 2.2 V; a, b), during (3.1 V; c) and after (4.1 V; d) phase transition.

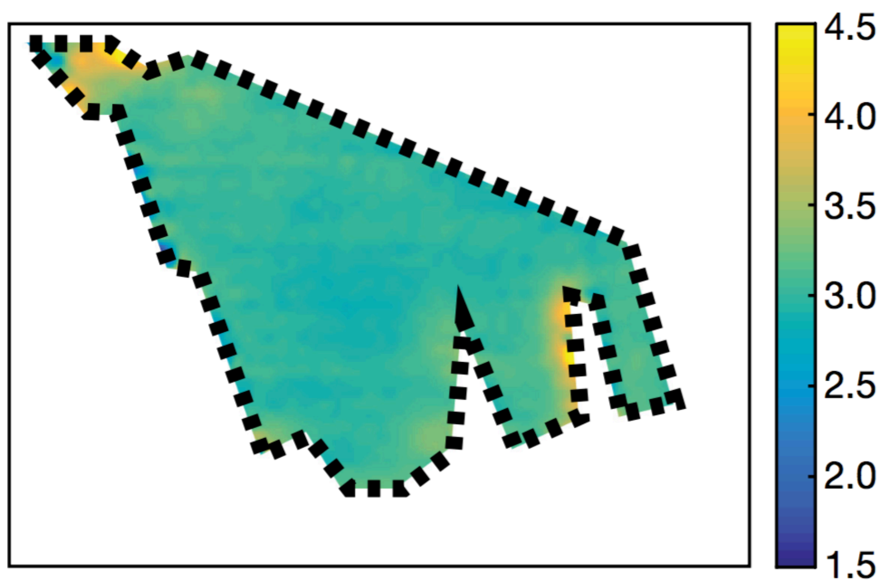

Figure 3-21: Spatial distribution of voltage threshold obtained by fitting. Target monolayer shows voltage thresholds center at 3V, with 0.1 V standard deviation across the 2D crystal, indicating the uniform and global structural phase transition.

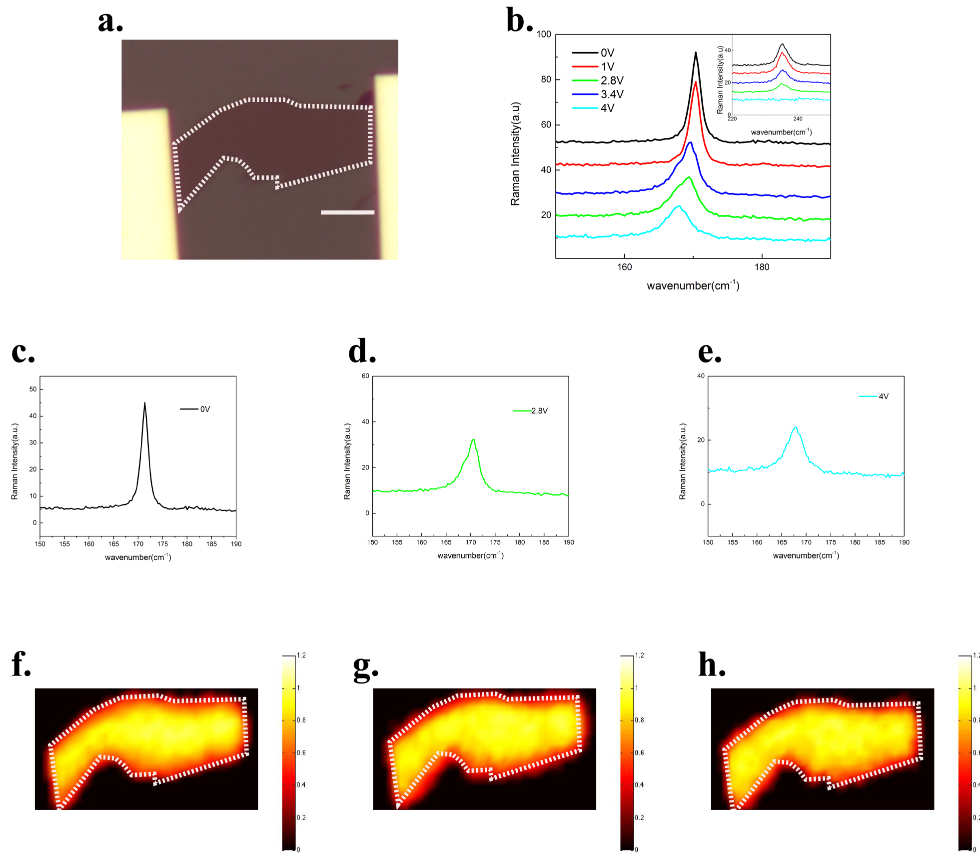

Figure 3-22: Raman mapping of phase transition in monolayer $MoTe_2$. a, Optical image of a monolayer $MoTe_2$ flake (encircled by white dash line) in contact with electrodes. The scale bar is 5 µm. b, Representative Raman spectra from one spot of the flake. Disappearance of A_1' mode at 171.5 cm^{-1} from 2H and appearance of A_g mode at 167.5 cm^{-1} from 1T' phase are shown when bias changes from 0V to 4V. Another peak (E' mode at 236 cm^{-1}) of 2H phase fades as gate increases (inset). c-e, Integration range on a single spectroscopy before (0 V), during (2.8 V) and after (4 V) phase transition. At 0V and 4V, shadowed areas are centered at characteristic peaks (171.5 cm^{-1} and 167.5 cm^{-1} respectively), with FWHM as area width. Not a single peak observed during phase transition (at 2.8V), middle point between A_{1g} and B_{1g} is chosen as center of integration region instead, with FWHM as area width. f-h, spatial Raman mapping at each gate following the integration area in c-e. Little variance of Raman intensity over the whole flake proves that the phase transition is uniform.

3.9 Exclude other possibilities that induce phase transition

During electrostatic doing induced phase transition, laser is the main tool to probe the status of flakes, such as Raman spectroscopy and SHG. And the power of laser, which is around 1mW/ μm^2 in experiments mentioned above, could locally heat up the flake and thermally induce phase transition. To exclude such possibility, two control experiments

have been conducted. Firstly, a monolayer of 2H $MoTe_2$ without gate bias was continuously exposed to 1mW/ μm^2 633nm laser for 20 hours, which is 4 times longer than the period for one run of gate dependent Raman measurement. Neither new peak nor shift of Raman peaks was observed (Figure 3-23). This proves only 1mW/ μm^2 laser irradiance cannot induce thermal 2H-1T' phase transition, which is consistent with previous report [113]. Secondly, we further rule out the presence of thermal phase transition even with applying gate bias. Two full runs of gate dependent Raman measurements were performed on the sample, excited by 633nm laser with the power of 0.1 mW/ μm^2 and 1mW/ μm^2 respectively. By analyzing the components of 2H ($A_1^{'}$) and 1T' (A_g) phases derived from Lorentz fitting, the gate dependent ratio between Raman intensity of A_g peak and the overall intensity are visualized for each power condition. We found that both thresholds and hysteretic loop are the same under either excitation power. Such observation contradicts thermal phase transition scenario given one order power difference is expected to results in substantial difference in kinetic barrier. This power independence of hysteresis confirms that the possibility of thermal-induced phase transition is negligible. The rationale for this insignificant local heating at 1mW/ μm^2 irradiance is analyzed in the following.

Temperature dependent and power dependent Raman measurements have been conducted to estimate local temperature. In Figure 3-24, under 0.01 mW/μm^2 irradiance, both $A_1^{'}$ and $E^{'}$ modes show a linear Raman peak shift (black squares) as system temperature changes. Based on such linear relationship and corresponding fitting (red curve) [124] the first-order temperature coefficient (χ_T) is -0.00589 cm^{-1}/K for $A_1^{'}$ and -0.00949 cm^{-1}/K for $E^{'}$ respectively. In contrast to Raman peak positions under 0.01 mW/ μm^2 excitation at 220K, both Raman modes exhibit red shift $\Delta\omega$ within 0.2 cm^{-1} under 1 mW/ μm^2 excitation (red square). Those red shifts indicate about 15~18 K local temperature increasing, calculated from $\Delta T = \Delta\omega / \chi_T$ for both modes. Therefore, local temperature at the laser spot region is about 235~238 K, which is far away from transition temperature (~780K) required for thermal induced 2H-1T' phase transition [113]. The reason for such small temperature change compared with Yamada, et al. is due to the low absorption of monolayer $MoTe_2$ (~ 3%) [125,126], as well as higher thermal conductivity of SiO_2/Si substrate. Thus, the accumulated heating is negligible compared with the temperature rise needed for phase transition in bulk $MoTe_2$ [111]. From power-independence of hysteresis and small local heating under laser excitation, we exclude the thermal effect during the phase transition and confirm the electrostatic doping mechanism.

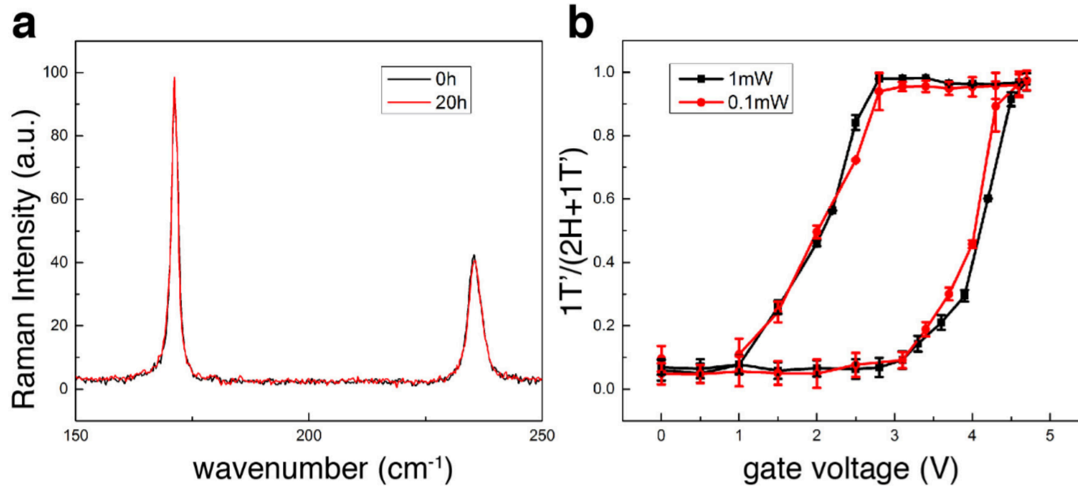

Figure 3-23: Thermally induced factors during phase transition. a, Raman spectra of monolayer 2H $MoTe_2$ before and after exposure to a 1 mW μm^{-2}, 633-nm laser for 20 hours. A shift in neither peak intensity nor peak position is observed. b, Gate-dependent Raman intensity ratio (1T′/(2H + 1T′)) under different laser-power excitations: 1 mWμm^{-2} or 0.1 mWμm^{-2}. At each gate voltage, the intensity for the 2H phase (or 1T′ phase) Raman mode A_1' (or A_g) was extracted by Lorentz fitting of the Raman mixture in the range 160–180 cm^{-1}. The error bars represent standard errors propagated from the fitting The error bars represent standard errors propagated from the fitting parameters. Given that the thresholds and hysteresis loops are the same at both powers, the transition between the 2H and the 1T′ phase must be independent of laser power and is determined purely by the electrostatic doping level rather than by a thermal effect. All experiments were conducted in a vacuum of 2×10^{-6} torr and at a temperature of 220 K.

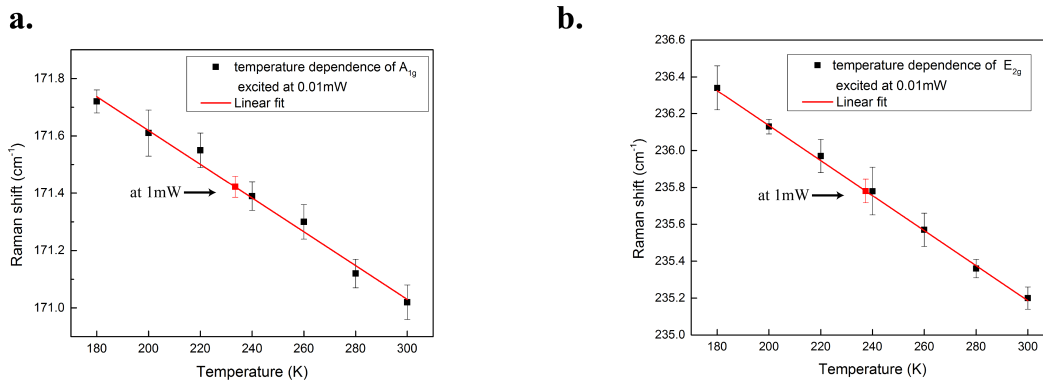

Figure 3-24: Temperature dependence of Raman peaks of monolayer 2H MoTe2.Temperature dependence of A_{1g} and E_{2g} peaks under 0.01 mW/μm^2 laser excitation (plotted in black squares). Both peak positions are well fitted (red lines) and show linear temperature dependences. At 220K, red shifts are observed for higher excitation power (1mW/ μm^2) condition. The red shifts indicate a local rising temperature, which can be derived from linear fitting curves of temperature dependent Raman and has been pointed out by red squares. Both A_{1g} and E_{2g} peak

shifts shows a small temperature increase within 20K induced by 1mW/ μm^2 633nm laser.

Another important possibility to exclude is the detention of ionic liquid's movement leases to hysteresis, which could complex what we observed. Ionic liquid consists with cations and anions in the form of large molecule. While forming electronic double layer on the surface of flake to induce doping, ions take time to move and if the sweeping speed for gate control is too fast to follow, a 'fake' hysteresis loop could be formed and obfuscates the intrinsic hysteresis of phase transition. To minimize this effect, the stabilization time for each gate in all experiments mentioned above has been extended to 2 minutes [9]. To ensure the validity of this solution, we conducted another SHG measurement on bilayer $MoTe_2$, shown in Figure 3-26. Because of prolong stabilization time, no hysteresis was observed. The absence of hysteresis in bilayer can be expected since more electrons are required to induce phase transition on system with a larger density of states. This observation also excludes the possibility the observed hysteresis on monolayer (see in Figure 3-25) originates from ionic liquid. The hysteresis of SHG in monolayer is consistent with the hysteresis present in Raman with the same width and transition threshold on the same sample. It confirms the hysteresis to be inherent during this phase transition.

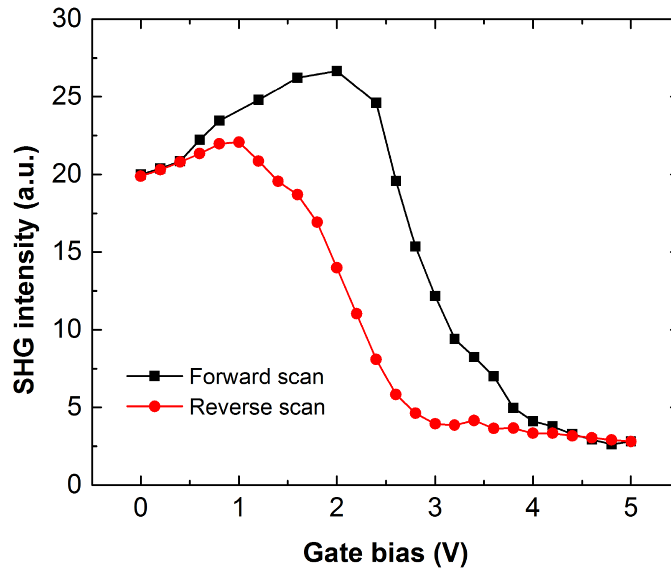

Figure 3-25: Gate dependent SHG on monolayer 2H $MoTe_2$.SHG intensity of monolayer $MoTe_2$ displays significant hysteresis during a forward and backward changing of top gate.

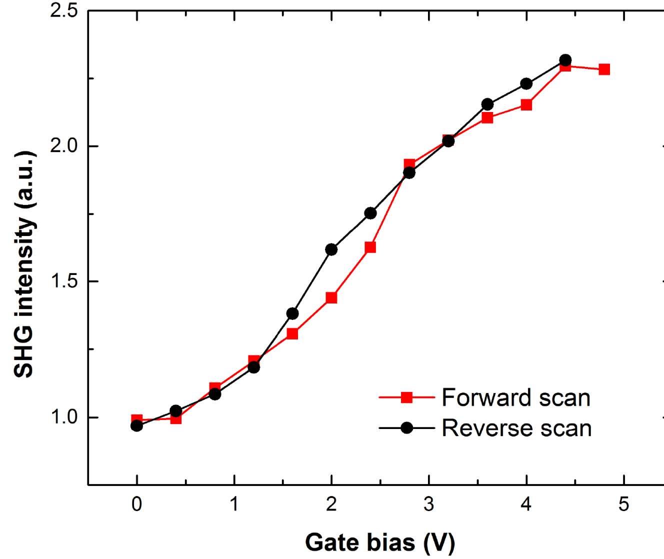

Figure 3-26: SHG intensity of bilayer sample under gate bias. There is no hysteresis under the sweeping of top gate bias.

The third control experiment is to exclude excitonic effect that modifies SHG intensity and clarify symmetry is the main factor that contributes to the disappearance of SHG when flakes transform to 1T' phase. Wavelength scan of SHG intensity was performed before transition (0 V) and after transition (4.4 V) gate bias (Figure 3-27). Without gate bias, a significant resonance at 1100 nm pumping was observed in 2H phase monolayer $MoTe_2$, which is attributable to the 1*s* resonance [127]. For the scan wavelength range from 1020 nm to 1160 nm, SHG intensity at 4.4 V is globally more than one order lower than that at 0 V. Previous studies reported gate bias induced charging can modify resonant strength of neutral and charged excitons or even remove excitonic resonance due to screening of Coulomb interaction [29,128]. Although such modification may lead to SHG intensity drop if the nonlinear optical process is mainly assisted by excitonic resonance, we note that in the previous case for non-resonant excitation, SHG intensity showed almost independence of gate bias scan. By contrast, in monolayer $MoTe_2$ under high gate bias, the substantial decrease of SHG intensity was observed for both resonant and non-resonant pumping. Such observation excludes gate-induced excitonic resonance peak shift and strength modification as main mechanisms for intensity drop. This signature also confirms the presence of 1T' phase with inversion symmetry. To reduce excitonic resonance effect on SHG intensity, we carefully selected 1066 nm as pumping wavelength for other gate-dependent SHG measurements.

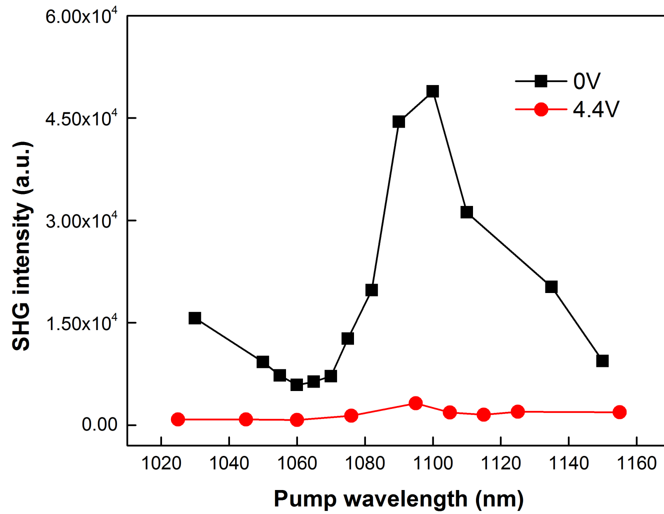

Figure 3-27: SHG intensity versus excitation energy before and after phase transition. At 0 V (black square), a significant excitonic resonance in SHG wavelength scan was observed in 2H phase monolayer $MoTe_2$ at a pump wavelength of 1100 nm. In contrast, while keeping pump power the same, SHG intensity (red dot) at 4.4 V bias shows globally drop by more than one order over the excitation spectrum range. The incident excitation power for each wavelength was fixed the same at the sample plan.

3.10 Summary and outlook

In conclusion, we have demonstrated reversible electrical manipulation of a structural phase transition in monolayer $MoTe_2$. Our method for controlling this phase transition provides a versatile platform for studying the fundamental physics of ordering competition and novel topological phases. In addition, the observed large hysteresis and modulation depth will aid the development of two-dimensional memory and reconfigurable devices. Crystal orientation proves to be reserved, which is the necessity for repetitive operation of memory devices.

Intrinsically, structural change is an ultrafast process as fast as femtosecond. The speed of the device integrated with ionic liquid is limited to the movement of ionic molecules. Upgrading the operation speed of ionic liquid gate would help to reveal the intrinsic timescale for phase transition in 2D material as well as benefits all other EDL-FET, satisfying both on-off ratio as well as modulation frequency. More fundamentally, the evolution of band structure happens before the phase transition does under the influence of quasiparticles. Thus, uncovering of such progress will be novel and important for understanding the role of electrons, from strong interaction region to free electron, in terms of thermal dynamics in phase transition. This is still blank in the field of material science. And two-dimensional materials, whose structures are planar, are best platform to reveal the dynamics of domains, such as growth and mergence as well as emergence of boundary. Taking use of the electronic way to control phases we discovered here, it has broad interests not only for application but also fundamental science.

4 Quantum yield optimization through electrostatic approach

4.1 Introduction

Two-dimensional transition metal dichalcogenides (TMDs) such MoS_2 and $MoTe_2$ are promising candidates for various optoelectronic applications [129,130] not only because they are direct band gap when thinning down to monolayer but also they have strong excitonic feature in photoluminescence, which enable stronger absorption and faster emission. For example, more than 5% light can be absorbed by such atomic thin layer at excitonic resonance. On the other hand, another important criteria to evaluate optoelectronic performance for a material is quantum yield (QY) of photoluminescence (PL). QY is the ratio of the number of photons radiated to the photons absorbed form light source. However, for 2D semiconductor such as MoS_2, the QY is less than 1% [52,131,132], which is too low for practical applications. For 2D optoelectronic applications, two approaches are used to achieve light emission, one is by photon absorption and the other is through electron-hole injection [60,133]. Both of them are substantially limited by low QY of the 2D layered materials. It is highly suspected that the presence of large amount of defects in 2D crystals, either formed intrinsically through growth or extrinsically through fabrication damage, results in such low QY. In other words, defect-assisted states in TMDs trap the excitons and serve as non-radiative channels to prevent effective light emission from the excitons.

Given the high defect density on the order of 10^{12}-$10^{13}/cm^2$, many efforts have been input to increase QY in TMDs by defect reduction. For example, introducing oxygen bonding on the surface is explored to reduce defects inside of crystal [132]. In this report, the authors demonstrated the forming of Mo-O bondings under thermal annealing neutralizes defects and hence deactivates the nonradiative process. Recently, people used chemical treatment to achieve surface passivation on 2D materials by organic superacid, TFSI. Essentially, TSFI adhering the surface of MoS_2 has high chance to be protonated, helping to expose deep-trapped defects and make the passivation process more efficient. This method turns out to be very effective and boosts the QY of MoS_2 by two orders with record-high near-unity QY at room temperature (see in Figure 4-1) [135]. Such performance is already comparable with that of high-quality commercial quantum dot and quantum well emitters. This work has not only brought back the attentions for optoelectronics based on 2D layered materials, but motivated researchers to explore the exact mechanism, which might be generalized to all 2D semiconductors and achieve high optical performance heterojunctions. It is believed that the coated organic superacid helps to remove the contribution of defect-mediated nonradiative recombination of defect site by passivating or repairing them or both. However, the exact mechanism behind this great enhancement is still unclear. In addition, such organic molecules were found just loosely attach the surface of MoS_2 without any chemical bonding and hence this enhance is not stable and cannot be repeatedly used under vacuum and at various temperature.

Here I explored the possibility to use electrical way to stabilize the organic molecules on the surface of MoS_2 as well as dynamics control of the QY. TFSI in ionic liquid

(DEME-TFSI) can be electrically controlled and the density of it on the surface of TMDs can be well determined. We achieved more than 20 times enhancement of PL. With this external control, the mechanism of the enhancement could be quantitatively studied in the near future.

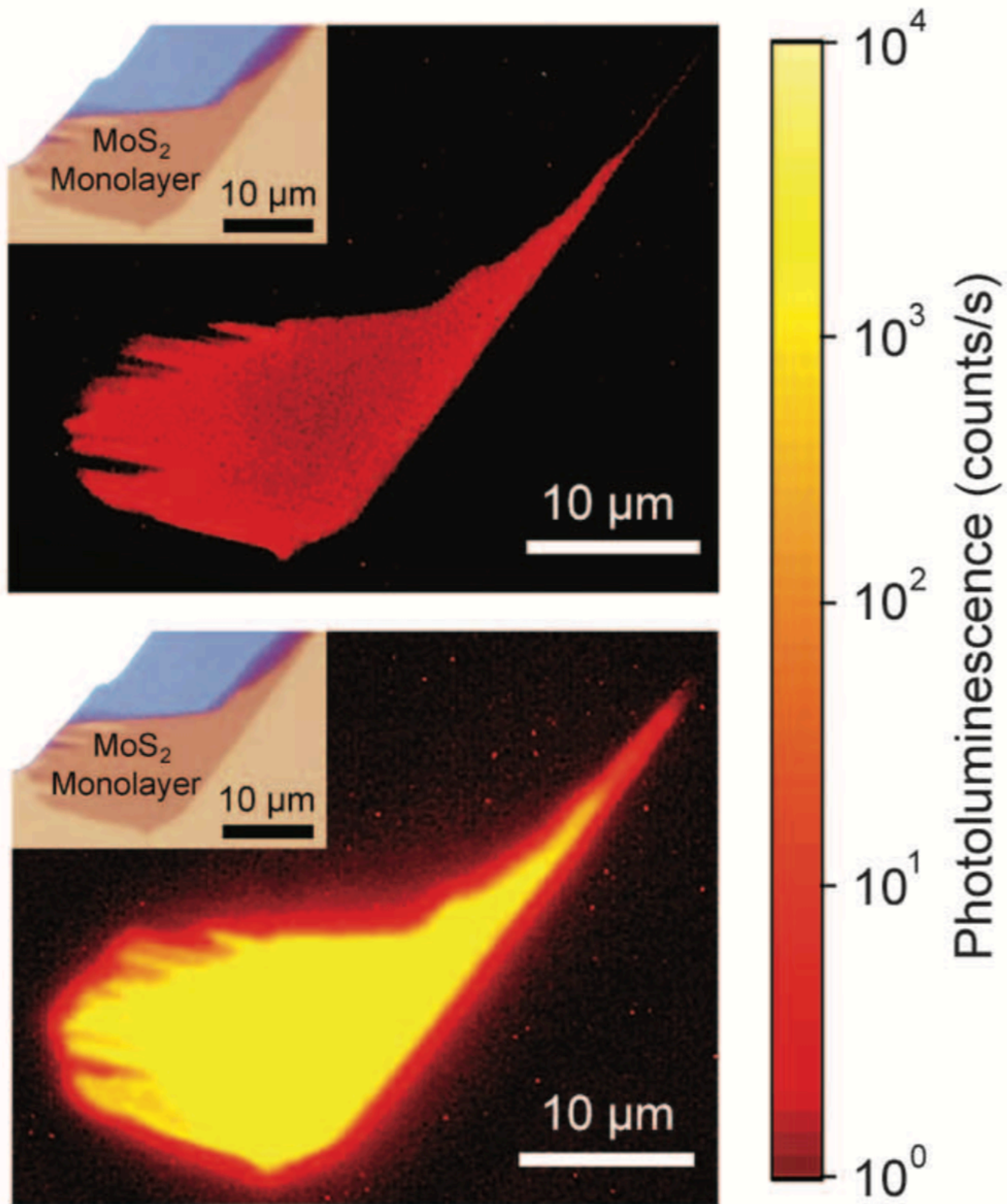

Figure 4-1: PL image of a MoS2 monolayer before and after treatment. Top (bottom) is captured before (after). Reprinted from Ref. [135] with permission from AAAS.

4.2 Experimental design and PL enhancement

In the previous study [135], the employed organic superacid is bis(trifluoromethane)sulfonimide (TFSI). And the chemical treatment includes the immersion of sample into TFSI solution and a subsequent annealing at 100°C for 5 min. And its performance varies from sample to sample, which might result from the quality variation of samples and non-uniformity of coating layer of TFSI (see in Figure 4-2). To make this process more controllable and more applicable under vacuum condition, we make use of ionic liquid (DEME-TFSI) [136] to replace pure TFSI. The ionic liquids have proven highly effective as dielectrics in Electric Double Layer (EDL) devices for ultrahigh electrostatic doping in two-dimensional materials in last chapter. And they are binary mixtures with cations and anions, such as $DEME^+$ and $TFSI^-$ (see in Figure 4-3). For these ions with net charge, we can easily use electric field to control their movement and distribution on the top of 2D material. With such voltage control, the enhancement of QY can be qualitatively studied and it is expected that the performance is stable and repeatable given the external bias maintaining the distribution of ions unchanged. Those ions not only physically attach onto the flake but also modify the doping level in the 2D material, which can further deactivate or screen the defects electrostatically. More importantly, by flipping the sign of applied bias, I can dynamically control of the surface passivation with either $DEME^+$ or $TFSI^-$. This broad polarity coverage is significant to achieve high QY for all 2D semiconductors, whose intrinsic doping types vary from n-doped to p-doped depending on the growth conditions. Another advantage for this method is its broad temperature application range. DEME-TFSI ionic liquid in particular has low glass transition temperature around 182 K [137,138]. Above this transition temperature, it is in liquid form and ions can move following the external field, which guarantees the wide working temperature for this approach.

For this ongoing project, I firstly applied this method to exfoliated monolayer MoS_2. As mentioned before, monolayer MoS_2 exfoliated from naturally grown crystals has quite low QY and it is found to be n-type doped [16]. Therefore, with the proximity to $TFSI^-$, the flake is expected to become electrically neutral. PL enhancement should be achieved because the initial defects are screened and non-radiative channels are suppressed. Following along this line, I made the gate-control device and conducted the measurements. Some preliminary results are shown below.

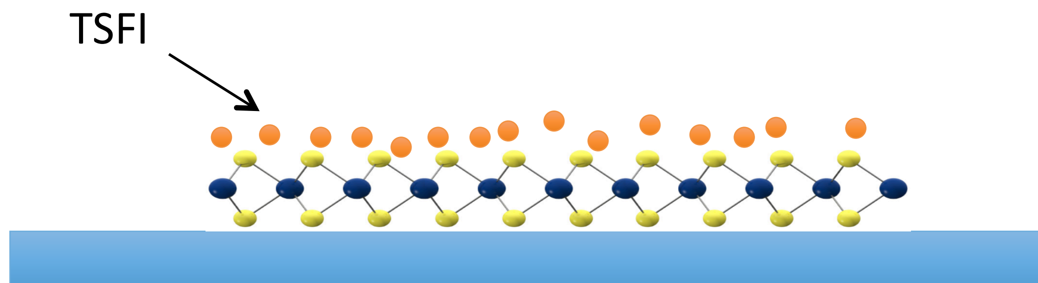

Figure 4-2: MoS_2 with TSFI coating.

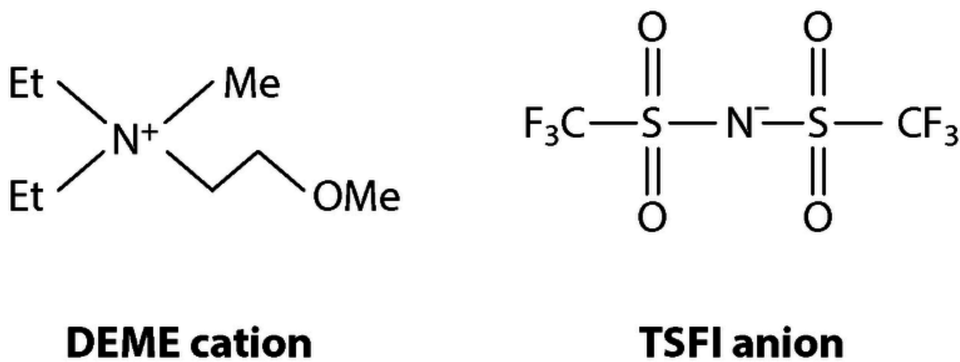

Figure 4-3: Chemical formula of DEME-TFSI. Reprinted permission from Annual Reviews.

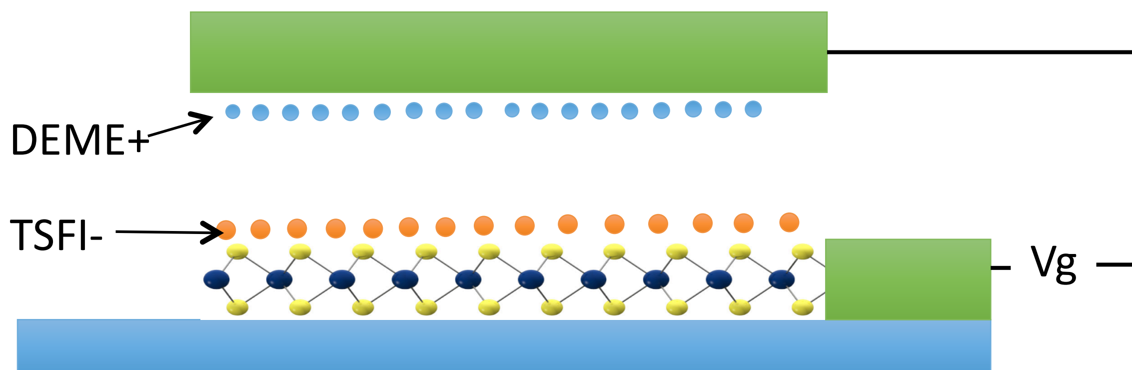

Figure 4-4: Schematics of redistribution of TSFI- on top of MoS_2.

To integrate with ionic liquid and manipulate PL intensity with electrical control, we have the same device design as the one in last chapter about engineering phase transition. MoS_2 monolayers were obtained by mechanically exfoliating bulky single crystals onto a Si wafer covered with a 285 nm thick thermally grown SiO_2 layer. Raman spectroscopy and optical contrast were used to characterize the thickness of samples. After identifying positions of monolayers, electrodes were patterned by standard electron-beam lithography and electrode metal of Ti (5 nm)/Au (100 nm) was deposited through electron beam evaporation. A drop of ionic liquid was cast on the top of device, covering both monolayer flakes and metal pad for gating. The difference here is that $TSFI^-$ is the molecules we want to work with so that the voltage gate is mainly negative and injects holes into the flake to make it electrically neutral. Compared to the chemical treatment, the electrical double layer (EDL) is uniformly distributed and the density of $TSFI^-$ is proportional to the gate voltage applied. The sample was loaded in high vacuum cryostat chamber (Janis ST-500) with electrical access.

The measurement of PL was performed on a commercial PL/Raman spectroscopy system (Horiba Labram HR evolution). The sample was under normal incidence of laser with wavelength at 473nm. The photon energy is above the optical bandgap of monolayer MoS_2 and such excitation can form excitons in the flake. The laser beam was focused on

the sample by a Zeiss 50X long working distance objective (N.A. = 0.65) and the spot size is about 1μm.

To avoid exciton-exciton annihilation [139], very small laser power less than 10 nW was used to excite PL and found negligible PL shown under zero bias. When negatively biasing the gate voltage, PL intensity emerges at -0.5V gate bias and keeps increasing until reaching to the saturation point at -1V (see in Figure 4-5). Further increasing the magnitude of voltage does not change the PL intensity at all. And the largest enhancement of PL observed is over 20 times. If assuming the original quantum yield of monolayer flake is 1%, which is the typical value reported in literature, the QY under electrostatic doping control is around 20%. Although further careful QY calibration is in need, such dynamically controlled enhancement is impressive. Besides the optical performance, the gate-induced doping estimation may shed light on the enhancement mechanism. Given the capacitance of ionic liquid (several $\mu F/cm^2$) and the bias range for PL enhancement is from -0.5V~-1V, the hole doping is around $10^{13}/cm^2$, which is consistent with the defects density in monolayer MoS_2. Such consistency strongly suggests that the charged ions electrically compensate the influence of detects and make them "invisible" to excitons. This hypothesis is further confirmed by the observed saturation behavior of PL, which indicates this effect does not originate from the band structure modification but from the suppression of one type of non-radiative channel. In addition, such saturation behavior infers those non-radiative channels are closely related with the defect sites and cannot simply open by electrical carriers. Furthermore, we also explore the electron doping side under positive gate bias and found no obvious PL changes and PL intensity stays under the noise level (Figure 4-6). Therefore, for n-type materials, only the coating of $TSFI^-$ and the corresponding hole doping lead to the enhancement. And we expect for other p-type two-dimensional material, the coating of $DEME^+$ will work and this method is versatile and in principle can work from the frozen temperature (182K for DEME-TSFI) to the electrochemical reaction temperature (around 475K for DEME-TSFI).

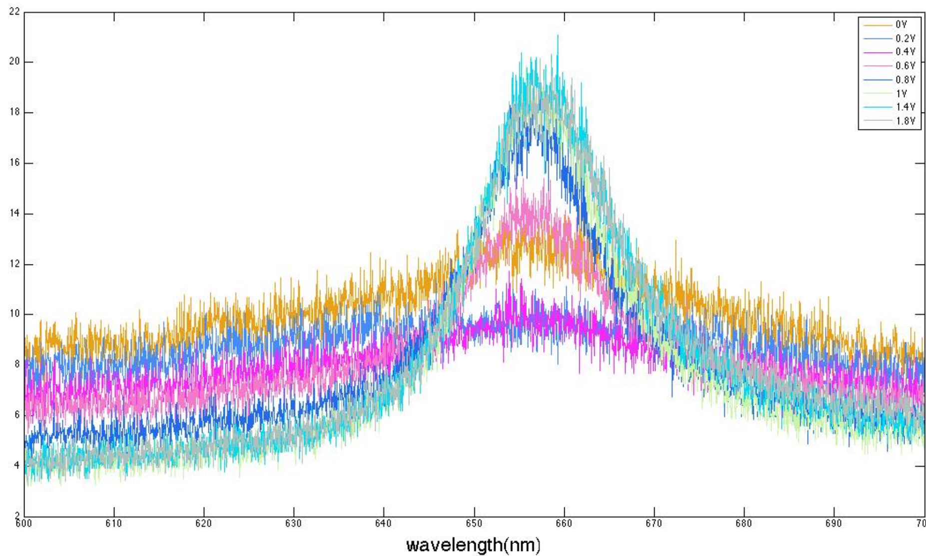

Figure 4-5: Enhancement of PL over 20 times.

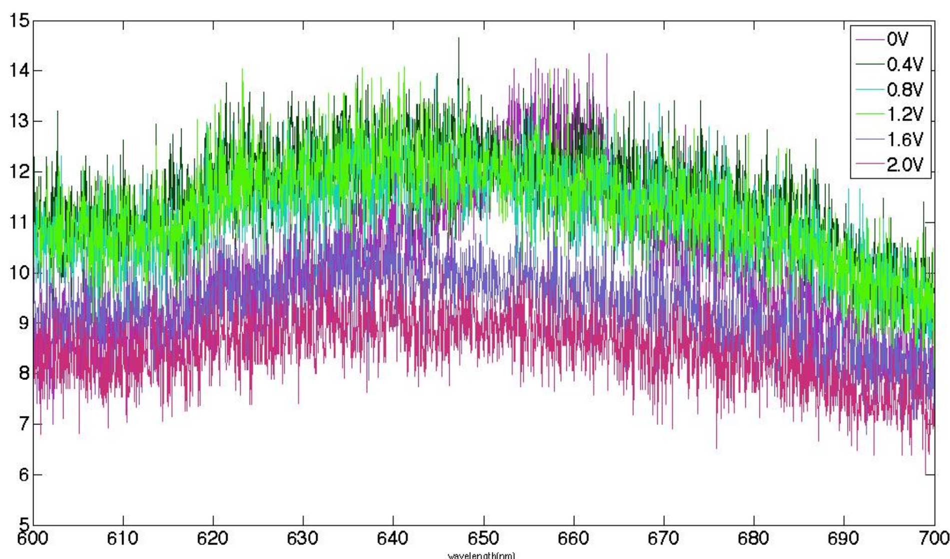

Figure 4-6: No change of PL at electrons side.

4.3 Summary and Outlook

Along the path to achieve high-performance 2D optoelectronic devices, I have demonstrated a versatile method to control PL intensity and QY in two-dimensional materials via ionic liquid gating. It proves to be a stable and controllable approach to decrease non-radiative channel and allows quantitative study of the impact of doping on the PL intensity as well as QY. Specially, in MoS_2 based devices, our preliminary data shows more than 20 times enhancement of QY. If the initial QY is typically reported 1%, then more than 20% QY was achieved through electrostatic ionic gating. Such QY already matches most requirements in optoelectrinonics, such as high performance of light-emitting diodes, solar cells and nano-lasers. Furthermore, the gate-induced doping level for maximum PL enhancement is comparable with intrinsic doping level in monolayer MoS_2. This finding may help to clarify the microscopic mechanism and highlight the role of electrical screening of defect sites.

Regarding future explorations, several directions can be projected. Firstly, a careful QY calibration is in need. With this data, it is clear to tell whether the PL enhancement saturation is due to unity QY or other reasons. In the meantime, it is also interesting to monitor how the exciton lifetime evolves with reduced defect influence. Secondly, it is important to generalize this method to more 2D semiconductors such as WS_2 and test its performance at low temperature. Finally, it is exciting to integrate the device with advanced atomic imaging techniques such as STM to visualize how intrinsic defects are screened as gate bias changes and any structural reconstructions at defect sites take place. This is fundamentally important to unravel the microscopic mechanism of PL loss and enhancement in 2D layered materials, which can contribute to the development of practical 2D photonics.

5 Conclusion and outlook

This thesis mainly presents experimental exploration on the two-dimensional materials by making using of strong quasiparticle-interactions, especially for engineering electronic and structural orderings. We demonstrated a recorded high powerfactor in MoS_2 through optimizing electronic states, whose contribution is deterministic for thermoelectric performance. And the full map of Seebeck coefficient, including temperature and carrier density parameters, reveals the hopping distance between defects as well as phonon-dominated scattering. Further lifting up the population of quasiparticles in monolayer $MoTe_2$, the switch of structural ordering was observed to be dynamic and reversible for the first time. It brought new degrees of freedom into engineering phase transition. Besides that, the modulation depth of nonlinear optical signal was increased one order, compared to traditional mechanism based on excitonic shift. It also realized versatile functionalities, such as semiconductor-metal transistor, trivial to non-trivial topological transition as well as memory device with hysteresis. Meanwhile, quasiparticles also interact with defects inside of materials and we demonstrated one platform to quantitatively study its mechanism, which influences quasiparticles' transport as well as optoelectronic properties. So far, our works and current literature mainly focus on very primitive phenomena despite of a lot of fundamental physics behinds as well as potential application in the field of exploring two-dimensional materials with the strong interaction of quasiparticles. In the rest of this chapter we point out both opportunities and challenges waiting for exploration.

5.1 Nano-engineering of two-dimensional materials

Two-dimensional materials have shown high power factor, determined by its uniqueness of DOS and large degeneracy of conduction band. Beside electronic states, the efficiency of thermoelectric device relies on low thermal conductivity to limit energy loss to phonon [140]. Integrating nano-disorders and defects is one option to limits phonon modes sacrificing electronic properties. New approach to circumvent this side effect is vital for the field of thermoelectricity. Recently, two-dimensional materials are found with non-trivial topology state [141]. In such system, electronic band are immune to backscattering by disorders and defects, while phonons are not [142]. We envision that using the decoupled phonon and electron transport is promising for 'phonon-glass, electron-crystal' for high performance of thermoelectric device.

5.2 Microscopic mechanism and dynamics of structural phase transition

The population of quasiparticles, as the source for external energy, drives phase transition. And at the same time, the band structure of two-dimensional material has been modified greatly [143,144], as well as the kinetic barriers [145]. As a competing process with structural modification, band renormalization is extremely important since it determines energy barrier for such transition. Thus, revealing such process is one direction we are exploring and extracting information from the intermixing of band renormalization and phase change. Meanwhile, the microscopic images of kinetic paths are missing. Since the sensitivity of band modification differs from band to band, we expect the kinetic path depends on the population of quasiparticles as well. And limited by the resolution of optical approaches, the formation and immigration of domains demand image tool with

high resolution, to confirm that the domain size is controllable under manipulating quasiparticles and the mechanism of well-alignments for distinct domains [146].

More practically, the time scale of structural phase transition from 2H to 1T', which determines the intrinsic frequency of devices, such as memories, is hindered by the slow movement of ionic liquid. This reveals the urgent need for dielectric gate, working for high frequency as well as high doping level. Even without such gating for now, we envision that two types of designs would be promising to obtain the intrinsic time scale. One way is to use ultrafast optical doping to get rid of ionic liquids [29]. And the alternative approach is releasing part of doping requirement to strain engineering [147] so that traditional solid gate should meet the requirement for doping, especially the ultrathin boron nitride. Meanwhile, the hybrid of strain and electrostatic doping system is more applicable to high-resolution imaging systems, eliminating the large scattering of ionic liquid for electron probes. With a better understanding of dynamics as well as mechanisms of domain growths, it would benefit the field of structural phase engineering under the new degree of freedom.

5.3 Quasiparticles in other low-dimensional orderings

Besides the insulator-to-metal and structural transitions in two-dimensional materials, other orderings attract great attention such as the formation of superconductivity, which originates from competition between electron-electron and electron-phonon interactions. Recent experiments on FeSe films grown on $SrTiO_3$ (STO) exhibits super high T_c, up to 100K, which is much higher than its bulk [148] [149]. And replica bands observed by Angle-resolved photoemission spectroscopy suggest the importance of the interaction between FeSe electrons and STO phonons [150]. And people already proved that electrostatic doping optimizes electron-phonon interaction in few layer MoS_2 [9], showing a complete superconducting dome. Similar to MoS_2, it is possible to further optimize the T_c and enrich understanding phonons' role in FeSe [149]. Meanwhile, two-dimensional material, with stable interface, works as a best platform to reveal ordering competitions.

On the other hand, intrinsic two-dimensional ferromagnetism was discovered recently, by overcoming thermal fluctuation with magnetic anisotropy [152,153]. Quasiparticles as an effective tool for engineering anisotropy energy and proves to stabilize T_c of ferromagnetism to room temperature [154]. Interface engineering is an alternative approach to manipulate quasiparticles and increase T_c, without external voltage or sacrificing functionalities in previous work. More importantly, combining these two types of layered materials, it generates a hybridized superconducting-ferromagnetic systems and in which topological effect are expected while quasiparticle is the main tool to activate different orbitals, which is determinative for such hybrid system and waiting for exploration [155].

-

Bibliography

[1] S. Francoeur, M.-J. Seong, A. Mascarenhas, S. Tixier, M. Adamcyk, and T. Tiedje, Appl. Phys. Lett. **82**, 3874 (2003).

[2] H. Li, X. Duan, X. Wu, X. Zhuang, H. Zhou, Q. Zhang, X. Zhu, W. Hu, P. Ren, P. Guo, L. Ma, X. Fan, X. Wang, J. Xu, A. Pan, and X. Duan, J. Am. Chem. Soc. **136**, 3756 (2014).

[3] K. Oe, Japanese J. Appl. Physics, Part 1 Regul. Pap. Short Notes Rev. Pap. **41**, 2801 (2002).

[4] P. Dawson, B. A. Wilson, C. W. Tu, and R. C. Miller, Appl. Phys. Lett. **48**, 541 (1986).

[5] A. Baldereschi, K. Maschke, E. Hess, H. Neumann, K. R. Schulze, and K. Unger, J. Phys. C Solid State Phys. **10**, 4709 (1977).

[6] S. J. Kimber, A. Kreyssig, Y.-Z. Zhang, H. O. Jeschke, R. Valentí, F. Yokaichiya, E. Colombier, J. Yan, T. C. Hansen, T. Chatterji, R. J. McQueeney, P. C. Canfield, A. I. Goldman, and D. N. Argyriou, Nat. Mater. **8**, 471 (2009).

[7] J. W. & Sons, *MOSFET Device Physics and Operation* (2003).

[8] L. J. Li, E. C. T. O'Farrell, K. P. Loh, G. Eda, B. Özyilmaz, and A. H. Castro Neto, Nature **529**, 185 (2015).

[9] J. T. Ye, Y. J. Zhang, R. Akashi, M. S. Bahramy, R. Arita, and Y. Iwasa, Science (80-.). **338**, 1193 (2012).

[10] J. S. Ross, S. Wu, H. Yu, N. J. Ghimire, A. M. Jones, G. Aivazian, J. Yan, D. G. Mandrus, D. Xiao, W. Yao, and X. Xu, Nat. Commun. **4**, 1474 (2013).

[11] E. Abrahams, S. V. Kravchenko, and M. P. Sarachik, Rev. Mod. Phys. **73**, 251 (2001).

[12] A. Ohtomo and H. Y. Hwang, Nature **427**, 423 (2004).

[13] P. Ajayan, P. Kim, and K. Banerjee, Phys. Today **69**, 38 (2016).

[14] B. Radisavljevic, a Radenovic, J. Brivio, V. Giacometti, and a Kis, Nat. Nanotechnol. **6**, 147 (2011).

[15] Z. Lin, A. McCreary, N. Briggs, S. Subramanian, K. Zhang, Y. Sun, X. Li, N. J. Borys, H. Yuan, S. K. Fullerton-Shirey, A. Chernikov, H. Zhao, S. McDonnell, A. M. Lindenberg, K. Xiao, B. J. Le Roy, M. Drndić, J. C. M. Hwang, J. Park, M. Chhowalla, R. E. Schaak, A. Javey, M. C. Hersam, J. Robinson, and M. Terrones, in *2D Mater.* (2016).

[16] RadisavljevicB, RadenovicA, BrivioJ, GiacomettiV, KisA, B. Radisavljevic, A. Radenovic, J. Brivio, V. Giacometti, and A. Kis, Nat Nano **6**, 147 (2011).

[17] K. S. Novoselov, A. Mishchenko, A. Carvalho, A. H. C. Neto, and O. Road,

Science (80-.). **353**, aac9439 (2016).

[18] M. S. Dresselhaus, G. Chen, M. Y. Tang, R. Yang, H. Lee, D. Wang, Z. Ren, J. P. Fleurial, and P. Gogna, Adv. Mater. **19**, 1043 (2007).

[19] Z. Ye, T. Cao, K. O'Brien, H. Zhu, X. Yin, Y. Wang, S. G. Louie, and X. Zhang, Nature **513**, 214 (2014).

[20] B. Zhu, X. Chen, and X. Cui, Sci. Rep. **5**, 9218 (2015).

[21] M. M. Ugeda, A. J. Bradley, S. F. Shi, F. H. Da Jornada, Y. Zhang, D. Y. Qiu, W. Ruan, S. K. Mo, Z. Hussain, Z. X. Shen, F. Wang, S. G. Louie, and M. F. Crommie, Nat. Mater. **13**, 1091 (2014).

[22] K. F. Young and H. P. R. Frederikse, J. Phys. Chem. Ref. Data **2**, 313 (1973).

[23] K. Reimann, M. Steube, D. Fröhlich, and S. . Clarke, J. Cryst. Growth **189–190**, 652 (1998).

[24] A. Chernikov, T. C. Berkelbach, H. M. Hill, A. Rigosi, Y. Li, O. B. Aslan, D. R. Reichman, M. S. Hybertsen, and T. F. Heinz, Phys. Rev. Lett. **113**, 076802 (2014).

[25] G. Zhang, A. Chaves, S. Huang, F. Wang, Q. Xing, T. Low, and H. Yan, Sci. Adv. **4**, (2018).

[26] S. Dufferwiel, S. Schwarz, F. Withers, A. A. P. Trichet, F. Li, M. Sich, O. Del Pozo-Zamudio, C. Clark, A. Nalitov, D. D. Solnyshkov, G. Malpuech, K. S. Novoselov, J. M. Smith, M. S. Skolnick, D. N. Krizhanovskii, and A. I. Tartakovskii, Nat. Commun. **6**, (2015).

[27] L. V. Butov, Superlattices Microstruct. **108**, 2 (2017).

[28] G. Grosso, J. Graves, A. T. Hammack, A. A. High, L. V. Butov, M. Hanson, and A. C. Gossard, Nat. Photonics **3**, 577 (2009).

[29] A. Chernikov, C. Ruppert, H. M. Hill, A. F. Rigosi, and T. F. Heinz, Nat. Photonics **9**, 466 (2015).

[30] K. Yao, A. Yan, S. Kahn, A. Suslu, Y. Liang, E. S. Barnard, S. Tongay, A. Zettl, N. J. Borys, and P. J. Schuck, Phys. Rev. Lett. **119**, (2017).

[31] A. Chernikov, T. C. Berkelbach, H. M. Hill, A. Rigosi, Y. Li, O. B. Aslan, D. R. Reichman, M. S. Hybertsen, and T. F. Heinz, Phys. Rev. Lett. **113**, (2014).

[32] A. K. Geim and I. V Grigorieva, Nature **499**, 419 (2013).

[33] Y. Liu, N. O. Weiss, X. Duan, H.-C. Cheng, Y. Huang, and D. Xiangfeng, Nat. Rev. Mater. **490**, 16042 (2016).

[34] D. Jariwala, T. J. Marks, and M. C. Hersam, Nat. Mater. **advance on**, (2016).

[35] F. Withers, O. Del Pozo-Zamudio, A. Mishchenko, A. P. Rooney, A. Gholinia, K. Watanabe, T. Taniguchi, S. J. Haigh, A. K. Geim, A. I. Tartakovskii, and K. S. Novoselov, Nat Mater **14**, 301 (2015).

[36] T. Roy, M. Tosun, J. S. Kang, A. B. Sachid, S. B. Desai, M. Hettick, C. C. Hu, and A. Javey, ACS Nano **8**, 6259 (2014).

[37] J. Jung, A. DaSilva, A. H. MacDonald, and S. Adam, Nat. Commun. **6**, 6308 (2014).

[38] A. H. MacDonald and R. Bistritzer, Nature **474**, 453 (2011).

[39] Y. Cao, V. Fatemi, S. Fang, K. Watanabe, T. Taniguchi, E. Kaxiras, and P. Jarillo-Herrero, Nature (2018).

[40] K. Hippalgaonkar, Y. Wang, Y. Ye, D. Y. Qiu, H. Zhu, Y. Wang, J. Moore, S. G. Louie, and X. Zhang, Phys. Rev. B **95**, 115407 (2017).

[41] Y. Wang, J. Xiao, H. Zhu, Y. Li, Y. Alsaid, K. Y. Fong, Y. Zhou, S. Wang, W. Shi, Y. Wang, A. Zettl, E. J. Reed, and X. Zhang, Nature **550**, 487 (2017).

[42] S. B. Riffat and X. Ma, Appl. Therm. Eng. **23**, 913 (2003).

[43] Y. Heichal, S. Chandra, and E. Bordatchev, Exp. Therm. Fluid Sci. **30**, 153 (2005).

[44] F. J. DiSalvo, Science **285**, 703 (1999).

[45] H. S. Kim, W. Liu, G. Chen, C.-W. Chu, and Z. Ren, PNAS **112**, 8205 (2015).

[46] Chemical Engineering Science Group, Renew. Energy Devices **31**, 2006 (2008).

[47] L.-D. Zhao, S.-H. Lo, Y. Zhang, H. Sun, G. Tan, C. Uher, C. Wolverton, V. P. Dravid, and M. G. Kanatzidis, Nature **508**, 373 (2014).

[48] A. I. Hochbaum, R. Chen, R. D. Delgado, W. Liang, E. C. Garnett, M. Najarian, A. Majumdar, and P. Yang, Nature **451**, 163 (2008).

[49] J. P. Heremans, V. Jovovic, E. S. Toberer, A. Saramat, K. Kurosaki, A. Charoenphakdee, S. Yamanaka, and G. J. Snyder, Science (80-.). **321**, 554 (2008).

[50] L. D. Zhao, G. Tan, S. Hao, J. He, Y. Pei, H. Chi, H. Wang, S. Gong, H. Xu, V. P. Dravid, C. Uher, G. J. Snyder, C. Wolverton, and M. G. Kanatzidis, Science (80-.). **351**, 141 (2016).

[51] D. Vashaee and A. Shakouri, Phys. Rev. Lett. **92**, (2004).

[52] K. F. Mak, C. Lee, J. Hone, J. Shan, and T. F. Heinz, Phys. Rev. Lett. **105**, (2010).

[53] S. Bhattacharyya and A. K. Singh, Phys. Rev. B - Condens. Matter Mater. Phys. **86**, (2012).

[54] C. Chiritescu, D. G. Cahill, N. Nguyen, D. Johnson, A. Bodapati, P. Keblinski, and P. Zschack, Science (80-.). **315**, 351 (2007).

[55] W. Huang, X. Luo, C. K. Gan, S. Y. Quek, and G. Liang, Phys. Chem. Chem. Phys. **16**, 10866 (2014).

[56] Z. H. Dughaish, Phys. B Condens. Matter **322**, 205 (2002).

[57] B. Baugher, H. O. H. Churchill, Y. Yang, and P. Jarillo-herrero, Nano Lett. **13**, 4212 (2013).

[58] C. Lee, H. Yan, L. E. Brus, T. F. Heinz, J. Hone, and S. Ryu, ACS Nano **4**, 2695 (2010).

[59] S. Najmaei, Z. Liu, P. M. Ajayan, and J. Lou, Appl. Phys. Lett. **100**, 013106 (2012).

[60] A. Splendiani, L. Sun, Y. Zhang, T. Li, J. Kim, C. Y. Chim, G. Galli, and F. Wang, Nano Lett. **10**, 1271 (2010).

[61] P. Nemes-Incze, Z. Osváth, K. Kamarás, and L. P. Biró, Carbon N. Y. **46**, 1435 (2008).

[62] B. Radisavljevic and A. Kis, Nat. Mater. **12**, 815 (2013).

[63] X. Cui, G.-H. Lee, Y. D. Kim, G. Arefe, P. Y. Huang, C.-H. Lee, D. a. Chenet, X. Zhang, L. Wang, F. Ye, F. Pizzocchero, B. S. Jessen, K. Watanabe, T. Taniguchi, D. a. Muller, T. Low, P. Kim, and J. Hone, Nat. Nanotechnol. **10**, 534 (2015).

[64] D. M. Rowe, *Thermoelectrics Handbook: Macro to Nano* (Taylor & Francis, 2005).

[65] B. Bhushan, *Springer Handbook of Nanotechnology* (Springer, 2007).

[66] D. M. Rowe and G. Min, J. Mater. Sci. Lett. **14**, 617 (1995).

[67] H. Babaei, J. M. Khodadadi, and S. Sinha, Appl. Phys. Lett. **105**, (2014).

[68] H.-P. Komsa and A. V. Krasheninnikov, Phys. Rev. B **86**, 241201 (2012).

[69] A. Molina-Sánchez, D. Sangalli, K. Hummer, A. Marini, and L. Wirtz, Phys. Rev. B - Condens. Matter Mater. Phys. **88**, (2013).

[70] J. M. Ziman, Endeavour **20**, 555 (1960).

[71] N. Mohankumar and A. Natarajan, Phys. Status Solidi **188**, 635 (1995).

[72] X. Li, J. T. Mullen, Z. Jin, K. M. Borysenko, M. Buongiorno Nardelli, and K. W. Kim, Phys. Rev. B - Condens. Matter Mater. Phys. **87**, (2013).

[73] G. J. Snyder and E. S. Toberer, Nat. Mater. **7**, 105 (2008).

[74] K. Kaasbjerg, K. S. Thygesen, and K. W. Jacobsen, Phys. Rev. B - Condens. Matter Mater. Phys. **85**, (2012).

[75] A. H. . Castro Neto, N. M. R. . Peres, K. S. . Novoselov, A. K. . Geim, and F. Guinea, Rev. Mod. Phys. **81**, 109 (2009).

[76] C. C. Chen, W. Bao, J. Theiss, C. Dames, C. N. Lau, and S. B. Cronin, Nano Lett. **9**, 4172 (2009).

[77] W. Bao, K. Myhro, Z. Zhao, Z. Chen, W. Jang, L. Jing, F. Miao, H. Zhang, C. Dames, and C. N. Lau, Nano Lett. **12**, 5470 (2012).

[78] J. Brivio, D. D. T. L. D. D. T. L. Alexander, and A. Kis, Nano Lett. **11**, 5148 (2011).

[79] S. Luo, G. Hao, Y. Fan, L. Kou, C. He, X. Qi, C. Tang, J. Li, K. Huang, and J. Zhong, Nanotechnology **26**, 105705 (2015).

[80] A. Castellanos-Gomez, R. Roldán, E. Cappelluti, M. Buscema, F. Guinea, H. S. J. Van Der Zant, and G. A. Steele, Nano Lett. **13**, 5361 (2013).

[81] B. Radisavljevic and A. Kis, Nat. Mater. **12**, 815 (2013).

[82] Z. Yu, Y. Pan, Y. Shen, Z. Wang, Z. Y. Ong, T. Xu, R. Xin, L. Pan, B. Wang, L. Sun, J. Wang, G. Zhang, Y. W. Zhang, Y. Shi, and X. Wang, Nat. Commun. **5**, (2014).

[83] W. Zhu, T. Low, Y. H. Lee, H. Wang, D. B. Farmer, J. Kong, F. Xia, and P. Avouris, Nat. Commun. **5**, (2014).

[84] S. Ghatak, A. N. Pal, and A. Ghosh, ACS Nano **5**, 7707 (2011).

[85] S.-T. Lo, O. Klochan, C.-H. Liu, W.-H. Wang, a R. Hamilton, and C.-T. Liang, Nanotechnology **25**, 375201 (2014).

[86] B. W. H. Baugher, H. O. H. Churchill, Y. Yang, and P. Jarillo-Herrero, Nano Lett. **13**, 4212 (2013).

[87] D. Yu, C. Wang, B. L. Wehrenberg, and P. Guyot-Sionnest, Phys. Rev. Lett. **92**, (2004).

[88] I. P. Zvyagin, Phys. Status Solidi **58**, 443 (1973).

[89] S. V. Demishev, M. V. Kondrin, a. a. Pronin, N. E. Sluchanko, N. a. Samarin, a. G. Lyapin, and G. Biscupski, J. Exp. Theor. Phys. Lett. **68**, 842 (1998).

[90] M. J. Burns and P. M. Chaikin, J. Phys. C Solid State Phys. **18**, L743 (1985).

[91] B. Jalan and S. Stemmer, Appl. Phys. Lett. **97**, (2010).

[92] K. P. Pernstich, B. Rössner, and B. Batlogg, Nat. Mater. **7**, 321 (2008).

[93] D. Ovchinnikov, A. Allain, Y. S. Huang, D. Dumcenco, and A. Kis, ACS Nano **8**, 8174 (2014).

[94] G. Eda, C. Mattevi, H. Yamaguchi, H. Kim, and M. Chhowalla, J. Phys. Chem. C **113**, 15768 (2009).

[95] H. Qiu, T. Xu, Z. Wang, W. Ren, H. Nan, Z. Ni, Q. Chen, S. Yuan, F. Miao, F. Song, G. Long, Y. Shi, L. Sun, J. Wang, and X. Wang, Nat. Commun. **4**, (2013).

[96] K. L. Grosse, M. H. Bae, F. Lian, E. Pop, and W. P. King, Nat. Nanotechnol. **6**, 287 (2011).

[97] M.-H. Bae, Z.-Y. Ong, D. Estrada, and E. Pop, Nano Lett. **10**, 4787 (2010).

[98] S. Sahoo, A. P. S. Gaur, M. Ahmadi, M. J. F. Guinel, and R. S. Katiyar, J. Phys.

Chem. C **117**, 9042 (2013).

[99] R. Yan, J. R. Simpson, S. Bertolazzi, J. Brivio, M. Watson, X. Wu, A. Kis, T. Luo, A. R. Hight Walker, and H. G. Xing, ACS Nano **8**, 986 (2014).

[100] Q. H. Wang, K. Kalantar-Zadeh, A. Kis, J. N. Coleman, and M. S. Strano, Nat. Nanotechnol. **7**, 699 (2012).

[101] D. Xiao, G. Bin Liu, W. Feng, X. Xu, and W. Yao, Phys. Rev. Lett. **108**, 196802 (2012).

[102] T. Cao, J. Feng, J. Shi, Q. Niu, and E. Wang, Nat. Commun. **3**, 885 (2011).

[103] K. F. Mak, K. L. McGill, J. Park, and P. L. McEuen, Science (80-.). **344**, 1489 (2014).

[104] Z. Ye, T. Cao, K. O'Brien, H. Zhu, X. Yin, Y. Wang, S. G. Louie, and X. Zhang, Nature **513**, 214 (2014).

[105] J. A. Wilson and A. D. Yoffe, Adv. Phys. **18**, 193 (1969).

[106] X. Qian, J. Liu, L. Fu, and J. Li, Science (80-.). **346**, 1344 (2014).

[107] Y. Ma, L. Kou, X. Li, Y. Dai, S. C. Smith, and T. Heine, Phys. Rev. B **92**, 085427 (2015).

[108] M. Imada, A. Fujimori, and Y. Tokura, Rev. Mod. Phys. **70**, 1039 (1998).

[109] Q. Wang, E. T. F. Rogers, B. Gholipour, C.-M. Wang, G. Yuan, J. Teng, and N. I. Zheludev, Nat. Photonics **10**, 60 (2015).

[110] M. Wuttig and N. Yamada, Nat. Mater. **6**, 824 (2007).

[111] D. H. Keum, S. Cho, J. H. Kim, D.-H. Choe, H.-J. Sung, M. Kan, H. Kang, J.-Y. Hwang, S. W. Kim, H. Yang, K. J. Chang, and Y. H. Lee, Nat. Phys. **11**, 482 (2015).

[112] D. Rhodes, D. A. Chenet, B. E. Janicek, C. Nyby, Y. Lin, W. Jin, D. Edelberg, E. Mannebach, N. Finney, A. Antony, T. Schiros, T. Klarr, A. Mazzoni, M. Chin, Y. –. Chiu, W. Zheng, Q. R. Zhang, F. Ernst, J. I. Dadap, X. Tong, J. Ma, R. Lou, S. Wang, T. Qian, H. Ding, R. M. Osgood, D. W. Paley, A. M. Lindenberg, P. Y. Huang, A. N. Pasupathy, M. Dubey, J. Hone, and L. Balicas, ArXiv: 1610.02480 (2016).

[113] S. Cho, S. Kim, J. H. Kim, J. Zhao, J. Seok, D. H. Keum, J. Baik, D.-H. Choe, K. J. Chang, K. Suenaga, S. W. Kim, Y. H. Lee, and H. Yang, Science (80-.). **349**, 625 (2015).

[114] J.-F. Ge, Z.-L. Liu, C. Liu, C.-L. Gao, D. Qian, Q.-K. Xue, Y. Liu, and J.-F. Jia, Nat. Mater. **14**, 285 (2014).

[115] X. Xi, Z. Wang, W. Zhao, J.-H. Park, K. T. Law, H. Berger, L. Forró, J. Shan, and K. F. Mak, Nat. Phys. **12**, 139 (2015).

[116] Y. Li, K.-A. N. Duerloo, K. Wauson, and E. J. Reed, Nat. Commun. 1 (2016).

[117] M. Armand, F. Endres, D. R. MacFarlane, H. Ohno, and B. Scrosati, Nat. Mater. **8**, 621 (2009).

[118] S. Zhang, J. Sun, X. Zhang, J. Xin, Q. Miao, and J. Wang, Chem. Soc. Rev. **43**, 7838 (2014).

[119] A. Lewandowski and A. Świderska-Mocek, J. Power Sources **194**, 601 (2009).

[120] N. V. Chandra Shekar and K. G. Rajan, Bull. Mater. Sci. **24**, 1 (2001).

[121] Y.-C. Lin, D. O. Dumcenco, Y.-S. Huang, and K. Suenaga, Nat. Nanotechnol. **9**, 391 (2014).

[122] J. G. Ramírez, A. Sharoni, Y. Dubi, M. E. Gómez, and I. K. Schuller, Phys. Rev. B **79**, 235110 (2009).

[123] G. C. Hadjipanayis, editor , *Magnetic Hysteresis in Novel Magnetic Materials* (Springer Netherlands, Dordrecht, 1997).

[124] R. Yan, S. Bertolazzi, J. Brivio, T. Fang, A. Konar, a. G. Birdwell, N. V. Nguyen, A. Kis, D. Jena, and H. G. Xing, ArXiv Prepr. ArXiv … 17 (2012).

[125] C. Ruppert, O. B. Aslan, and T. F. Heinz, Nano Lett. **14**, 6231 (2014).

[126] K. F. Mak, M. Y. Sfeir, Y. Wu, C. H. Lui, J. A. Misewich, and T. F. Heinz, Phys. Rev. Lett. **101**, 196405 (2008).

[127] C. Ruppert, O. B. Aslan, and T. F. Heinz, Nano Lett. **14**, 6231 (2014).

[128] K. L. Seyler, J. R. Schaibley, P. Gong, P. Rivera, A. M. Jones, S. Wu, J. Yan, D. G. Mandrus, W. Yao, and X. Xu, Nat. Nanotechnol. **10**, 407 (2015).

[129] A. C. Ferrari, F. Bonaccorso, V. Fal'ko, K. S. Novoselov, S. Roche, P. Bøggild, S. Borini, F. H. L. Koppens, V. Palermo, N. Pugno, J. A. Garrido, R. Sordan, A. Bianco, L. Ballerini, M. Prato, E. Lidorikis, J. Kivioja, C. Marinelli, T. Ryhänen, A. Morpurgo, J. N. Coleman, V. Nicolosi, L. Colombo, A. Fert, M. Garcia-Hernandez, A. Bachtold, G. F. Schneider, F. Guinea, C. Dekker, M. Barbone, Z. Sun, C. Galiotis, A. N. Grigorenko, G. Konstantatos, A. Kis, M. Katsnelson, L. Vandersypen, A. Loiseau, V. Morandi, D. Neumaier, E. Treossi, V. Pellegrini, M. Polini, A. Tredicucci, G. M. Williams, B. Hee Hong, J.-H. Ahn, J. Min Kim, H. Zirath, B. J. van Wees, H. van der Zant, L. Occhipinti, A. Di Matteo, I. A. Kinloch, T. Seyller, E. Quesnel, X. Feng, K. Teo, N. Rupesinghe, P. Hakonen, S. R. T. Neil, Q. Tannock, T. Löfwander, and J. Kinaret, Nanoscale **7**, 4598 (2015).

[130] F. Xia, H. Wang, D. Xiao, M. Dubey, and A. Ramasubramaniam, Nat. Photonics **8**, 899 (2014).

[131] L. Yuan and L. Huang, Nanoscale (2015).

[132] H. Wang, C. Zhang, and F. Rana, Nano Lett. **15**, 339 (2015).

[133] R. S. Sundaram, M. Engel, A. Lombardo, R. Krupke, A. C. Ferrari, P. Avouris,

and M. Steiner, Nano Lett. **13**, 1416 (2013).

[134] H. Nan, Z. Wang, W. Wang, Z. Liang, Y. Lu, Q. Chen, D. He, P. Tan, F. Miao, X. Wang, J. Wang, and Z. Ni, ACS Nano **8**, 5738 (2014).

[135] M. Amani, D. H. Lien, D. Kiriya, J. Xiao, A. Azcatl, J. Noh, S. R. Madhvapathy, R. Addou, K. C. Santosh, M. Dubey, K. Cho, R. M. Wallace, S. C. Lee, J. H. He, J. W. Ager, X. Zhang, E. Yablonovitch, and A. Javey, Science (80-.). **350**, 1065 (2015).

[136] A. M. Goldman, Annu. Rev. Mater. Res. **44**, 45 (2014).

[137] T. Sato, G. Masuda, and K. Takagi, Electrochim. Acta **49**, 3603 (2004).

[138] Y. Yoshimura, T. Takekiyo, Y. Imai, and H. Abe, J. Phys. Chem. C **116**, 2097 (2012).

[139] N. Kumar, Q. Cui, F. Ceballos, D. He, Y. Wang, and H. Zhao, Phys. Rev. B - Condens. Matter Mater. Phys. **89**, (2014).

[140] A. A. Balandin, J. Nanosci. Nanotechnol. **5**, 1015 (2005).

[141] S. Wu, V. Fatemi, Q. D. Gibson, K. Watanabe, T. Taniguchi, R. J. Cava, and P. Jarillo-Herrero, Science (80-.). **359**, 76 (2018).

[142] N. Xu, Y. Xu, and J. Zhu, Npj Quantum Mater. **2**, 51 (2017).

[143] A. Walsh, J. L. F. Da Silva, and S. H. Wei, Phys. Rev. B - Condens. Matter Mater. Phys. **78**, (2008).

[144] J. Katoch, S. Ulstrup, R. J. Koch, S. Moser, K. M. McCreary, S. Singh, J. Xu, B. T. Jonker, R. K. Kawakami, A. Bostwick, E. Rotenberg, and C. Jozwiak, Nat. Phys. 1 (2018).

[145] O. Rubel, ArXiv: **1711**, 11147 (2017).

[146] Y.-C. Lin, D. O. Dumcenco, Y.-S. Huang, and K. Suenaga, Nat. Nanotechnol. **9**, 391 (2014).

[147] K.-A. N. Duerloo, Y. Li, and E. J. Reed, Nat. Commun. **5**, (2014).

[148] G. Zhou, D. Zhang, C. Liu, C. Tang, X. Wang, Z. Li, C. Song, S. Ji, K. He, L. Wang, X. Ma, and Q. K. Xue, Appl. Phys. Lett. **108**, (2016).

[149] J. F. Ge, Z. L. Liu, C. Liu, C. L. Gao, D. Qian, Q. K. Xue, Y. Liu, and J. F. Jia, Nat. Mater. **14**, 285 (2015).

[150] J. J. Lee, F. T. Schmitt, R. G. Moore, S. Johnston, Y. T. Cui, W. Li, M. Yi, Z. K. Liu, M. Hashimoto, Y. Zhang, D. H. Lu, T. P. Devereaux, D. H. Lee, and Z. X. Shen, Nature **515**, 245 (2014).

[151] R. Peng, H. C. Xu, S. Y. Tan, H. Y. Cao, M. Xia, X. P. Shen, Z. C. Huang, C. H. P. Wen, Q. Song, T. Zhang, B. P. Xie, X. G. Gong, and D. L. Feng, Nat. Commun. **5**, (2014).

[152] C. Gong, L. Li, Z. Li, H. Ji, A. Stern, Y. Xia, T. Cao, W. Bao, C. Wang, Y. Wang, Z. Q. Qiu, R. J. Cava, S. G. Louie, J. Xia, and X. Zhang, Nature **546**, 265 (2017).

[153] B. Huang, G. Clark, E. Navarro-Moratalla, D. R. Klein, R. Cheng, K. L. Seyler, D. Zhong, E. Schmidgall, M. A. McGuire, D. H. Cobden, W. Yao, D. Xiao, P. Jarillo-Herrero, and X. Xu, Nature **546**, 270 (2017).

[154] ArXiv:1803.02038 (2018).

[155] S. Nadj-Perge, I. K. Drozdov, J. Li, H. Chen, S. Jeon, J. Seo, A. H. MacDonald, B. A. Bernevig, and A. Yazdani, Science (80-.). **346**, 602 (2014).